

MINCE III. Detailed chemical analysis of the UVES sample[★]

F. Lucertini¹, L. Sbordone¹, E. Caffau^{2,3}, P. Bonifacio^{2,3}, L. Monaco^{4,3}, G. Cescutti^{5,3,6}, R. Lallement², P. François^{2,8},
E. Spitoni³, C. J. Hansen⁷, A. J. Korn⁹, A. Kučinskas¹⁰, A. Mucciarelli^{11,12}, L. Magrini¹³, L. Lombardo⁷,
M. Franchini³, and R. F. de Melo¹⁴

¹ ESO - European Southern Observatory, Alonso de Cordova 3107, Vitacura, Santiago, Chile

² GEPI, Observatoire de Paris, Université PSL, CNRS, 5 Place Jules Janssen, 92190 Meudon, France

³ INAF-Osservatorio Astronomico di Trieste, Via G.B. Tiepolo 11, 34143 Trieste, Italy

⁴ Universidad Andres Bello, Facultad de Ciencias Exactas, Departamento de Físicas y Astronomía - Instituto de Astrofísica, Autopista Concepción-Talcahuano, 7100, Talcahuano, Chile

⁵ Dipartimento di Fisica, Sezione di Astronomia, Università di Trieste, Via G. B. Tiepolo 11, 34143 Trieste, Italy

⁶ INFN, Sezione di Trieste, Via A. Valerio 2, 34127 Trieste, Italy

⁷ Institute for Applied Physics, Goethe University Frankfurt, Max-von-Laue-Strasse 1, 60438 Frankfurt am Main, Germany.

⁸ UPJV, Université de Picardie Jules Verne, Pôle Scientifique, 33 rue St Leu, 80039, Amiens, France

⁹ Division of Astronomy and Space Physics, Department of Physics and Astronomy, Uppsala University, Box 516, 75120 Uppsala, Sweden

¹⁰ Institute of Theoretical Physics and Astronomy, Vilnius University, Saulėtekio al. 3, 10257 Vilnius, Lithuania

¹¹ Dipartimento di Fisica e Astronomia “Augusto Righi”, Alma Mater Studiorum, Università di Bologna, Via Gobetti 93/2, 40129 Bologna, Italy

¹² INAF – Osservatorio di Astrofisica e Scienza dello Spazio di Bologna, Via Gobetti 93/3, 40129 Bologna, Italy

¹³ INAF – Osservatorio Astrofisico di Arcetri, Largo E. Fermi, 5, 50125, Firenze, Italy

¹⁴ Goethe University Frankfurt, Institute for Applied Physics, Max-von-Laue-Str. 12, 60438 Frankfurt am Main, Germany

Received November 11, 2024; accepted January 17, 2025

ABSTRACT

Context. The MINCE (Measuring at Intermediate Metallicity Neutron-Capture Elements) project aims to provide high quality neutron-capture abundances measurements in several hundred stars at intermediate metallicity, $-2.5 < [\text{Fe}/\text{H}] < -1.5$. This project will shed light on the origin of the neutron-capture elements and the chemical enrichment of the Milky Way.

Aims. The goal of this work is to chemically characterize the second sample of the MINCE project and compare the abundances with the galactic chemical evolution model at our disposal.

Methods. We performed a standard abundance analysis based on 1D LTE model atmospheres on high-resolution and high-signal-to-noise-ratio UVES spectra.

Results. We provide the kinematic classification (i.e., thin disk, thick disk, thin-to-thick disk, halo, Gaia Sausage Enceladus, Sequoia) of 99 stars and the atmospheric parameters for almost all stars. We derive the abundances for light elements (from Na to Zn) and neutron-capture elements (Rb, Sr, Y, Zr, Ba, La, Ce, Pr, Nd, Sm, Eu) in a subsample of 32 stars in the metallicity range $-2.5 < [\text{Fe}/\text{H}] < -1.00$. In the subsample of 32 stars, we identify 8 active stars exhibiting (inverse) P-Cygni profile and one Li-rich star, CD 28-11039. We find a general agreement between the chemical abundances and the stochastic model computed for the chemical evolution of the Milky Way halo for the elements Mg, Ca, Si, Ti, Sc, Mn, Co, Ni, Zn, Rb, Sr, Y, Zr, Ba, La, and Eu .

Conclusions. The MINCE project has already significantly increased the number of neutron-capture elements measurements in the intermediate metallicity range. The results from this sample are in perfect agreement with the previous MINCE sample. The good agreement between the chemical abundances and the chemical evolution model of the Galaxy supports the nucleosynthetic processes adopted to describe the origin of the n-capture elements.

Key words. Galaxy: evolution - Galaxy: formation - Galaxy: halo – stars: abundances - stars: atmospheres - nuclear reactions, nucleosynthesis, abundances

1. Introduction

One of the astronomical ways to constrain the Galaxy’s formation and evolution is a detailed chemical analysis of its stellar populations. The main ingredients for this purpose are a complete census of the stellar populations hosted by the Galaxy, and a deep investigation of the different nucleosynthesis processes. The goal of the MINCE project (Measuring at Interme-

diate Metallicity Neutron-Capture Elements, see [Cescutti et al. 2022](#)) is to fill in with chemical abundances of mildly metal-poor stars ($-2.5 < [\text{Fe}/\text{H}] < -1.5$).

The understanding of early Galactic neutrosynthesis processes and chemical evolution led to hunt the ever more metal-poor stars. This effort increased with the discovery of Carbon Enhanced Metal-Poor (CEMP) stars ([Sneden et al. 1994](#); [Barbuy et al. 1997](#); [Norris et al. 1997](#); [Bonifacio et al. 1998](#); [Hill et al. 2000](#)) characterized by different neutron-capture (n-capture) elements content ([Cohen et al. 2003](#); [Beers & Christlieb 2005](#); [Hansen et al. 2012](#); [Roederer et al. 2014](#); [Yong et al. 2014](#)). At

* This paper is based on data collected with the Very Large Telescope (VLT) at the European Southern Observatory (ESO) on Paranal, Chile (ESO Program ID: 105.20ML.001, 106.21PG.001)

the same time, the n-capture elements abundances in halo stars have been analyzed in several Galactic archaeology studies (see e.g. François et al. 2003, 2007, and references therein). As a result, the old giant stars with intermediate metallicity have been less examined by the scientific community.

The bulk of elements heavier than iron are produced through slow (s), rapid (r) or intermediate (i) neutron capture processes. The difference among these processes lie in the neutron density, which determines the probability of capturing a neutron before the radioactive beta decay (Burbidge et al. 1957). The s-process occurs in the inter-shell region of asymptotic giant branch (AGB) stars with low- and intermediate-mass (Gallino et al. 1998; Busso et al. 1999; Karakas & Lattanzio 2014). Both Supernovae and neutron star mergers have been proposed as sites hosting the r-process (Argast et al. 2004; Côté et al. 2018; Watson et al. 2019; Cavallo et al. 2021; Cowan et al. 2021). Despite several suggested sites, the site of the i-process remains an open question (Hampel et al. 2016, 2019; Denissenkov et al. 2017). For a recent review on the origin of the elements, see Arcones & Thielemann (2023).

Another puzzle concerning n-capture elements abundances is their large star-to-star scatter at low metallicities. Indeed, it has been shown that the dispersion in [n-capture/Fe] increases as metallicity decreases. This finding provides critical insights into the origin of n-capture elements (Hansen et al. 2014) and the processes of formation of the MW.

In summary, the measurement of n-capture elements in intermediate metallicity stars will allow us to increase our knowledge on the contribution from the different n-capture processes. Consequently, this will provide new insights into the origin of the heavy elements and their progenitor stars may be achieved. This will also shed light on the early interstellar medium (ISM) pollution process and its timescales (Côté et al. 2019), which are fundamental details to improve the Galactic chemical evolution models.

In this work we present the chemical abundances of the second MINCE sample (hereafter referred to as MINCE III), thus the results obtained for light elements (from Na to Zn) and n-capture elements (Rb, Sr, Y, Zr, Ba, La, Ce, Pr, Nd, Sm, Eu), and their comparison with the chemical evolution model of the Galaxy.

2. Observations and data reduction

The MINCE project exploits several facilities around the world to collect high-quality data, and provide precise atmospheric parameters and chemical abundances of stars at intermediate metallicity.

In this paper, we present a sample of 99 stars observed with UVES@ESO-VLT/UT2 (Dekker et al. 2000), Paranal Observatory (Chile). The data were collected between September 2020 and August 2021. The instrument was set with two configurations: Dichroic#1, blue and red arms centered at 346 nm and 580 nm, respectively, and Dichroic#2, blue and red arms centered at 437 nm and 760 nm, respectively. The final dataset for each star covers the spectral range 304–945 nm. A slit width of 0.5 arcsec was used, providing a high resolving power of R~65000 and R~75000 in blue and red spectra, respectively. The data were reduced using the UVES pipeline (version 5.10.13¹). The final spectra are characterized by high signal-to-noise ratio (SNR), with mean values of 148 at 580 nm and 105 at 760 nm.

¹ <https://www.eso.org/sci/software/pipelines/>

Table B.1 lists the coordinates and the *Gaia* eDR3 (Gaia Collaboration et al. 2021) magnitudes of the sample.

2.1. Radial velocities

The *Gaia* DR3 (Gaia Collaboration et al. 2022) radial velocities (RV) of the targets used in this work are listed in Table B.1, when available. When the radial velocity was not available from *Gaia* DR3 it was estimated directly from our UVES spectrum.

These values were used to shift the observed spectra to the rest frame. However, in the case of six stars we did not find a good match between the synthetic and the observational spectra. For CD-28 10387, we found an RV difference of 7.49 kms⁻¹. For this star, *Gaia* DR3 provides a ruwe value of 3.63, suggesting a possible binary nature. In the case of CD-29 15930 and CD-31 16658, we applied an additional shift of -4.99 kms⁻¹ and -7.49 kms⁻¹, respectively. The final RV of CD-31 16922 differs from the *Gaia* one by 17.47 kms⁻¹. It is interesting to note that *Gaia* estimates an error on the RV of about 9.08 kms⁻¹ for this star. The largest shift corrections found are those corresponding to CD-44 12644 (-29.95 kms⁻¹) and TYC 5422-1192-1 (19.97 kms⁻¹).

Except for TYC 5422-1192-1, we do not detect the contribution of a companion in the spectra of the above mentioned stars. Thus, we can reasonably exclude that these stars are double-lined spectroscopic binary (SB2), and that the companion contributes to the spectrum to explain the disagreements with *Gaia* RV. It is however quite likely that these five stars are single lined spectroscopic binaries; the future release of *Gaia* epoch radial velocities will help to elucidate this issue.

Taking into account the shift estimated, we corrected the *Gaia* RV and reported the final results in Table B.1, where the results for these stars are highlighted with the superscript (a).

3. Analysis

3.1. Stellar parameters

Each stellar parameters derivation method leads to systematic errors in the estimation of chemical abundances. Since the MINCE project has at its disposal several spectra, a homogeneous way to derive the stellar parameters is required to present consistent analysis. For this reason, we obtained the atmospheric parameters as described in Cescutti et al. (2022).

Starting from the *Gaia* eDR3 (Gaia Collaboration et al. 2021) photometry, we first obtained the dereddened *G* magnitude and $G_{BP} - G_{RP}$ color of the targets. Extinction estimates were made for each target star according to the following scheme. The first step uses the extinction density maps presented by Vergely et al. (2022). For each star the extinction density (in mag per pc) is integrated along the paths between the Sun and the star to provide the total extinction. Details about the maps can be found in Vergely et al. (2022). In brief, they were computed by inversion of about 40 million individual extinction measurements for stars with precise distances, mainly *Gaia* parallaxes. The inversion is regularised on the basis of a covariance kernel (or minimum cloud size) adapted to the volume density of the targets through a hierarchical scheme. In addition to the three maps presented in that work, for close targets we also used an additional unpublished map with a minimum kernel size of 5 pc (courtesy J.L. Vergely). The largest map has a volume of 10 kpc x 10 kpc x 800 pc centred on the Sun (largest dimensions along the Plane, 400 pc maximum distance from the Plane). Given the limits of the volumes covered by the mapping, distant stars and halo

stars may be located outside the computational volume. In this case, we also searched for the extinction estimate from [Green et al. \(2019\)](#), if available. For all targets, we also computed an estimate of the total extinction up to large distance outside the dust disk by using Planck dust emission measurements ([Planck Collaboration et al. 2016](#)). Specifically, we converted the optical thickness at 353 GHz into an extinction in the visible using $A_V = 3.1 * 1.510^4 \tau$ (353). We slightly refined this estimate, when possible, based on Figure 11 of [Remy et al. \(2018\)](#), using in addition the Planck temperature and the β coefficient. For most of the targets located outside the maps, the Planck-based value and the extinction reached at the boundary of the map (or for a few cases the [Green et al. 2019](#) value) are very close to each other (average difference of 0.05 mag, maximum difference of 0.2 mag), meaning that the target is located beyond the majority of the dust. In this case we preferred the maximal value, given the large distance of the targets. The extinction values adopted in this work are reported in Table B.2.

The first guess stellar parameters were obtained comparing synthetic colors with the dereddened $G_{BP} - G_{RP}$ color, the absolute G magnitude and a first guess metallicity. Running our code MyGIsFOS ([Sbordone et al. 2014](#)) with the first guess of the stellar parameters, we extracted the metallicity.

As discussed in [Cescutti et al. \(2022\)](#), the initial selection of the sample allowed the presence both of stars that are more metal-rich than -1.0 and of stars with $T_{\text{eff}} \leq 4000$ K, for both these kinds the spectral analysis is more complex due to line blending especially in the blue. A first scrutiny of the spectra resulted in defining a sample of 32 stars for which we were confident that a complete chemical inventory could be derived. Figure 1 shows the G_0 versus $(G_{BP} - G_{RP})_0$ color magnitude diagram (CMD) of the targets. We also highlight the stars exhibiting $H\alpha$ emission (red dots, see 4.1) and the Li-rich star (green symbol, see Sec. 4.2).

For the remaining stars with effective temperature above 4000 K we run MyGIsFOS limiting ourselves to the 437+760 spectral range, using the same grids and line selections detailed in [Caffau et al. \(2021, 2024\)](#). For the stars with $T_{\text{eff}} < 4000$ K we limited the analysis to the interval 840 nm – 874 nm, that corresponds roughly to the range covered by *Gaia* RVS and it is not contaminated by TiO. We computed a grid of synthetic spectra based on the grid of ATLAS 9 models of Mucciarelli et al. (in preparation). The grid covers effective temperatures from 3750 K to 5250 K at steps of 125 K surface gravities from 0.0 to 2.5 at steps of 0.5 dex, metallicities from -2.00 to $+0.25$ at steps of 0.25 dex, microturbulent velocities 1.2 and 3.0 km s^{-1} and $[\alpha/\text{Fe}] = 0.0$ and 0.4. For the atomic lines we adopted the list used by *Gaia* GP-Spec ([Contursi et al. 2021](#)).

For all stars, we refined the atmospheric parameters following the steps described above with the metallicities derived by MyGIsFOS, and then we run MyGIsFOS with the new stellar parameters. This process was iterated until it reached negligible changes in T_{eff} (10 K) and $\log g$ (0.05 dex). At any iteration, the microturbulence was derived from the calibration by [Mashonkina et al. \(2017\)](#).

The atmospheric parameters and the metallicity derived for 94 stars are listed in Table B.2. The 32 stars with a complete chemical inventory are highlighted in bold.

Five stars remain excluded from our analysis: two stars classified as RS CVn by *Gaia*, the SB2 binary CD –52 2441, the fast rotator CD –31 16922, and the fast rotator TY 5422-1192-1, that is a member of the Open Cluster NGC 2423, of metallicity $+0.12$.

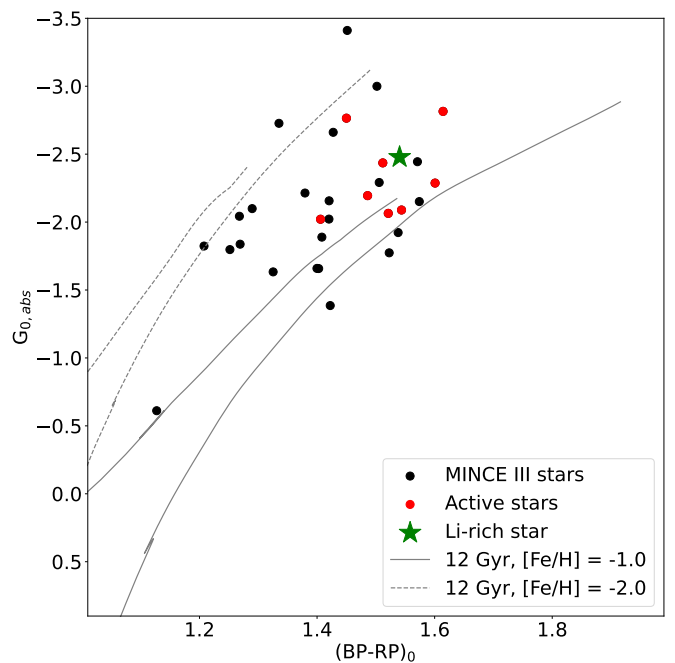


Fig. 1: G_0 versus $(G_{BP} - G_{RP})_0$ diagram of the sample. The stars exhibiting $H\alpha$ emission are reported in red. The green star symbol is the Li-rich star. The CMD is superimposed to the 12 Gyr BASTI isochrones ([Pietrinferni et al. 2021](#)) with metallicities $[\text{Fe}/\text{H}] = -1.0$ (solid grey line) and $[\text{Fe}/\text{H}] = -2.0$ (dashed grey line).

3.2. Kinematics

We evaluated the kinematics of the target stars using the astrometric data (coordinates, proper motions, parallaxes) and radial velocities (RVs) from *Gaia* DR3 ([Gaia Collaboration et al. 2022](#)) together with the `galpy` code² ([Bovy 2015](#)).

We adopted the default `MWPotential2014` Milky Way potential ([Bovy 2015](#)), solar distance and circular velocity at the solar distance of $r_0 = 8$ kpc, $v_0 = 220 \text{ km s}^{-1}$ ([Bovy et al. 2012](#)) and the solar motion from [Schönrich et al. \(2010\)](#). In order to evaluate the errors on the calculated quantities, similarly to [Bonifacio et al. \(2021\)](#), we employed the `pyia` code ([Price-Whelan 2018](#)) to extract, for each star, one thousand realizations of the six input parameters, using multivariate Gaussians, using the errors in the input parameters and taking into account the covariance matrix between the astrometric parameters.

Parallaxes were zero-point corrected following the prescription of [Lindegren et al. \(2021\)](#)³. The *Gaia* DR3 catalog does not report RVs for stars TYC 5422-1192-1 and CD-52 2441. For these stars we adopted the RVs measured from the UVES spectra. A negative parallax is assigned to star CD-35 14807 in *Gaia* DR3. For this star we adopted the photogeometric distance from [Bailer-Jones et al. \(2021\)](#).

Following [Bensby et al. \(2014\)](#), our targets can be divided into 42 with thin disk kinematics, 22 belonging to the thick disk and one of transition type between them. 34 stars are classified as belonging to the halo. Among the halo stars, 6 and 3 are kinematically similar to the Gaia-Sousage-Enceladus (GSE, [Belokurov et al. 2018; Haywood et al. 2018; Helmi et al. 2018](#)) and the

² <http://github.com/jobovy/galpy>

³ https://gitlab.com/icc-ub/public/gaiadr3_zeropoint

Sequoia (Seq, [Barbá et al. 2019](#); [Myeong et al. 2019](#); [Villanova et al. 2019](#)) structures, respectively, according to the criteria introduced by [Feuillet et al. \(2021\)](#). We report in Tables B.3 and B.4 some of the property evaluated for the target stars and their classification.

Putting the focus on the 32 metal-poor stars, none of these belong to the thin disk or are in transition between the thin and the thick disk. The whole sample can be divided into halo (23) and thick disk (9) stars. Moreover, among the halo stars, 4 and 2 are kinematically similar to GSE and Seq, respectively.

The top panels of Fig. 2 present the target stars in the Galactocentric cartesian Z vs cylindrical radius R plane (top-left), in the Galactocentric cartesian Y vs X plane (top-middle) and in the maximum height over the Galactic plane Z_{max} vs the apocentric distance r_{ap} plane (top-right). The bottom-left panel presents stars in the pericentric distance r_{peri} vs r_{ap} plane. The bottom-middle and bottom-right panels are a zoom-in of the top-right and bottom-left panels, respectively. The identity lines are also plotted in these panels to indicate the forbidden region above the line in the bottom-middle panel, and the locus of stars with zero eccentricity ($r_{peri}=r_{ap}$) in the bottom-right panel.

Stars classified as belonging to the thin disk (magenta), thick disk (cyan), thin-thick transition (blue) and the halo (black) are marked as filled circles. Candidate GSE and Seq members are marked with red squares and green diamonds, respectively.

Target stars are confined to distances lower than 3.7 kpc from the Sun, they reach out to about 10 kpc in the disk from the Galactic center and are found within 2.5 kpc from the plane (top panels). The middle panels reveal that a few stars classified as halo and GSE reach large Z_{max} and r_{ap} . Halo and GSE stars get to smaller r_{peri} distances than Seq, thick, transition and thin disk stars. This is due to the progressively lower eccentricity of the orbits of these objects, as can be better appreciated looking at the distance from the identity line (zero eccentricity: $r_{peri}=r_{ap}$) of the different categories of objects in the bottom-right panel. Notice that Seq candidates have extremely retrograde orbits which are, however, less eccentric than halo and GSE stars (see bottom-left panel in Figure 3).

Excluding 3 halo and 2 GSE stars, which reach $Z_{max} > 10$ kpc, the rest of the halo stars are confined to $Z_{max} < 7$ kpc (bottom-left panel) and, therefore, belong to the inner halo population. Most of the thin disk stars have $Z_{max} < 1$ kpc, but a few stars extend to $Z_{max} \approx 2$ kpc. Star classified as thick disk extend to Z_{max} up to 4 kpc and Seq stars to $Z_{max} < 3$ kpc. Notice here, that the classification between thin, thick, transition and halo stars is based on their current U_{lsr}, V_{lsr} and W_{lsr} velocity components.

Figure 3, presents the target stars in several commonly used planes to characterize the stellar orbits and kinematics ([Lane et al. 2022](#)), using the same symbols as in Fig. 2. The background gray dot population is the “good parallax sub-sample” studied in [Bonifacio et al. \(2021\)](#) which we use here for reference only.

The top-left and top-middle panels present a version of the Toomre diagram (the square root of the sum of the squares of the radial V_R and vertical V_Z velocity components in galactocentric cylindrical coordinates vs the transverse velocity component, V_T) and the V_T vs V_R plane, first used to identify the “Sausage” structure by [Belokurov et al. \(2018\)](#). The top-right panel is the usual total orbital energy E vs angular momentum L_Z plane. Bottom-panels present the eccentricity vs L_Z (left), the square root of the radial action J_R vs the azimuthal action ($J_\phi=L_Z$, middle) and the so called action diamond (right), namely the difference between the vertical and radial actions (J_Z-J_R) vs J_ϕ , both normalized to the total action $J_{tot}=J_R+|J_\phi|+J_Z$. In

the bottom-middle and bottom-right panels, the red and green shaded areas indicate the criteria adopted here from [Feuillet et al. \(2021\)](#) to select candidate GSE and Seq stars, namely $-500 < L_Z < +500$ kpc kms $^{-1}$ and $30 < \sqrt{J_R} < 55$ (kpc kms $^{-1}$) $^{1/2}$ for GSE and $(J_Z-J_R)/J_{tot} < 0.1$ and $J_\phi/J_{tot} < -0.6$, for Seq, respectively.

The different classes of objects are perhaps better separated in these planes. Thin, transition and thick disk stars have prograde orbits (V_T or $L_Z > 0$). Moving from thin to thick disk stars, the eccentricity of the orbits increases, together with J_R , V_R and V_Z , while $L_Z=J_\phi$, E and V_T all decrease. Sequoia stars have the most retrograde orbits in the sample.

Halos stars have, as expected, together with GSE stars, the most eccentric orbits. Including the GSE and Seq candidates, 21 out of 34 halos stars have prograde orbits. These number change to 18 out of 25 on prograde orbits, excluding the 9 stars belonging to GSE (6) and Seq (3). GSE stars have prograde and retrograde orbits in equal number (3). Considering only stars having $Z_{max} < 7$ kpc (and therefore $r_{ap} < 50$ kpc, $\sqrt{J_R} < 60$ kpc kms $^{-1}$, and $E < 0^4$, see Figs. 2 and 3), then we are left with 17 out of 22 (77%) stars on prograde orbits. This is consistent with these stars participating in a collapse process which gave rise to the inner halo and with the mostly prograde orbits (70%) found in very metal-poor stars ([Fe/H] < -2) at $1 < |Z| < 3$ kpc by [Carter et al. \(2021\)](#) using data of the H3 survey.

3.3. Abundances

We estimated the chemical abundances of the elements up to zinc using MyGIsFOS.

Regarding n-capture elements measurements, we used the Wrapper for Turbospectrum and Fitprofile (henceforth WTF), a python code that computes line profile fits from a synthetic spectra grid computed on the fly. From an input file defining the region(s) for line fitting and continuum pseudonormalization, the input atmosphere model, the observed spectrum to fit and the ion and abundance range for the calculation, WTF calls turbospectrum ([Alvarez & Plez 1998](#); [Plez 2012](#)) to compute a grid of small synthetic spectra around the region of interest, then launches Fitprofile ([Thygesen et al. 2016](#)) to compute the best-fitting synthetic. In this case Fitprofile is run with the abundance of the element of choice as the only free parameter. Finally WTF displays the fit result graphically.

In the present case, ATLAS9 ([Kurucz 2005](#)) models were computed for the parameters and the MyGIsFOS-derived abundance pattern for every star (elements for which we derived abundances in MyGIsFOS were put at the derived values, the others were set to the solar-scaled value for the star’s metallicity). WTF retains the Fitprofile capability to fit different features for the same ion either as separate, or as a single global fit. In this work, if multiple lines were present, each one was fitted separately.

In Table B.5, we provide the line list adopted for the star BD-11 3235 as an example, while the line list for the other targets can be found in the online material. The average abundances obtained are listed in Tables B.6 - B.10. The error reported is the line-to-line scatter (σ). However, to get the final error, the uncertainties due to atmospheric parameters should be added in

⁴ Notice that 3 stars have $E > 0$ in Fig. 3, upper right panel. These stars are, however, on bound orbits. In fact, their space velocities are lower than the escape velocities at their distances. It is a known and documented feature that “galpy potentials do not necessarily approach zero at infinity”. This is indeed the case of [MWPotential2014](#).

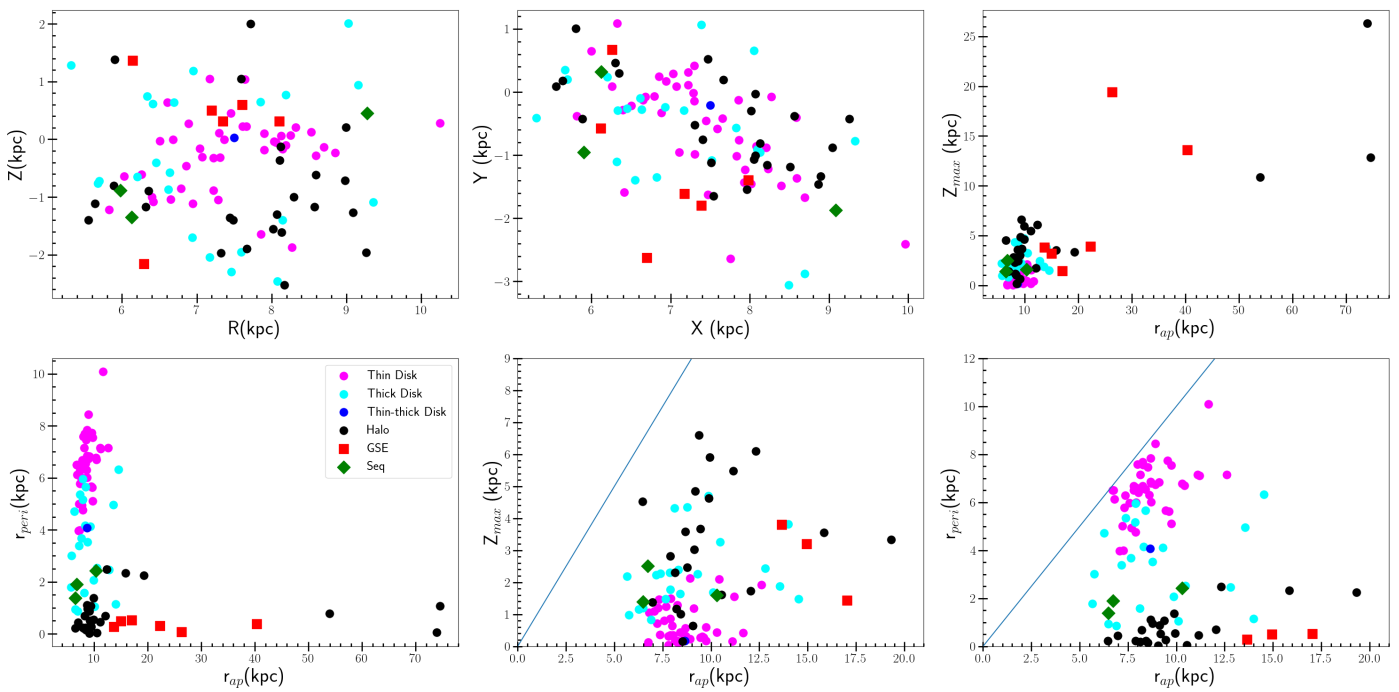


Fig. 2: Top-panels: left: Galactocentric Cartesian height over the galactic plane Z vs cylindrical galactocentric radius R . Middle: targets' Galactocentric Cartesian X vs Y coordinates. Right: maximum height over the galactic plane Z_{max} vs apocentric distance r_{ap} . Bottom-panels: left: pericentric distance r_{peri} vs r_{ap} . Middle: zoom-in of the top-right panel. The region above the line is forbidden. Right: zoom-in of the bottom-left panel. The stars with zero eccentricity lie on the line $r_{peri}=r_{ap}$. Targets classified as belonging to the thin (magenta) or thick disk (cyan), thin-thick transition (blue) and halo (black) are presented as filled circles. Candidate GSE and Seq stars are denoted with red squares and green diamonds, respectively.

quadrature.

We estimated these last uncertainties for the star BD-11 3235 by varying $\Delta T_{\text{eff}} = \pm 100$ K, $\Delta \log g = \pm 0.2$ dex, and $\Delta \xi = \pm 0.2$ km s^{-1} . We considered this star because its atmospheric parameters are representative of the sample and all the elements have been measured for it. The typical errors due to atmospheric parameters are reported in Table 1 for all chemical species analyzed here. Similar results have been found for the first sample of metal-poor giant stars analyzed by the MINCE collaboration (Cescutti et al. 2022; François et al. 2024, hereafter the MINCE I sample). The solar abundances adopted in this work are listed in Table 2.

Finally, we want to highlight that we used $[\text{X}/\text{Fe}] = [\text{X}/\text{Fe I}]$ or $[\text{X}/\text{Fe}] = [\text{X}/\text{Fe II}]$ when X is a neutral or ionised species, respectively.

The sulfur abundances $A(\text{S})$ were measured following a different procedure. In the wavelength ranges covered by the spectral frames centered at 580 and 760 nm lie the Sulfur (S) lines of Mult. 6, 8, and 1. These lines are of high excitation, thus, they become weak at low temperatures and in the metal-poor regime. We rejected the S lines at bluer wavelengths (Mult. 6, 8) because too weak, and we considered only the strongest features at 920 nm (Mult. 1).

The contamination due to telluric lines in this wavelength region makes difficult the standard workflow of MyGIsFOS. In particular, the pseudonormalization of the observed spectrum is hampered when a telluric line falls in a continuum region. Moreover, since MyGIsFOS does not take into account the presence of telluric lines, blended or shape distorted lines are not recognized by the code. Therefore, depending on the degree of telluric contamination, MyGIsFOS rejects S lines or overestimates the abundances. For these reasons, we decided to derive $A(\text{S})$ from

equivalent width (EW).

We first compared the observed spectra of our stars with that of a B-type star to evaluate the suitability of Mult. 1 lines. S lines contaminated by telluric lines were rejected. This reduced our sample to a total of 23 stars.

Using the deblending option of the IRAF⁵ task `splot`, we took into account the contribution in EW from the telluric and S lines. The conversion from EW to abundances was computed through the code GALA (Mucciarelli et al. 2013), that is a user-friendly wrapper for WIDTH9 (Kurucz 2005). The results obtained for sulfur are reported in Table B.11.

3.4. Non-local thermodynamic equilibrium effects

Among the elements analyzed in this work, some are known for being sensitive to deviation from LTE, or NLTE effects. In this work, the chemical investigation was performed under the assumption of LTE, similar to what done in the first two papers of the series: Cescutti et al. (2022) and François et al. (2024). The intervals in metallicity, effective temperature and surface gravity spanned by the present sample is similar to that of the sample analysed in Cescutti et al. (2022) and François et al. (2024). We defer a more complete analysis of the NLTE effects to a future investigation on the complete sample. To provide an indication of the magnitude of NLTE effects we are dealing with, in Cescutti et al. (2022) we took advantage of the thorough investigation by Hansen et al. (2020). In Table 9 of Cescutti et al. (2022), we provided the NLTE corrections from Hansen et al. (2020) for BD-10 3742 ($T_{\text{eff}}, \log g, [\text{Fe}/\text{H}], \xi$: 4678 K, 1.38, -1.96, 1.9 km s^{-1}) and BD-12 106 (4889 K, 2.03, -2.11,

⁵ <https://iraf-community.github.io/>

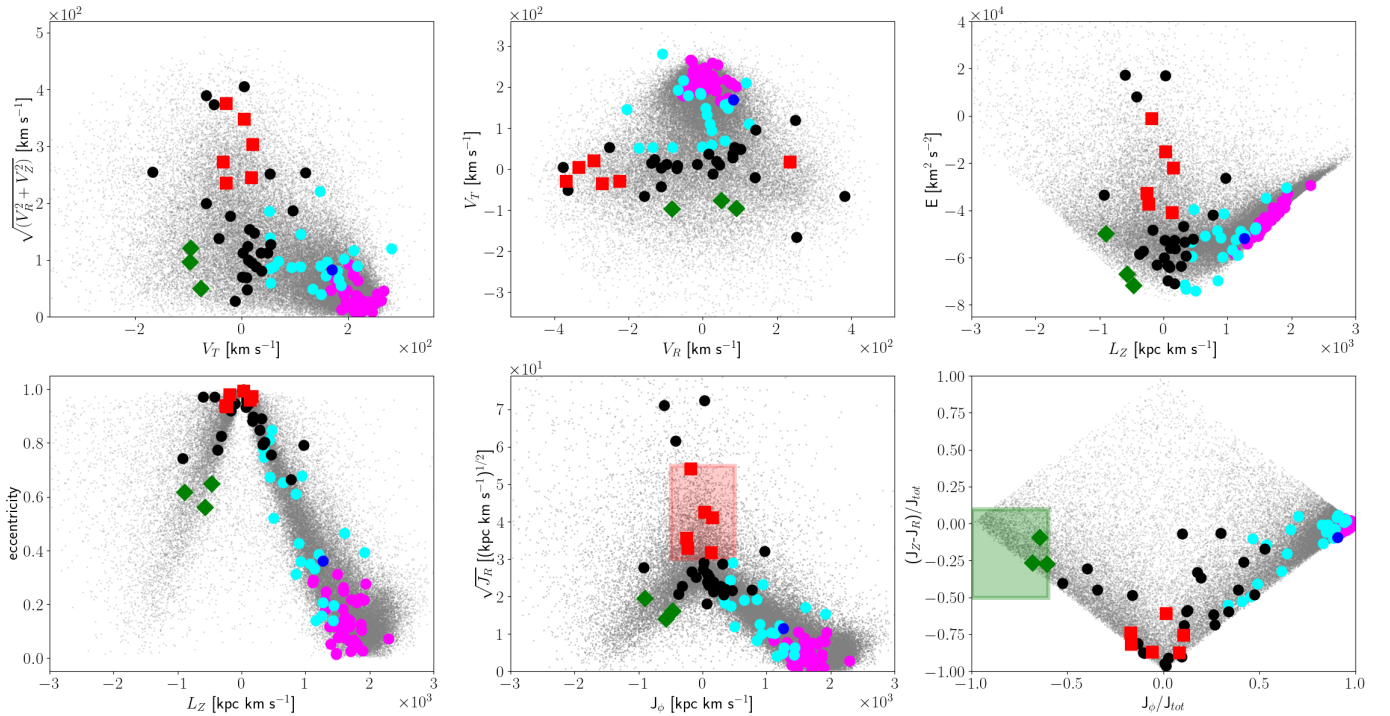


Fig. 3: Upper panels: left: Toomre diagram ($\sqrt{V_R^2 + V_Z^2}$ vs V_T). V_R , V_Z , V_T are the stars' velocity components in galactocentric cylindrical coordinates. Middle: V_R vs V_T . Right: Orbital energy E vs angular momentum L_Z . Bottom panels: left: orbital eccentricity vs L_Z . Middle: $\sqrt{J_R}$ vs J_ϕ , where J_R and $J_\phi = L_Z$ indicate the radial and azimuthal actions. Right: action diamond, namely the difference between the vertical and radial actions ($J_z - J_R$) vs J_ϕ , both of them normalized to the total action $J_{tot} = J_R + |J_\phi| + J_z$. The red (middle panel) and green (right panel) shaded areas indicate the criteria adopted here from [Feuillet et al. \(2021\)](#) to select candidate GSE and Seq stars, respectively. Gray dots are stars from the “good parallax sample” of [Bonifacio et al. \(2021\)](#). The colored symbols are the same as in Fig. 2.

1.5 km s $^{-1}$). These two stars have parameters close to those of BD+07 4625 and BD+39 3309 in the MINCE I sample and to those of CD-52 976 (4655 K, 1.29, -1.90, 1.97 km s $^{-1}$) and BD-19 3663 (4767 K, 1.82, -2.51, 1.82 km s $^{-1}$) in the present sample. We therefore refer the reader to the discussion in [Cescutti et al. \(2022\)](#) and table 9 to have an indication of the NLTE corrections we should be dealing with. Another relevant paper is [Matas Pinto et al. \(2021\)](#) who provide NLTE corrections for two stars with stellar parameters similar to the stars here investigated. From this comparison, we conclude that for all elements, except Na I and Co I, the NLTE corrections are smaller than the typical uncertainty on the abundances and they are positive, as NLTE corrections for Fe, becoming even smaller when using [X/Fe]. Therefore, the comparison of LTE abundances with chemical evolution models is meaningful. There are not many NLTE computations available for neutron capture elements, but a discussion of NLTE corrections for Sr, Eu and Ba can be found in [François et al. \(2024\)](#).

4. Discussion

In the following section are shown the results obtained for the MINCE III stars.

4.1. The stars exhibiting H α emission

We realised that some stars in the sample show P-Cygni and/or inverse P-Cygni profile, a signature of stellar activity.

In Figure 1, the stars with activity (red dots) are among the brightest and reddest in the sample, as expected by [Smith & Dupree \(1988\)](#), see their Figure 1).

The stars in question are: BD-11 3235, BD-13 934, BD-15 5449, CD-28 17446, CD-33 15063, CD-39 9313, HD 19367 and TYC 8633-2281-1. The spectra of the H α line of these stars are shown in Figure 4. BD-11 3235 is the only star with symmetric H α emission wings. In BD-13 934, CD-28 17446, CD-33 15063 and HD 19367, the blue wing is stronger than the red one, while the remaining stars show the opposite profile.

Finally, for these active stars, one must be cautious not to use lines whose contribution also comes from the chromosphere, such as the Ca II triplet lines, the Na I-D lines or the K I line at 769.9 nm, lines that have not been used in this investigation.

4.2. The Li-rich star: CD-28 10039

The star CD-28 10039 has A(Li) = 1.1, which is not expected for a star of this log g . According to our kinematic results, this star belongs to the thick disk.

To check the evolutionary state of this star, we considered two BASTI isochrones ([Pietrinferni et al. 2021](#)) characterized by [Fe/H] = -1.0 and -2.0, [α/Fe] = +0.4, and Age = 12 Gyr. In Figure 1, CD-28 10038 (green star symbol) lies close to the asymptotic-giants branch of the isochrone with [Fe/H] = -1.0.

We reported CD-28 10039 in the A(Li) versus log g diagram (green star symbol in Figure 5). The evolution of Li with log g is characterized by the Spite Plateau (A(Li) ~ 2.2 dex, [Spite &](#)

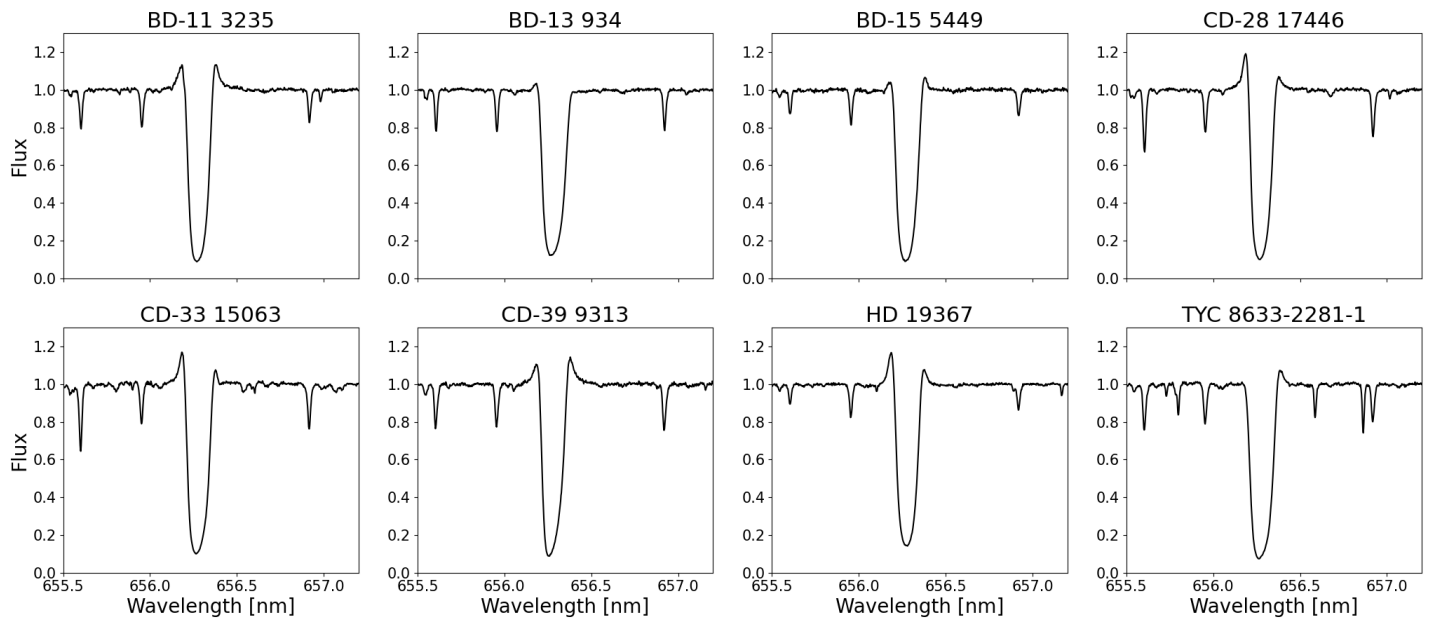


Fig. 4: Spectra of the H α line of the stars exhibiting P-Cygni and/or inverse P-Cygni profile.

Spite 1982), followed by the First Dredge-Up (FDU) drop until the RGB Plateau ($A(\text{Li}) \sim 1$ dex, Mucciarelli et al. 2012, 2022), which is followed by another drop due to the RGB bump (RGBb) mixing episode. In this diagram, the unexpected position of CD-28 10039, slightly above the RGB Plateau at low $\log g$, reveals that the Li enhancement of this star is not due to standard stellar evolution (Iben 1967) or non-canonical mixing processes (Charbonnel et al. 2020; Magrini et al. 2021).

The spectra of CD-28 10039 (red) are compared with those of the star with similar parameters CD-27 16505 (black) in Fig. 6. The top panel shows the evident difference in strength of the Li line at 670.78 nm between the two stars. The reddest line of the Mg II triplet at 518.36 nm seems similar in both stars (second panel from the top), suggesting that the Li enhancement of CD-28 10032 is not due to rotation effects. The H α and the reddest line of the Ca II triplet at 866.21 nm are reported in the last two panels. From these two features it is possible to notice slight differences between the Li-rich and the reference stars. The H α of the Li-rich star seems shallower, with asymmetrical core and blue wing. On the other hand, the red wing of the reddest line of the Ca II triplet appears shallower in the Li-rich stars than in the reference one. These anomalous profiles could be compatible with chromospheric activity and mass loss (Meszaros et al. 2008). However, the H α blue wing of CD-27 16505 recall a slight emission profile, so it could be possible that we are comparing two active stars.

From the chemical point of view, CD-28 10039 has $A(Y) = 1.17 \pm 0.00$ and $A(\text{Ba}) = 1.34 \pm 0.09$. These values are not discrepant with those of the sample. For instance, we obtained $A(Y) = 1.01 \pm 0.10$ and $A(\text{Ba}) = 1.14 \pm 0.00$ in CD-27 16505. Comparing the abundances of the *s*-process elements, in the Li-rich star, the ratio $[\text{Rb}/Y] = -0.06$ dex suggests a low neutron density at the sites of these elements (Smith & Lambert 1984). Moreover, we find a similar *r*-process elements enrichment for the Li-rich star, $A(\text{Eu})=0.04$ dex, and CD-27 16505, $A(\text{Eu})=0.05$ dex.

We present in Figure 7 the Spectral Energy Distribution (SED, red and yellow points) of CD-28 10039, which we con-

structed using the Virtual Observatory SED Analyzer (VOSA⁶, Bayo et al. 2008) service. The SED was generated adopting the stellar distance and extinction, namely $d=2.14$ kpc and $A_V = 0.22$ mag. We fitted the SED using Kurucz ATLAS9 model atmospheres calculated with new opacity distribution functions and no overshooting (Castelli & Kurucz 2003), allowing for a narrow range of parameters, around those we adopted here for the star. The best fitting model (blue points and line) obtained with the parameters indicated in the top-label of the Figure, seems a fair representation of the stellar SED all over the wavelength range, but for the Near Ultra Violet (NUV) GALEX photometry at 2303.37Å. In fact, CD-28 10039 appears to present a significant NUV excess, which may be indicating the presence of a hot companion, like a white dwarf.

On the other hand, the radial velocity measured from the UVES spectra and that reported in *Gaia* DR3, are very similar (RV difference of less than 0.5 km s^{-1}) to each other. Furthermore, the *Gaia* DR3 astrometry quality parameters are not suggestive of binarity: RUWE=1.13, astrometric_gof_al=2.79, astrometric_excess_noise = 0.09 mas, although astrometric_excess_noise_sig = 10.1.

Finally, *Gaia* DR3 does not report variability information for CD-28 10039 (phot_variable_flag="NOT_AVAILABLE"). However, the star is reported as variable in G, G_{BP} and G_{RP} (VarF=VVV), according to the analysis of Maíz Apellániz et al. (2023).

4.3. α -elements

Figure 8 shows our results for the α -elements Mg, Si, Ca, and Ti. The stars belonging to the Galactic halo (black dots), Galactic thick-disk (cyan dots), GSE (red squares), and Sequoia (green diamonds) substructures are distinguished by colors and symbols. The good agreement with the first results of the MINCE series (Cescutti et al. 2022) is shown adopting the same colors and smaller symbols. As comparison, we reported the results of

⁶ <http://svo2.cab.inta-csic.es/theory/vosa/>

Table 1: Sensitivity of abundances on atmospheric parameters.

Element	ΔT_{eff} 100 K	$\Delta \log g$ 0.2 dex	$\Delta \xi$ 0.2 km s^{-1}
Na I	0.08	0.02	0.01
Mg I	0.04	0.06	0.03
Al I	0.06	0.01	0.00
Si I	0.04	0.03	0.00
S I	0.18	0.09	0.03
Ca I	0.12	0.02	0.03
Sc II	0.04	0.14	0.02
Ti I	0.18	0.01	0.01
Ti II	0.02	0.14	0.11
V I	0.20	0.02	0.01
Cr I	0.14	0.02	0.01
Cr II	0.04	0.06	0.02
Mn I	0.17	0.02	0.01
Fe I	0.09	0.01	0.04
Fe II	0.07	0.06	0.02
Co I	0.11	0.02	0.00
Ni I	0.08	0.03	0.03
Cu I	0.17	0.01	0.00
Zn I	0.07	0.06	0.04
Sr I	0.19	0.02	0.02
Y II	0.03	0.12	0.06
Zr II	0.01	0.08	0.02
Ba II	0.03	0.08	0.18
La II	0.08	0.11	0.07
Ce II	0.13	0.11	0.02
Pr II	0.08	0.13	0.05
Nd II	0.07	0.11	0.02
Sm II	0.05	0.14	0.07
Eu II	0.03	0.14	0.04

Note. Sulfur results were obtained with GALA.

Lombardo et al. (2022) obtained from the CERES survey in gray. This legend will be maintained for the rest of the section. The stars of the different substructures seem to share the same plateau trend in all panels in the metallicity range $-2.5 < [\text{Fe}/\text{H}] < -1.5$. Moreover, due to the low number of GSE, and Sequoia stars, it is not possible to draw further conclusions about the differences between MW, GSE and Sequoia members.

All the α -elements are enhanced with respect to the $[\text{Fe}/\text{H}]$ abundances with sample averages and standard deviations of $\langle [\text{Mg}/\text{Fe}] \rangle = 0.49 \pm 0.08$, $\langle [\text{Si}/\text{Fe}] \rangle = 0.39 \pm 0.09$, $\langle [\text{Ca}/\text{Fe}] \rangle = 0.36 \pm 0.09$ and $\langle [\text{Ti}/\text{Fe}] \rangle = 0.34 \pm 0.09$.

We also estimated the $[\text{Ti II}/\text{Fe II}]$ ratio. In particular, the mean abundances ratio is 0.42 ± 0.14 , and the mean difference between $[\text{Ti II}/\text{Fe II}]$ and $[\text{Ti I}/\text{Fe I}]$ is 0.08 ± 0.14 . The NLTE effects for Ti I lines (Mashonkina et al. 2016) may explain the fact that the ionization equilibrium of Ti is not established, although the offset is not very significant. These results are in agreement, within errors, with those in the literature (see e.g. Cescutti et al. 2022; Lombardo et al. 2022).

Figure 9 compares the sulfur results before (left panel) and after (right panel) NLTE corrections. In the left panel, we can guess the presence of a plateau at the value $[\text{S}/\text{Fe}]_{\text{LTE}} \sim 0.64$. This quantity is considerably higher than both the usual $[\alpha/\text{Fe}] \sim 0.40$ and $[\text{S}/\text{Fe}] \sim 0.30$ values in the literature (Caffau et al. 2010; Nissen et al. 2007). After NLTE corrections, the $[\text{S}/\text{Fe}]$ ratios present a larger scatter but the plateau value, $\langle [\text{S}/\text{Fe}] \rangle = 0.45 \pm 0.19$, is in better agreement with the typical $[\alpha/\text{Fe}]$ abundance ratio. The large scatter in $[\text{S}/\text{Fe}]$ is introduced by the difficulties

Table 2: Solar abundances used throughout this paper.

Element	A(X)	Reference
Na	6.30	Lodders et al. (2009)
Mg	7.54	Lodders et al. (2009)
Al	6.47	Lodders et al. (2009)
Si	7.52	Lodders et al. (2009)
S	7.16	Caffau et al. (2011)
Ca	6.33	Lodders et al. (2009)
Sc	3.10	Lodders et al. (2009)
Ti	4.90	Lodders et al. (2009)
V	4.00	Lodders et al. (2009)
Cr	5.64	Lodders et al. (2009)
Mn	5.37	Lodders et al. (2009)
Fe	7.52	Caffau et al. (2011)
Co	4.92	Lodders et al. (2009)
Ni	6.23	Lodders et al. (2009)
Cu	4.21	Lodders et al. (2009)
Zn	4.62	Lodders et al. (2009)
Rb	2.60	Lodders et al. (2009)
Sr	2.92	Lodders et al. (2009)
Y	2.21	Lodders et al. (2009)
Zr	2.58	Lodders et al. (2009)
La	1.14	Lodders et al. (2009)
Ce	1.61	Lodders et al. (2009)
Pr	0.76	Lodders et al. (2009)
Nd	1.45	Lodders et al. (2009)
Sm	1.00	Lodders et al. (2009)
Eu	0.52	Lodders et al. (2009)
Ba	2.17	Lodders et al. (2009)

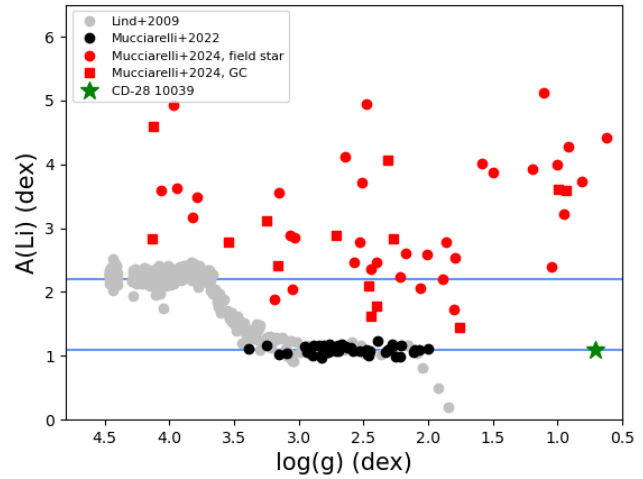


Fig. 5: $A(\text{Li})$ versus $\log g$ diagram for CD-28 10039 in comparison with literature data: Lind et al. (2009, grey), Mucciarelli et al. (2022, black), Mucciarelli et al. (2024, red). The blue lines are the Spite ($A(\text{Li}) \sim 2.2$, Spite & Spite 1982) and RGB ($A(\text{Li}) \sim 1.1$, Mucciarelli et al. 2012) Plateaus.

in the $A(\text{S})$ estimation, such as the telluric contamination and the NLTE corrections.

In Figures 8 and 9, we notice a peculiar star with low α -elements content. The MW halo star CD-38 13823 is Mg-rich ($[\text{Mg}/\text{Fe}] = 0.49$), as expected for its metallicity ($[\text{Fe}/\text{H}] = -2.46$), slightly poor in $[\text{Si}/\text{Fe}] = 0.27$ and $[\text{S}/\text{Fe}] = 0.26$, and with solar ratios of $[\text{Ca}/\text{Fe}] = 0.06$ and $[\text{Ti}/\text{Fe}] = 0.06$.

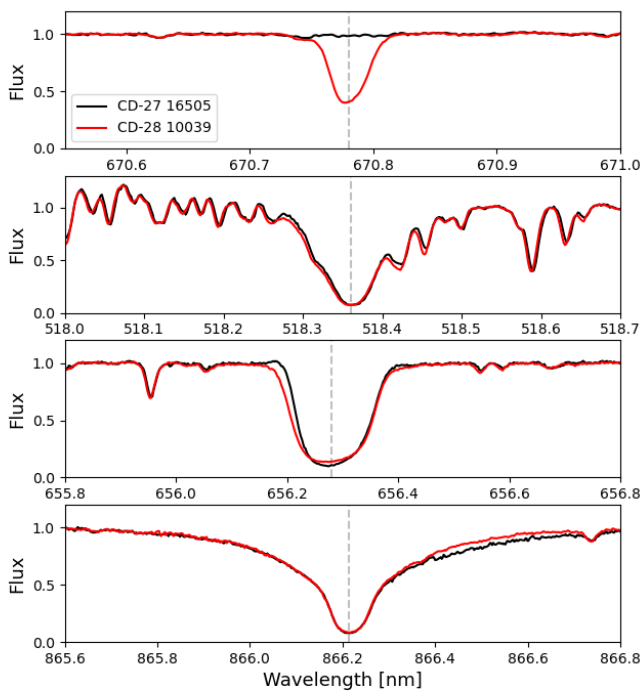


Fig. 6: Comparison of the spectra of the Li-rich star CD-28 10039 (red) with that of CD-27 1605 (black) in different wavelength regions. From the top to bottom: Li doublet at 670.7 nm, reddest line of the Mg II triplet at 518.36 nm, H α at 656.28 nm, and the reddest line of the Ca II triplet at 866.21 nm.

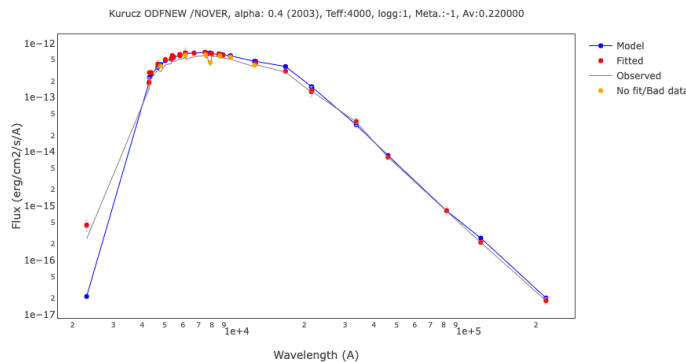


Fig. 7: Spectral energy distribution of CD-28 10039 obtained from the VOSA service. The model obtained with the parameters indicated in the toplabel is shown in blue. An apparent NUV excess is detected from the GALAX photometry.

4.4. Light-odd elements

Figure 10 shows our results for the light-odd elements Na, Al, Sc, and V. The stars of the different kinematic components are identified with the same colors and symbols as in Fig. 8. In the following we shall comment on which lines were used to determine the abundances in the MINCE III sample.

The Na abundances were derived from the Na I lines at 498.3 nm, 568.2 nm, 568.8 nm, the Na D resonance lines at 588.9 nm (D1) and 589.5 nm (D2), and 616.1 nm. The large dispersion $\langle [\text{Na}/\text{Fe}] \rangle = -0.08 \pm 0.15$ may be due to the LTE

deviations of these lines. In our sample in three halo stars, two thick-disk stars and one Sequoia candidate, the Na is enhanced over iron. However, the limited size of the sample does not allow us to draw any robust conclusion about the differences between MW and GSE stars.

The Al abundances were derived from the Al I resonance lines at 394.4 nm and 396.1 nm as well as from the Al I lines at 555.6 nm, and the doublet at 669.6 nm and 669.8 nm. However, the Al I resonance lines were rejected for most of the stars to estimate the final Al abundances. Inspection of Fig. 10 shows that the [Al/Fe] ratio is quite scattered spanning a range of almost 0.8 dex. The mean value is $\langle [\text{Al}/\text{Fe}] \rangle = 0.16$ dex with a standard deviation of 0.26 dex. The dispersion is driven by four Al-enhanced stars, two of which belong to the MW halo, one to the MW thick-disk, and one to GSE. The MINCE I sample shows similar scatter and dispersion. In Fig. 10, the [Na/Fe] and [Al/Fe] ratios do not show clear trends with the metallicity.

We determined the mean abundance ratios of Sc and V ions to the corresponding Fe ions. The ratios and their corresponding standard deviations are: $\langle [\text{Sc I}/\text{Fe I}] \rangle = -0.01 \pm 0.13$, $\langle [\text{Sc II}/\text{Fe II}] \rangle = 0.28 \pm 0.15$, $\langle [\text{V I}/\text{Fe I}] \rangle = -0.01 \pm 0.08$, and $\langle [\text{V II}/\text{Fe II}] \rangle = 0.02 \pm 0.15$. Thus, while the mean difference between [Sc II/Fe II] and [Sc I/Fe I] is about 0.29 ± 0.17 , the one between [V II/Fe II] and [V I/Fe I] is only of 0.03 ± 0.17 . These results agree within errors with those obtained by Lombardo et al. (2022) in a sample of lower metallicity giant stars. We notice a slight increase in the [Sc II/Fe] and [V I/Fe] ratios with metallicity.

In Fig. 10, CD-38 13823 shows a low [Sc/Fe] ratio of about -0.17 , and it is slightly poor in [Na/Fe] = -0.38 and [V/Fe] = -0.26 . We could not measure the Al abundance for this star.

4.5. Iron-peak elements

Figure 11 shows our results for the iron-peak elements Cr, Mn, Co, Ni, Cu, and Zn. The first five of these elements are produced in nuclear statistical equilibrium in SNe of all types, like iron, so their ratio to iron are expected to be close to the solar value. The situation is less clear for Zn, that may have contribution from α -rich freeze-out and from neutron captures (see Duffau et al. 2017, for a discussion on the nucleosynthesis of Zn). In the MINCE III sample Cr, Ni, Co, and Zn have mean abundance ratios close to solar: $\langle [\text{Cr}/\text{Fe}] \rangle = 0.00 \pm 0.06$, $\langle [\text{Co}/\text{Fe}] \rangle = 0.09 \pm 0.06$, $\langle [\text{Ni}/\text{Fe}] \rangle = 0.00 \pm 0.03$, and $\langle [\text{Zn}/\text{Fe}] \rangle = -0.02 \pm 0.13$. Co and Ni display flat trends, while Cr and Zn exhibit increasing and decreasing trends with metallicity, respectively. Previous studies have found similar behavior for these elements (Cayrel et al. 2004; Bonifacio et al. 2009; Ishigaki et al. 2013; Cescutti et al. 2022; Lombardo et al. 2022).

The iron-peak elements showing exceptional behavior are Mn and Cu. Indeed, we observe sub-solar trends for these elements, which slightly increasing with metallicity. Similar behaviors have been noted by Ishigaki et al. (2013) and Cescutti et al. (2022).

Manganese is produced by both SNe Ia and SNe II, like the other iron peak elements; however, the contribution by SNe Ia at solar metallicity is higher compared to iron, leading to a speculate trend to that of the α -elements. Moreover, Mn yields from SNe Ia are the most dependent to the explosion mechanism among the iron peak elements and its evolution can be used to evaluate the presence and contribution of different SNe Ia channels (Cescutti & Kobayashi 2017; Seitzenzahl et al. 2013). The nucleosynthesis of Cu is also peculiar. According to Timmes et al. (1995), the explosion of massive stars at solar metallicity

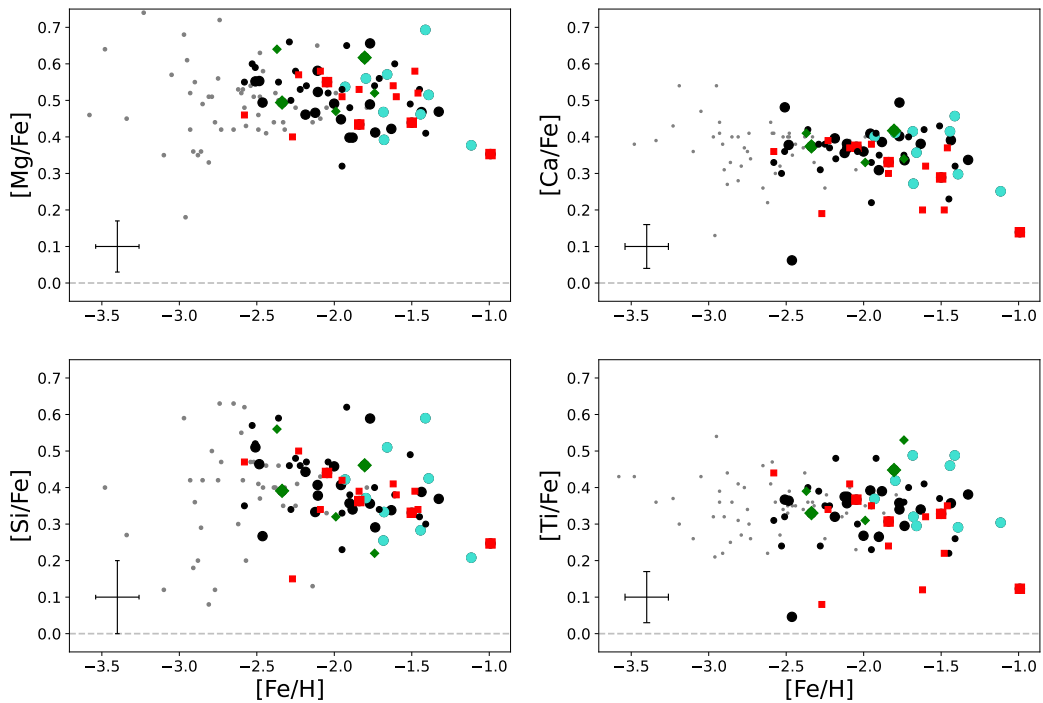


Fig. 8: α -elements abundances measured in the MINCE III stars. Black and cyan points are Galactic stars belonging to the halo and thick-disk, respectively. Candidate Gaia-Sausage-Enceladus (red squares) and Sequoia (green diamonds) stars are also shown. The results of Cescutti et al. (2022) for the same substructures in the MINCE I sample are reported with same colors and smaller symbols. The gray points are the results of Lombardo et al. (2022)

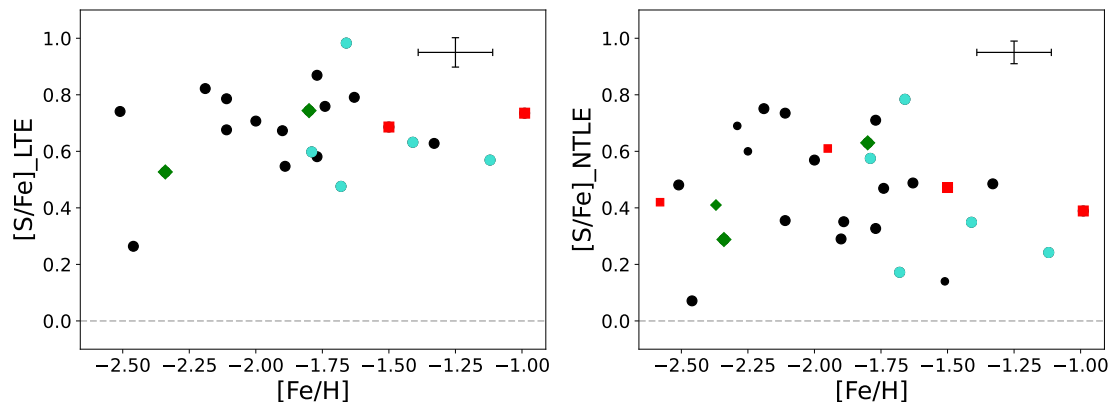


Fig. 9: [S/Fe] versus [Fe/H] LTE (left panel) and NLTE (right panel) diagrams of the MINCE sample, the MINCE I sample (Cescutti et al. 2022) is identified by smaller symbols. Colors and symbols are the same in Figure 8.

ity produces yields 5 times larger than the same explosion at low metallicity. Therefore it is the metal dependencies of SNe II that produce the rise rather than the SNe type-Ia. The behavior of Mn may also be due to the strong NLTE effects on the lines of these elements (Bergemann & Gehren 2008). However, the use of NLTE corrections decreases the trend with metallicity, but does not cancel it, suggesting that there is a role of SNe Ia in Mn nucleosynthesis (Eitner et al. 2020). Among the stars of the MINCE III sample, CD-38 13823 is the most Mn-rich, $[\text{Mn}/\text{Fe}] = -0.10$, and the most Cu-poor, $[\text{Cu}/\text{Fe}] = -0.78$.

This star does not show peculiar values for the other iron-peak elements in comparison to the other targets.

The mean abundance ratios and their standard deviations for Mn and Cu ions to the corresponding Fe ions are: $\langle [\text{Cr I}/\text{Fe I}] \rangle = 0.00 \pm 0.06$, $\langle [\text{Cr II}/\text{Fe II}] \rangle = 0.11 \pm 0.12$, $\langle [\text{Mn I}/\text{Fe I}] \rangle = -0.27 \pm 0.07$, $\langle [\text{Mn II}/\text{Fe II}] \rangle = -0.23 \pm 0.06$. Thus, the ionisation equilibrium is reached in LTE for both Cr and Mn. Our results are in perfect agreement with those found by Lombardo et al. (2022).

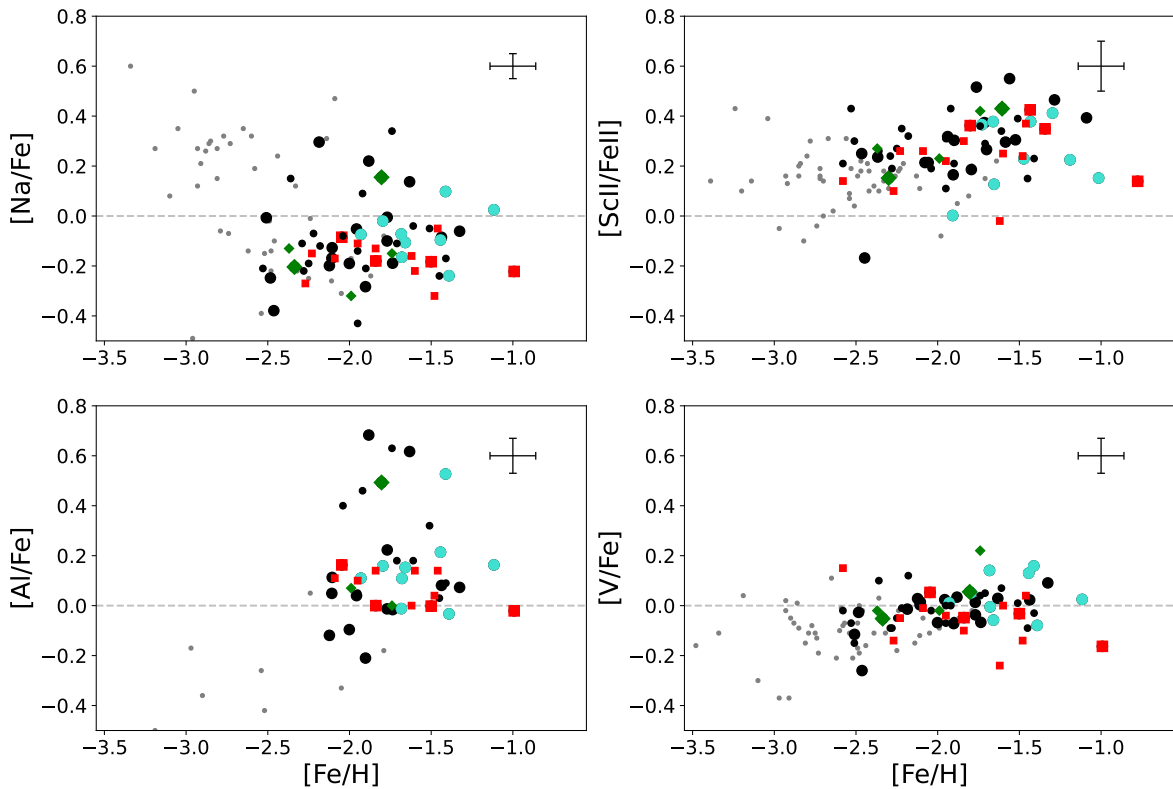


Fig. 10: Light-odd elements abundances measured in the MINCE stars, the MINCE I sample (Cescutti et al. 2022) is identified by smaller symbols. Colors and symbols are the same as in Figure 8.

4.6. Neutron capture elements

Figure 12 displays our results for the n-capture elements Rb, Sr, Y, Zr, Ba, La, Ce, Pr, Nd, Sm and Eu. The different MW substructures are shown with the same colors and symbols as in Figure 8. The gray points are from Lombardo et al. (2022); Lombardo (2023). Our results are generally in agreement with the analysis of the MINCE I sample (smaller symbols François et al. 2024).

We observed flat trends for all the n-capture elements with the exception of Sr and Ba. Sr decreases with increasing metallicity, while Ba increases. Similar behaviors have also been noted in other studies (François et al. 2007; Ishigaki et al. 2013; Lombardo et al. 2022). In particular, we found sub-solar mean abundances ratios and standard deviation for $\langle [\text{Sr}/\text{Fe}] \rangle = -0.41 \pm 0.28$. The mean abundances of $\langle [\text{Y}/\text{Fe}] \rangle = -0.09 \pm 0.19$, $\langle [\text{La}/\text{Fe}] \rangle = 0.08 \pm 0.22$ and $\langle [\text{Ce}/\text{Fe}] \rangle = 0.01 \pm 0.21$ are close to solar. Finally, we found mean abundances above solar for $\langle [\text{Zr}/\text{Fe}] \rangle = 0.38 \pm 0.21$, $\langle [\text{Ba}/\text{Fe}] \rangle = 0.13 \pm 0.26$, $\langle [\text{Pr}/\text{Fe}] \rangle = 0.11 \pm 0.17$, $\langle [\text{Nd}/\text{Fe}] \rangle = 0.16 \pm 0.21$, $\langle [\text{Sm}/\text{Fe}] \rangle = 0.31 \pm 0.19$, and $\langle [\text{Eu}/\text{Fe}] \rangle = 0.43 \pm 0.21$.

Considering both the MINCE I (François et al. 2024) and the present samples, we find an indication of a slight increase in the n-capture elements scatter with decreasing metallicity. This is more visible in the trends of Ba, La and Eu. The comparison with the results of Lombardo et al. (2022); Lombardo (2023) allows to better visualize this effect. The MW, GSE and Sequoia stars seem to behave similarly for all elements (see Fig. 12). However,

a larger sample for each substructure is required to draw firmer conclusions.

The *s*-process elements content of CD-38 13823 is low: $[\text{Y}/\text{Fe}] = -0.70$, $[\text{Zr}/\text{Fe}] = -0.39$, $[\text{Ba}/\text{Fe}] = -0.72$, $[\text{La}/\text{Fe}] = -0.49$. On the other hand, in comparison to the other stars of the sample, it is also the poorest one in $[\text{Sm}/\text{Fe}] = -0.24$ and $[\text{Eu}/\text{Fe}] = -0.03$.

The $[\text{Eu}/\text{Ba}]$ versus $[\text{Ba}/\text{H}]$ diagram in Fig. 13 allowed us to discriminate the origin of the n-capture elements enrichment. In this plot, the (almost) Eu-free stars lie at $[\text{Ba}/\text{H}] \leq -3$ (Cescutti et al. 2015a; Cavallo et al. 2021), the enrichment in the range $-2.5 < [\text{Ba}/\text{H}] < -1.5$ may be attributed to rotating massive stars, while AGB stars are likely responsible for the enrichment at $[\text{Ba}/\text{H}] > -1$. The *r*-process pollution occurs at $[\text{Eu}/\text{Ba}] > 1$. Our sample of stars appears to define a flat trend up to $[\text{Ba}/\text{H}] \sim -1.0$. The Li-rich star, CD-28 10039, lies in the area polluted by AGB stars, while the position of the peculiar star, CD-38 13823, supports its low Eu-content.

5. Chemical evolution model

We compare our results with a stochastic chemical evolution model (Cescutti & Chiappini 2014; Cescutti et al. 2015a) that traces Rb, Sr, Y, Zr, Ba, La, and Eu as well as the α elements Mg, Ca, Si, Ti, the light-odd element Sc, and the iron peak elements Mn, Co, Ni and Zn.

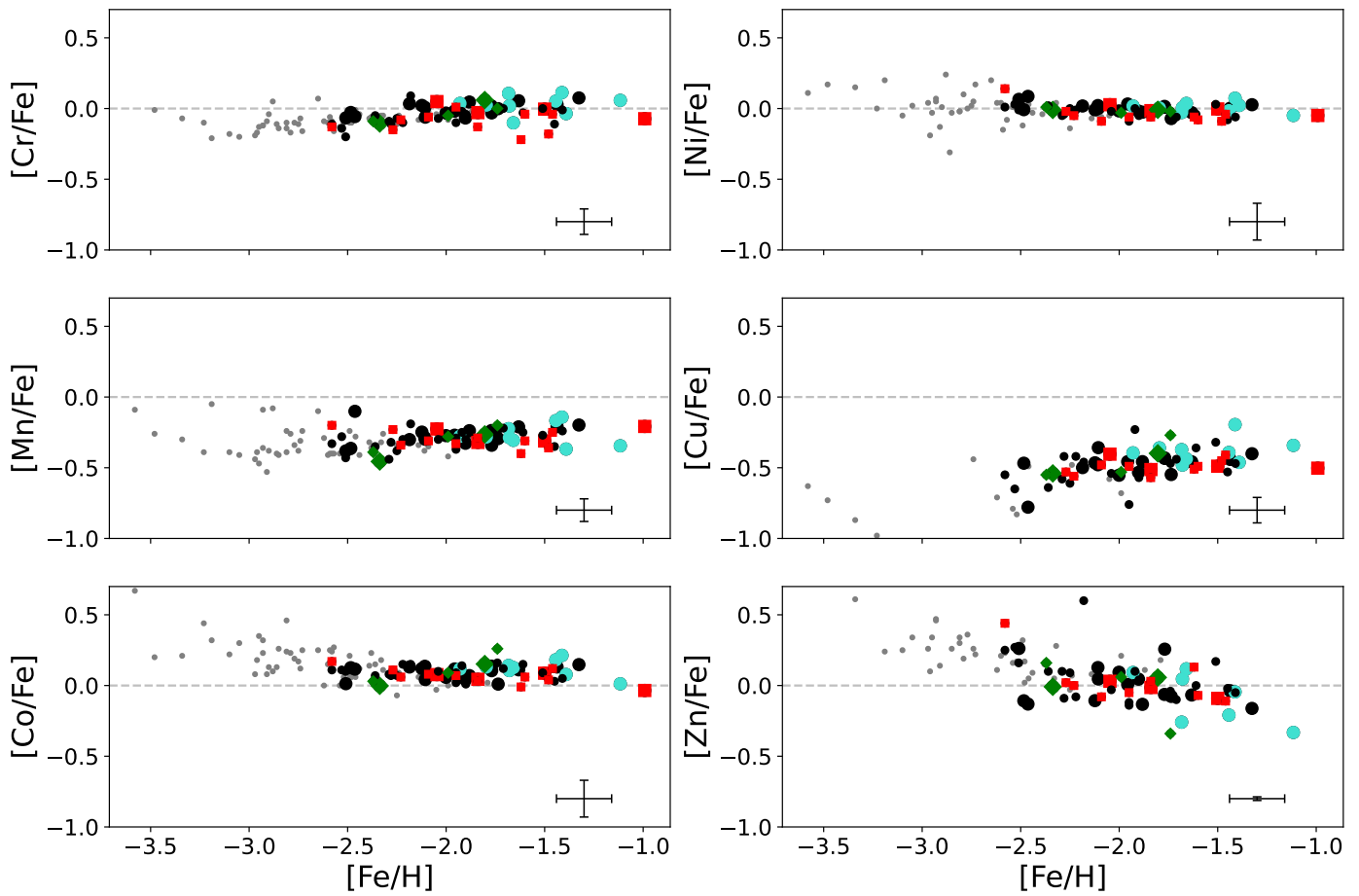


Fig. 11: Iron-peak elements abundances measured in the MINCE stars, the MINCE I sample (Cescutti et al. 2022) is identified by smaller symbols. Colors and symbols are the same as in Figure 8.

The chemical evolution model presented in Figures A.1 -A.2 is the same as described in Cescutti & Chiappini (2014). The model describes the evolution of the Galactic halo and assumes a stochastic formation of stars, it consists of 100 realizations, each of them with the same parameters of chemical evolution (infall, outflow, star formation efficiency, initial mass function, etc). In each region, the following gas infall law with a primordial chemical composition was applied:

$$\frac{dGas_{in}(t)}{dt} \propto e^{-(t-t_o)^2/\sigma_o^2}, \quad (1)$$

where t_o is set to 100 Myr and σ_o is 50 Myr. Similarly, the star formation rate is defined as

$$SFR(t) \propto (\rho_{gas}(t))^{1.5}, \quad (2)$$

where $\rho_{gas}(t)$ represents the gas mass density within the volume under consideration. Additionally, the model includes an outflow from the system:

$$\frac{dGas_{wind}(t)}{dt} \propto SFR(t). \quad (3)$$

In each volume, at each time step, the masses of the stars are assigned with a random function, weighted according to the same initial mass function. In this way in each region, at each time step, the mass of gas turned into stars is the same, but the

total number and mass distribution of the stars are different. This produces different chemical abundances, stronger if there are large differences among the yields of the stellar masses (Cescutti 2008). The other stochastic events are the enrichment by magneto-rotational driven supernovae (Nishimura et al. 2015), which are the events producing n-capture elements through the r -process in our model. Similar results can be obtained also assuming neutron star mergers with very short time delay (see Cescutti et al. 2015a). Therefore, some volumes may be enriched early on by an r -process event, while others are only enriched later, producing a dispersion in the traced n-capture elements. In this model, besides the enrichment due to r -process events, the n-capture elements are considered produced by rotating massive stars, assuming the yields by Frischknecht et al. (2016). The use of different yields does not alter substantially the outcome (Rizzuti et al. 2021). The other source of neutron capture elements, asymptotic giant branch stars, is also included by adopting yields from Cristallo et al. (2011). All the details can be found in Cescutti & Chiappini (2014). The nucleosynthesis for the remaining elements, namely α - and iron-peak elements, is based on François et al. (2004). They slightly altered the original yields presented in Woosley & Weaver (1995) to match, with a standard chemical evolution model, the abundances in extremely metal-poor stars measured in Cayrel et al. (2004). The only variation for these yields concerned nickel. The original results produced a $[Ni/Fe] \sim 0.3$ at $[Fe/H] = -2$, visible in François et al. (2004) as well as Cescutti et al. (2022). According to the present results,

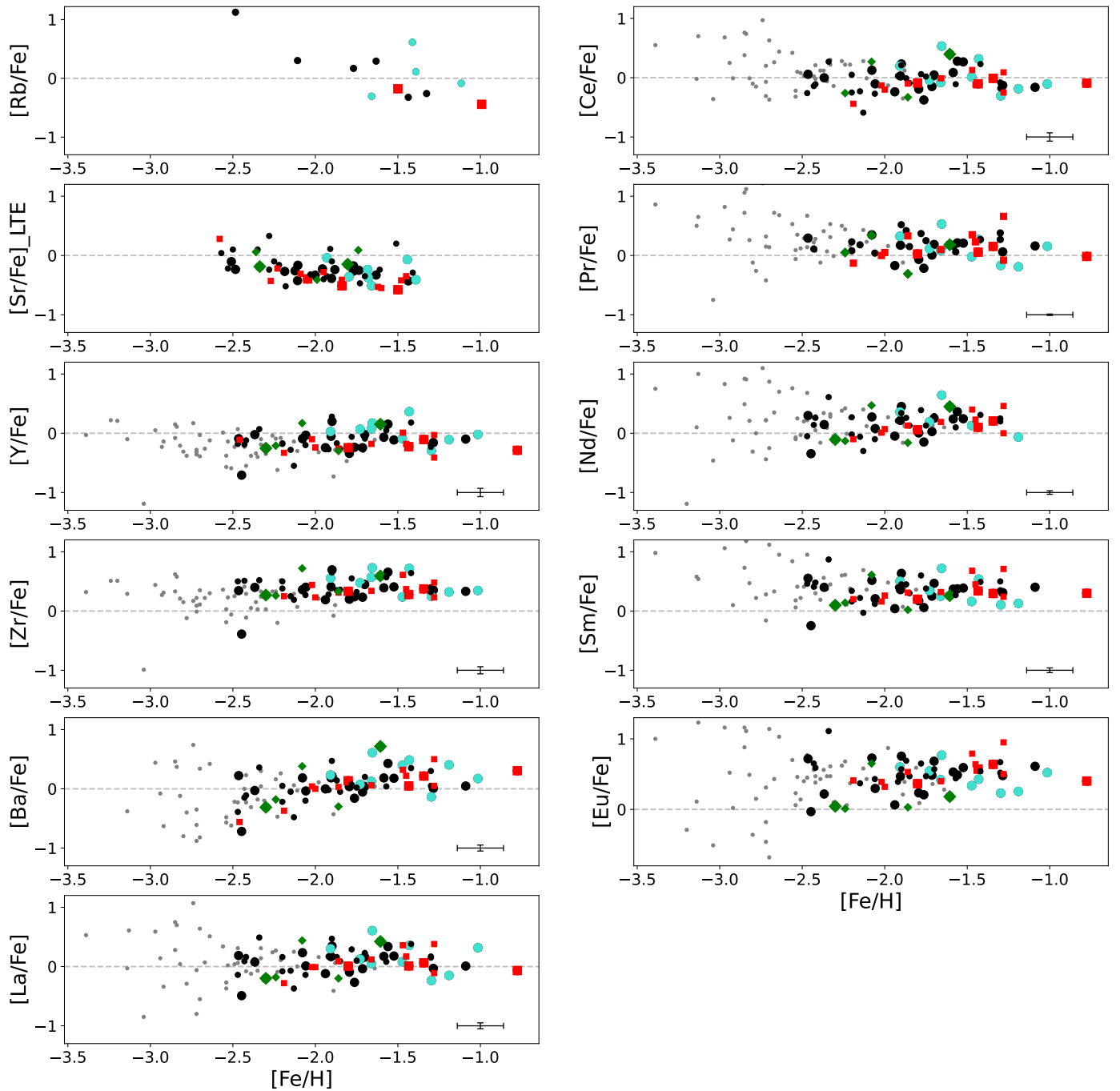


Fig. 12: Neutron capture elements abundances measured in the MINCE stars, the MINCE I sample (François et al. 2024) is identified by smaller symbols. Colors and symbols are the same as in Figure 8. The stars of the CERES survey analyzed by Lombardo et al. (2021); Lombardo (2023) are reported in gray.

nickel should be decreased by a factor of two in a new implementation of this model.

The comparison of our chemical evolution model for elements Mg to Zn of the MINCE sample (that includes also the star in the MINCE I sample), shown in Fig. A.1 and Fig. A.2, is by and large, satisfactory. Some concern is on Zn, for which the observed dispersion in abundance ratios is larger than what predicted by the model. Another cause of concern is for Co I, if a NLTE correction of the order of +0.5 dex, as suggested by Hansen et al. (2020) is applied, the [Co/Fe] ratios are all well above the model predictions. We do not provide a comparison of

the model with the data for Na I, because this element is not currently included in our model. We refrain to perform any quantitative comparison of the model with the observations, and defer such an exercise to when the sample of analysed stars will be larger.

The primary goal of MINCE is to provide abundance ratios for neutron-capture elements in intermediate metal-poor stars ($-2.5 < [\text{Fe}/\text{H}] < -1.5$), offering crucial constraints for model development to distinguish between different nucleosynthesis scenarios. In Figure A.2, we compare model predictions with the MINCE III data for neutron-capture elements (X = Rb, Sr, Y, Zn,

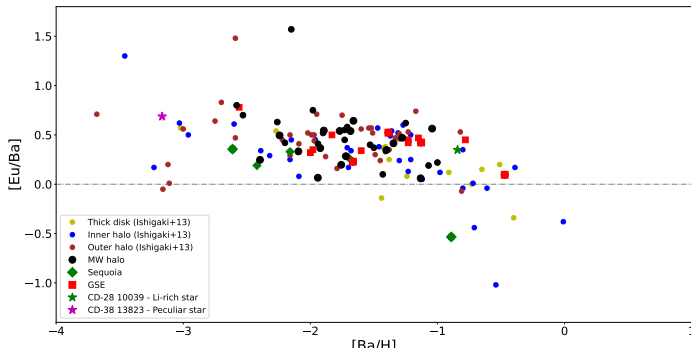


Fig. 13: Abundance ratio of [Eu/Ba] as a function of [Ba/H] for MINCE stars. MW halo, Seq and GSE stars are reported as black dots, green diamond symbols, and red square symbols, respectively. The results for MINCE I stars (François et al. 2024) are represented with same color and smaller symbols. The Li-rich star CD-28 10039 (green) and CD-38 13823 (magenta) are highlighted with star symbols. We added the samples from Ishigaki et al. (2013) for comparison.

Ba, La, Eu) presented in this study. Notably, the spread in model predictions in the [X/Fe] versus [Fe/H] space shrinks at higher metallicities, and within the metallicity range of the MINCE data, the model's predicted [X/Fe] dispersion aligns well with observations. This agreement supports the validity of the adopted nucleosynthesis prescriptions and the model assumptions. At the same time, iron peak elements and α -elements dispersion are very reduced in the abundance measurements and compatible at this metallicity with the one proposed by the model results. Moreover, this is the first time that we can confirm the model predictions for rubidium shown in Cescutti et al. (2015b), at that time there were not stellar abundances measurements for this element in halo stars. We also note that europium predictions are slightly too high compared to the measured data. This is most likely connected to the simplified assumptions for the r-process yields that scale among the elements as the observed pattern in r-process-rich stars. This offset was visible also in the original results (Cescutti & Chiappini 2014). Barium shows some stars located above the model results, but lanthanum, which has a very similar nucleosynthesis, the comparison between abundance measurements and model results is excellent. Small offsets are visible for Zr and Y too.

6. Summary and conclusions

The MINCE project investigates the nucleosynthetic processes that lead to the chemical elements production in the intermediate metallicity range, $-2.5 < [\text{Fe}/\text{H}] < -1.5$, with a particular focus on the bulk of elements heavier than iron ($Z>30$). In this work, we presented the analysis carried out of high resolution and high signal-to-noise UVES data of 94 stars. Of these we provide a detailed chemical inventory for 32 stars, while for the remaining stars we only provide [Fe/H] and atmospheric parameters. For five stars, no abundances or atmospheric parameters are provided. Remarks on individual stars can be found in Appendix C.

All 99 stars observed were kinematically characterized and divided into thin disk (42), thick disk (22), thin-to-thick disk (1) and halo (34), where 6 and 3 halo stars belong to GSE and Sequoia, respectively. Among the subsample of 32 stars with detailed chemical analysis, 23 stars belong to the Galactic halo 9 to the thick-disk, 4 to GES and 2 to Sequoia.

We derived high precision abundances for light elements (from Na to Zn) and n-capture elements (Rb, Sr, Y, Zr, Ba, La, Ce, Pr, Nd, Sm, Eu) in the 32 metal-poor stars. These results along with those in the first two papers of the MINCE serie (I -Cescutti et al. 2022, II-François et al. 2024) already represent a significant increase of n-capture elements measurements in the intermediate metallicity range. However, the low number of GSE and Sequoia candidates does not allow us to draw firm conclusions on the differences between these sub-structures and the MW halo.

Among the brightest and reddest stars, 8 of them exhibit (inverse) P-Cygni profile. We also identified one low gravity Li-rich star, CD 28-10039, with $A(\text{Li}) = 1.1$. This last belongs to the thick disk, and its Li enhancements is not due to the standard stellar evolution or non-canonical mixing processes. According to the SED of this star, the NUV excess may suggest the presence of a hot companion.

Finally, we compared our results with stochastic chemical evolution model of the MW halo. The events considered by the model for the production and the enrichment of n-capture elements are the stochastic formation of stars in the Galactic halo, magneto-rotational driven supernovae yields, rotating massive stars and asymptotic giant branch stars yields. The good agreement between the chemical abundances and the chemical evolution model proves that the nucleosynthesis processes adopted to describe the origin of the n-capture elements are reliable.

Acknowledgements. Support for the author F.L. is provided by CONICYT- 118 PFCHA/Doctorado Nacional año 2020-folio 21200677. We gratefully acknowledge support from the French National Research Agency (ANR) funded project "Pristine" (ANR-18-CE31-0017). PB acknowledges support from the ERC advanced grant N. 835087 – SPIAKID. This work has made use of data from the European Space Agency (ESA) mission *Gaia* (<https://www.cosmos.esa.int/gaia>), processed by the *Gaia* Data Processing and Analysis Consortium (DPAC, <https://www.cosmos.esa.int/web/gaia/dpac/consortium>). Funding for the DPAC has been provided by national institutions, in particular the institutions participating in the *Gaia* Multilateral Agreement. This work was also partially supported by the European Union (ChETEC-INFRA, project no. 101008324) This research has used the SIMBAD database, operated at CDS, Strasbourg, France. This publication makes use of VOSA, developed under the Spanish Virtual Observatory (<https://svo.cab.inta-csic.es>) project funded by MCIN/AEI/10.13039/501100011033/through grant PID2020-112949GB-I00. VOSA has been partially updated by using funding from the European Union's Horizon 2020 Research and Innovation Programme, under Grant Agreement n° 776403 (EXOPLANETS-A). GC acknowledges the grant PRIN project No. 2022X4TM3H 'Cosmic POT' from Ministero dell'Università e della Ricerca (MUR). A.M. acknowledges support from the project "LEGO– Reconstructing the building blocks of the Galaxy by chemical tagging" (PI: A. Muccia-relli). granted by the Italian MUR through contract PRIN 2022LLP8TK_001.

References

- Alvarez, R. & Plez, B. 1998, A&A, 330, 1109
- Arcones, A. & Thielemann, F.-K. 2023, The Astronomy and Astrophysics Review, 31, 1
- Argast, D., Samland, M., Thielemann, F.-K., & Qian, Y.-Z. 2004, A&A, 416, 997
- Bailer-Jones, C. A. L., Rybizki, J., Fouesneau, M., Demleitner, M., & Andrae, R. 2021, AJ, 161, 147
- Barbá, R. H., Minniti, D., Geisler, D., et al. 2019, ApJ, 870, L24
- Barbuy, B., Cayrel, R., Spite, M., et al. 1997, A&A, 317, L63
- Bayo, A., Rodrigo, C., Barrado Y Navascués, D., et al. 2008, A&A, 492, 277
- Beers, T. C. & Christlieb, N. 2005, ARA&A, 43, 531
- Belokurov, V., Erkal, D., Evans, N. W., Koposov, S. E., & Deason, A. J. 2018, MNRAS, 478, 611
- Bensby, T., Feltzing, S., & Oey, M. S. 2014, A&A, 562, A71
- Bergemann, M. & Gehren, T. 2008, A&A, 492, 823
- Bonifacio, P., Molaro, P., Beers, T. C., & Vladilo, G. 1998, A&A, 332, 672
- Bonifacio, P., Monaco, L., Salvadori, S., et al. 2021, A&A, 651, A79
- Bonifacio, P., Spite, M., Cayrel, R., et al. 2009, A&A, 501, 519
- Bossini, D., Vallenari, A., Bragaglia, A., et al. 2019, A&A, 623, A108

- Bovy, J. 2015, ApJS, 216, 29
- Bovy, J., Allende Prieto, C., Beers, T. C., et al. 2012, ApJ, 759, 131
- Burbidge, E. M., Burbidge, G. R., Fowler, W. A., & Hoyle, F. 1957, Rev. Mod. Phys., 29, 547
- Busso, M., Gallino, R., & Wasserburg, G. J. 1999, ARA&A, 37, 239
- Caffau, E., Bonifacio, P., François, P., et al. 2011, Nature, 477, 67
- Caffau, E., Bonifacio, P., Korotin, S. A., et al. 2021, A&A, 651, A20
- Caffau, E., Katz, D., Gómez, A., et al. 2024, A&A, 683, A72
- Caffau, E., Sbordone, L., Ludwig, H. G., Bonifacio, P., & Spite, M. 2010, Astronomische Nachrichten, 331, 725
- Carter, C., Conroy, C., Zaritsky, D., et al. 2021, ApJ, 908, 208
- Castelli, F. & Kurucz, R. L. 2003, in IAU Symposium, Vol. 210, Modelling of Stellar Atmospheres, ed. N. Piskunov, W. W. Weiss, & D. F. Gray, A20
- Cavallo, L., Cescutti, G., & Matteucci, F. 2021, MNRAS, 503, 1
- Cayrel, R., Depagne, E., Spite, M., et al. 2004, A&A, 416, 1117
- Cescutti, G. 2008, A&A, 481, 691
- Cescutti, G., Bonifacio, P., Caffau, E., et al. 2022, A&A, 668, A168
- Cescutti, G. & Chiappini, C. 2014, A&A, 565, A51
- Cescutti, G. & Kobayashi, C. 2017, A&A, 607, A23
- Cescutti, G., Romano, D., Matteucci, F., Chiappini, C., & Hirschi, R. 2015a, A&A, 577, A139
- Cescutti, G., Romano, D., Matteucci, F., Chiappini, C., & Hirschi, R. 2015b, A&A, 577, A139
- Charbonnel, C., Lagarde, N., Jasniewicz, G., et al. 2020, A&A, 633, A34
- Cohen, J. G., Christlieb, N., Qian, Y. Z., & Wasserburg, G. J. 2003, ApJ, 588, 1082
- Contursi, G., de Laverny, P., Recio-Blanco, A., & Palicio, P. A. 2021, A&A, 654, A130
- Côté, B., Eichler, M., Arcones, A., et al. 2019, ApJ, 875, 106
- Côté, B., Fryer, C. L., Belczynski, K., et al. 2018, ApJ, 855, 99
- Cowan, J. J., Sneden, C., Lawler, J. E., et al. 2021, Reviews of Modern Physics, 93, 015002
- Cristallo, S., Piersanti, L., Straniero, O., et al. 2011, ApJS, 197, 17
- Dekker, H., D'Odorico, S., Kaufer, A., Delabre, B., & Kotzlowski, H. 2000, in Society of Photo-Optical Instrumentation Engineers (SPIE) Conference Series, Vol. 4008, Optical and IR Telescope Instrumentation and Detectors, ed. M. Iye & A. F. Moorwood, 534–545
- Denissenkov, P. A., Herwig, F., Battino, U., et al. 2017, ApJ, 834, L10
- Dias, W. S., Monteiro, H., Moitinho, A., et al. 2021, MNRAS, 504, 356
- Duffau, S., Caffau, E., Sbordone, L., et al. 2017, A&A, 604, A128
- Eitner, P., Bergemann, M., Hansen, C. J., et al. 2020, A&A, 635, A38
- Ekström, S., Georgy, C., Eggenberger, P., et al. 2012, A&A, 537, A146
- Feuillet, D. K., Sahlholdt, C. L., Feltzing, S., & Casagrande, L. 2021, MNRAS, 508, 1489
- François, P., Matteucci, F., Cayrel, R., et al. 2004, A&A, 421, 613
- François, P., Cescutti, G., Bonifacio, P., et al. 2024, A&A, 686, A295
- François, P., Depagne, E., Hill, V., et al. 2007, A&A, 476, 935
- François, P., Depagne, E., Hill, V., et al. 2003, A&A, 403, 1105
- Frischknecht, U., Hirschi, R., Pignatari, M., et al. 2016, MNRAS, 456, 1803
- Gaia Collaboration, Brown, A. G. A., Vallenari, A., et al. 2021, A&A, 649, A1
- Gaia Collaboration, Vallenari, A., Brown, A. G. A., et al. 2022, arXiv e-prints, arXiv:2208.00211
- Gallino, R., Arlandini, C., Busso, M., et al. 1998, ApJ, 497, 388
- Green, G. M., Schlafly, E., Zucker, C., Speagle, J. S., & Finkbeiner, D. 2019, ApJ, 887, 93
- Hampel, M., Karakas, A. I., Stancliffe, R. J., Meyer, B. S., & Lugaro, M. 2019, ApJ, 887, 11
- Hampel, M., Stancliffe, R. J., Lugaro, M., & Meyer, B. S. 2016, ApJ, 831, 171
- Hansen, C. J., Koch, A., Mashonkina, L., et al. 2020, A&A, 643, A49
- Hansen, C. J., Montes, F., & Arcones, A. 2014, ApJ, 797, 123
- Hansen, C. J., Primas, F., Hartman, H., et al. 2012, A&A, 545, A31
- Haywood, M., Di Matteo, P., Lehnert, M. D., et al. 2018, ApJ, 863, 113
- Helmi, A., Babusiaux, C., Koppelman, H. H., et al. 2018, Nature, 563, 85
- Hill, V., Barbuy, B., Spite, M., et al. 2000, A&A, 353, 557
- Iben, Icko, J. 1967, ApJ, 147, 624
- Ishigaki, M. N., Aoki, W., & Chiba, M. 2013, ApJ, 771, 67
- Karakas, A. I. & Lattanzio, J. C. 2014, PASA, 31, e030
- Kurucz, R. L. 2005, Memorie della Societa Astronomica Italiana Supplementi, 8, 14
- Lane, J. M. M., Bovy, J., & Mackereth, J. T. 2022, MNRAS, 510, 5119
- Lind, K., Primas, F., Charbonnel, C., Grundahl, F., & Asplund, M. 2009, A&A, 503, 545
- Lindgren, L., Bastian, U., Biermann, M., et al. 2021, A&A, 649, A4
- Lodders, K., Palme, H., & Gail, H. P. 2009, Landolt Börnstein, 4B, 712
- Lombardo, L. 2023, in Memorie della Societa Astronomica Italiana, Vol. 94, 99
- Lombardo, L., Bonifacio, P., François, P., et al. 2022, A&A, 665, A10
- Lombardo, L., François, P., Bonifacio, P., et al. 2021, A&A, 656, A155
- Magrini, L., Lagarde, N., Charbonnel, C., et al. 2021, A&A, 651, A84
- Maíz Apellániz, J., Holgado, G., Pantaleoni González, M., & Caballero, J. A. 2023, A&A, 677, A137
- Mashonkina, L., Jablonka, P., Sitnova, T., Pakhomov, Y., & North, P. 2017, A&A, 608, A89
- Mashonkina, L. I., Belyaev, A. K., & Shi, J. R. 2016, Astronomy Letters, 42, 366
- Matas Pinto, A. M., Spite, M., Caffau, E., et al. 2021, A&A, 654, A170
- Meszaros, S., Dupree, A. K., & Szentgyorgyi, A. 2008, AJ, 135, 1117
- Mucciarelli, A., Bellazzini, M., & Massari, D. 2021, A&A, 653, A90
- Mucciarelli, A., Bonifacio, P., Monaco, L., Salaris, M., & Matteuzzi, M. 2024, arXiv e-prints, arXiv:2406.17026
- Mucciarelli, A., Monaco, L., Bonifacio, P., et al. 2022, A&A, 661, A153
- Mucciarelli, A., Pancino, E., Lovisi, L., Ferraro, F. R., & Lapenna, E. 2013, GALA: Stellar atmospheric parameters and chemical abundances
- Mucciarelli, A., Salaris, M., & Bonifacio, P. 2012, MNRAS, 419, 2195
- Myeong, G. C., Vasilić, E., Iorio, G., Evans, N. W., & Belokurov, V. 2019, MNRAS, 488, 1235
- Nishimura, N., Takiwaki, T., & Thielemann, F.-K. 2015, ApJ, 810, 109
- Nissen, P. E., Akerman, C., Asplund, M., et al. 2007, A&A, 469, 319
- Norris, J. E., Ryan, S. G., & Beers, T. C. 1997, ApJ, 489, L169
- Pietrinferni, A., Hidalgo, S., Cassisi, S., et al. 2021, ApJ, 908, 102
- Planck Collaboration, Adam, R., Ade, P. A. R., et al. 2016, A&A, 594, A10
- Plez, B. 2012, Turbospectrum: Code for spectral synthesis, Astrophysics Source Code Library, record ascl:1205.004
- Price-Welan, A. 2018, Adrn/Pyia: V0.2
- Remy, Q., Grenier, I. A., Marshall, D. J., & Casandjian, J. M. 2018, A&A, 616, A71
- Rizzuti, F., Cescutti, G., Matteucci, F., et al. 2021, MNRAS, 502, 2495
- Roederer, I. U., Cowan, J. J., Preston, G. W., et al. 2014, MNRAS, 445, 2970
- Sbordone, L., Caffau, E., Bonifacio, P., & Duffau, S. 2014, A&A, 564, A109
- Schönrich, R., Binney, J., & Dehnen, W. 2010, MNRAS, 403, 1829
- Seitenzahl, I. R., Cescutti, G., Röpke, F. K., Ruiter, A. J., & Pakmor, R. 2013, A&A, 559, L5
- Smith, G. H. & Dupree, A. K. 1988, AJ, 95, 1547
- Smith, V. V. & Lambert, D. L. 1984, PASP, 96, 226
- Sneden, C., Preston, G. W., McWilliam, A., & Searle, L. 1994, ApJ, 431, L27
- Spite, F. & Spite, M. 1982, A&A, 115, 357
- Thygesen, A. O., Sbordone, L., Ludwig, H. G., et al. 2016, A&A, 588, A66
- Timmes, F. X., Woosley, S. E., & Weaver, T. A. 1995, ApJS, 98, 617
- Vergely, J. L., Lallemand, R., & Cox, N. L. J. 2022, A&A, 664, A174
- Villanova, S., Monaco, L., Geisler, D., et al. 2019, ApJ, 882, 174
- Watson, D., Hansen, C. J., Selsing, J., et al. 2019, Nature, 574, 497
- Woosley, S. E. & Weaver, T. A. 1995, ApJS, 101, 181
- Yong, D., Roederer, I. U., Grundahl, F., et al. 2014, MNRAS, 441, 3396

Appendix A: Additional figures

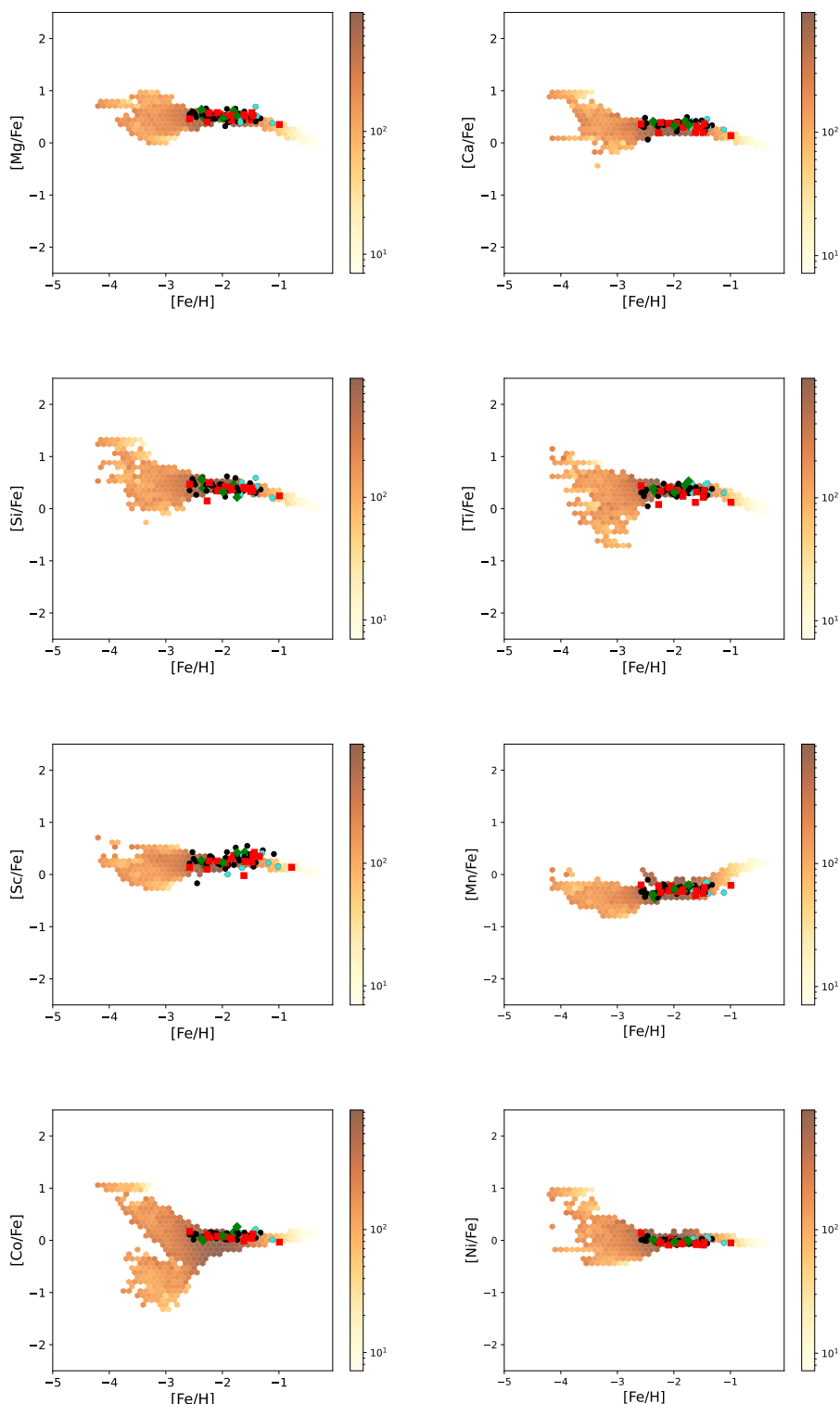


Fig. A.1: Comparison between the chemical abundances in MINCE I and III stars and the chemical evolution model for Mg, Ca, Si, Ti, Sc, Mn, Co and Ni. Colors and symbols are the same as in Figure 8

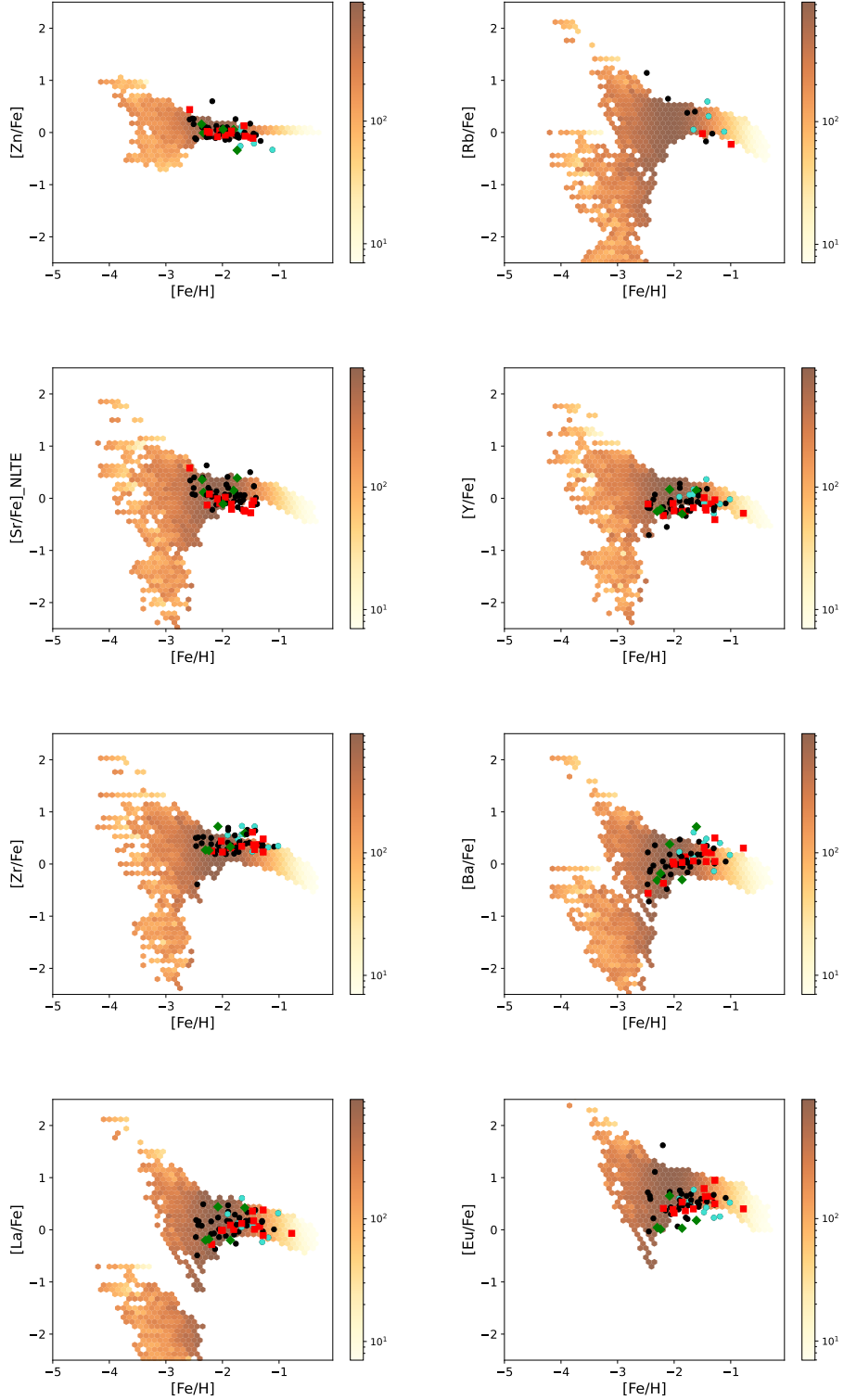


Fig. A.2: Comparison between the chemical abundances in MINCE I and III stars and the chemical evolution model for Zn, Rb, Sr, Y, Zr, Ba, La, Eu. Colors and symbols are the same as in Figure 8

Appendix B: Additional tables

Table B.1: Coordinates, *Gaia* magnitudes and radial velocities of the sample.

N	Star	RA [hh:mm:ss]	DEC [° :′ : ″]	G [mag]	$G_{\text{BP}} - G_{\text{RP}}$ [mag]	RV km s ⁻¹	σ_{RV} km s ⁻¹
1	BD-11 3235	12:05:09.45	-12:04:53.1	9.41	1.54	118.66	0.24
2	BD-12 5650	20:07:39.97	-11:44:04.6	9.03	1.47	-7.89	0.15
3	BD-13 934	04:37:15.68	-13:38:48.1	9.05	1.48	80.89	0.19
4	BD-13 3195	10:41:59.98	-14:41:14.4	9.03	1.4	129.82	0.16
5	BD-13 3488	12:06:16.06	-14:33:42.6	9.02	1.68	72.06	0.13
6	BD-13 6352	23:09:38.58	-12:17:27.4	9.63	1.78	6.15	0.37
7	BD-14 52	00:22:00.67	-13:59:08.9	9.66	1.56	59.75	0.24
8	BD-15 4109	15:27:20.71	-16:17:57.8	9.22	1.65	-30.24	0.22
9	BD-15 5449	19:44:42.15	-15:31:01.1	9.35	1.51	125.96	0.37
10	BD-16 2232	07:59:46.83	-17:23:08.4	9.44	1.38	510.25	0.29
11	BD-17 3143	10:25:45.93	-17:59:20.5	9.8	1.45	44.59	0.33
12	BD-17 4251	15:06:44.19	-17:37:39.6	9.16	1.71	352.18	0.41
13	BD-18 5150	18:58:39.07	-18:46:52.4	8.49	1.54	25.84	0.13
14	BD-19 6363	22:55:38.46	-18:45:54.0	9.71	1.13	37.6	3.29
15	CD-23 1855	04:18:21.57	-23:23:39.1	9.63	1.27	53.83	0.17
16	CD-23 11064	13:25:48.58	-23:59:13.0	9.36	1.97	-47.95	0.21
17	CD-24 613	01:26:26.97	-24:21:03.3	9.62	1.96	-4.02	2.16
18	CD-24 1384	03:02:13.68	-23:48:37.4	9.23	1.67	179.45	0.13
19	CD-26 7083	09:27:48.16	-26:48:30.9	8.82	1.29	105.36	0.13
20	CD-27 14182	19:40:22.01	-27:37:48.4	9.21	1.71	-4.85	0.24
21	CD-27 15535	21:37:36.08	-26:56:48.0	9.28	1.79	40.97	0.13
22	CD-27 16505	23:59:31.55	-27:16:52.6	9.18	1.57	-98.43	0.3
23	CD-28 10039	13:22:48.61	-29:13:12.2	9.09	1.54	60.7	0.17
24	CD-28 10387	14:01:50.71	-29:28:30.1	9.71	1.05	-43.3 ^(a)	1.77
25	CD-28 16762	20:34:20.77	-28:32:33.3	9.55	1.42	-90.89	0.16
26	CD-28 17446	21:46:45.62	-27:46:43.4	9.44	1.6	96.97	0.34
27	CD-29 9391	11:52:09.82	-30:16:19.7	9.43	1.94	-0.18	0.97
28	CD-29 15930	19:17:19.19	-29:28:02.9	9.38	1.57	-10.5 ^(a)	0.45
29	CD-31 16658	19:24:40.24	-31:03:08.6	9.28	1.87	18.51 ^(a)	0.18
30	CD-31 16922	19:39:27.38	-31:20:59.4	8.95	1.57	19.69 ^(a)	9.08
31	CD-31 17277	20:04:18.55	-31:17:17.4	9.18	1.72	111.21	0.51
32	CD-32 4154	07:34:02.70	-32:37:53.2	9.23	1.73	56.74	0.14
33	CD-32 13158	17:41:14.77	-32:08:03.2	6.91	1.03	-15.71	0.13
34	CD-32 14894	19:08:54.80	-32:25:49.6	9.31	1.82	93.59	0.24
35	CD-33 2721	06:05:11.04	-33:08:47.2	8.89	1.43	219.28	0.25
36	CD-33 15063	20:37:09.52	-33:30:29.8	9.51	1.52	-83.15	0.27
37	CD-34 242	00:42:17.06	-33:23:34.3	9.41	1.88	11.86	1.41
38	CD-34 3626	07:28:22.20	-34:16:43.9	8.62	1.37	39.16	0.13
39	CD-34 5597	09:07:05.26	-34:36:22.8	8.98	1.41	45.47	0.14
40	CD-35 4882	08:38:16.96	-36:16:12.3	8.95	1.53	58.45	0.14
41	CD-35 13334	19:15:27.67	-34:54:44.0	9.44	1.91	-84.73	0.29
42	CD-35 13661	19:44:11.70	-35:26:28.2	9.55	1.37	59.37	0.26
43	CD-35 14807	21:29:53.08	-35:10:08.6	9.73	1.53	14.21	0.18
44	CD-36 518	01:21:26.75	-35:41:02.3	9.45	1.33	154.19	0.16
45	CD-36 11584	17:31:01.16	-36:45:38.0	7.57	1.06	-15.71 ^(b)	
46	CD-38 13823	20:03:11.21	-38:27:01.0	9.85	1.33	-218.19	0.28
47	CD-39 6037	10:00:24.45	-39:59:00.1	9.08	1.54	203.46	0.22
48	CD-39 9313	14:53:41.90	-40:29:56.2	9.29	1.41	136.67	0.44
49	CD-40 471	01:52:29.17	-39:39:54.5	9.19	1.5	81.68	0.36
50	CD-41 4744	09:02:29.24	-42:25:06.9	8.84	1.48	19.46	0.18
51	CD-41 7816	13:25:56.60	-41:40:29.2	8.89	1.48	18.38	0.14
52	CD-41 14843	22:20:13.37	-41:02:47.4	9.3	1.67	-8.63	0.15
53	CD-43 7161	11:35:54.19	-43:41:57.8	9.24	1.51	189.2	0.26
54	CD-43 8736	14:01:43.85	-43:56:33.8	9.31	1.79	-2.15	0.33
55	CD-44 12644	18:29:45.64	-44:24:28.2	9.08	1.27	34.60 ^(a)	0.16
56	CD-44 13783	20:11:49.99	-44:07:42.6	9.33	1.87	92.29	0.25

Continue on the next page

TableB.1–continued.

N	Star	RA [hh:mm:ss]	DEC [° :′ :″]	G [mag]	$G_{\text{BP}} - G_{\text{RP}}$ [mag]	RV [km s ⁻¹]	σ_{RV} [km s ⁻¹]
57	CD-44 13981	20:29:41.18	-43:47:02.7	9.23	1.75	-22.36	0.18
58	CD-44 15269	23:31:56.96	-44:12:43.4	9.9	1.42	25.83	0.23
59	CD-46 8357	13:03:11.95	-46:52:51.5	9.07	1.41	-32.39	5.24
60	CD-46 13658	20:41:33.09	-45:45:25.0	9.53	1.78	-39.74 ^(b)	
61	CD-47 14271	22:38:03.11	-46:32:32.0	9.57	1.88	-36.33	0.28
62	CD-48 12928	19:09:18.11	-48:35:45.5	8.85	2.08	7.46	0.35
63	CD-50 823	02:47:57.63	-49:41:36.7	8.86	1.54	44.46	0.23
64	CD-50 877	02:57:28.07	-49:31:26.2	8.73	1.98	109.99	0.61
65	CD-52 976	04:41:20.20	-51:54:47.5	9.35	1.21	193.02	0.16
66	CD-52 2441	08:34:39.47	-52:36:37.8	8.67	1.33	16.85 ^(b)	
67	CD-52 4849	12:08:03.89	-52:58:26.7	9.21	1.56	150.76	0.34
68	CD-57 1959	08:01:58.97	-57:52:03.2	9.42	1.41	140.32	0.14
69	CD-58 294	01:24:37.75	-57:33:46.9	9.61	2.01	104.44	0.25
70	CD-59 6913	18:36:34.19	-59:42:35.5	9.14	1.66	31.47	0.33
71	CD-62 15	00:24:26.77	-61:41:39.8	9.39	1.25	95.52	0.18
72	CPD-62 1126	08:54:42.79	-62:49:48.0	8.78	1.45	-4.04	0.15
73	HD 6518	01:05:49.23	-26:39:45.2	8.92	1.39	128.24	0.17
74	HD 19367	03:06:25.12	-15:00:12.9	9.22	1.45	141.72	0.29
75	HD 41020	06:00:37.04	-40:22:06.0	8.61	1.69	164.25	0.49
76	HD 114621	13:12:56.14	-63:56:09.6	8.35	1.43	1.22	0.14
77	HD 298008	10:23:46.94	-50:01:54.2	8.83	1.52	7.2	0.51
78	HD 298296	09:11:01.43	-52:25:17.1	8.69	1.4	26.64	0.13
79	TYC 5340-1656-1	05:29:17.35	-11:40:37.6	9.62	1.42	46.67 ^(b)	
80	TYC 5422-1192-1	07:41:52.22	-13:36:53.5	9.43	0.48	60.24 ^(b)	
81	TYC 5763-1084-1	20:35:42.25	-12:35:36.5	9.82	1.91	-54.96	0.24
82	TYC 6002-1724-1	08:24:38.17	-17:55:23.6	9.75	1.29	207.81	0.2
83	TYC 6108-150-1	12:20:06.99	-22:14:35.3	9.82	1.21	109.24	2.59
84	TYC 6195-815-1	15:56:04.95	-19:59:52.7	9.58	1.76	13.01	0.28
85	TYC 6199-351-1	15:58:13.62	-21:56:52.4	9.19	1.52	78.89	0.19
86	TYC 6310-1651-2	19:28:39.93	-20:48:30.6	9.53	1.91	27.56	0.21
87	TYC 7144-1122-1	08:36:40.01	-34:15:50.7	9.28	1.81	22.53	0.13
88	TYC 7351-734-1	16:13:05.07	-34:23:59.3	8.99	1.74	-46.3	0.13
89	TYC 7354-1196-1	16:46:09.99	-34:08:43.1	8.82	1.31	4.47	0.21
90	TYC 7427-35-1	19:17:11.88	-32:32:42.5	8.91	1.63	-37.15	0.14
91	TYC 8025-237-1	00:01:55.06	-48:45:17.1	9.51	1.75	60.1	0.23
92	TYC 8161-753-1	08:23:43.70	-50:58:23.4	8.84	1.42	209.7	0.18
93	TYC 8178-334-1	09:12:04.35	-52:08:22.1	8.87	1.5	16.59 ^(b)	
94	TYC 8263-2160-1	13:58:20.15	-45:46:43.0	9.01	1.43	10.51	0.19
95	TYC 8325-6844-1	16:31:24.40	-46:32:20.0	9.21	1.58	-65.07	0.46
96	TYC 8394-14-1	19:48:11.54	-48:35:11.9	9.29	1.67	1.92	0.45
97	TYC 8400-1610-1	20:04:23.01	-49:06:31.6	9.56	1.97	7.83	0.25
98	TYC 8584-127-1	09:23:52.76	-53:58:53.1	8.66	1.51	21.96	0.23
99	TYC 8633-2281-1	12:13:36.87	-53:13:12.9	8.67	1.61	302.75	0.25

Note. ^(a)RV corrected by our findings (see subsection 2.1).

Note. ^(b)RV derived by the UVES spectrum (see subsection 2.1).

Table B.2: Reddening, atmospheric parameters and metallicity of the sample.

N	Star	Av	T_{eff} [K]	$\log g$ [gcs]	ξ [km s $^{-1}$]	[Fe/H]	Comments
1	BD-11 3235	0.18	4158	0.90	1.93	-2.11 ± 0.14	
2	BD-12 5650	0.44	4200	1.49	1.50	-0.13 ± 0.19	
3	BD-13 934	0.66	4245	0.91	1.97	-1.93 ± 0.12	-
4	BD-13 3195	0.17	4280	1.15	1.81	-1.41 ± 0.15	-
5	BD-13 3488	0.21	4000	1.36	1.50	-0.39 ± 0.20	
6	BD-13 6352	0.09	3928	0.61	1.90	-1.28 ± 0.07	
7	BD-14 52	0.06	4108	0.75	1.94	-1.70 ± 0.17	<i>Gaia SB1</i>
8	BD-15 4109	0.34	4048	0.53	2.04	-2.01 ± 0.15	
9	BD-15 5449	0.58	4230	0.80	2.01	-2.19 ± 0.12	
10	BD-16 2232	0.09	4367	0.98	1.96	-1.77 ± 0.12	
11	BD-17 3143	0.24	4344	0.48	2.19	-1.68 ± 0.14	
12	BD-17 4251	0.30	4000	0.53	1.97	-1.47 ± 0.20	
13	BD-18 5150	0.57	4080	1.06	1.66	-0.27 ± 0.16	
14	BD-19 6363	0.09	4767	1.82	1.82	-2.51 ± 0.12	
15	CD-23 1855	0.14	4551	1.23	1.96	-1.96 ± 0.11	
16	CD-23 11064	0.28	3748	0.82	1.73	-0.83 ± 0.19	
17	CD-24 613	0.04	3758	0.81	1.82	-0.54 ± 0.16	
18	CD-24 1384	0.06	4000	1.05	1.67	-0.70 ± 0.16	
19	CD-26 7083	0.41	4579	0.53	2.23	-0.43 ± 0.08	
20	CD-27 14182	0.50	4000	1.11	1.63	-0.28 ± 0.20	
21	CD-27 15535	0.08	3935	1.13	1.59	-0.41 ± 0.12	
22	CD-27 16505	0.05	4046	0.80	1.85	-1.33 ± 0.16	
23	CD-28 10039	0.22	4100	0.71	1.91	-1.12 ± 0.20	
24	CD-28 10387	0.16	5043	2.25	1.58	-0.28 ± 0.17	
25	CD-28 16762	0.17	4291	0.96	1.93	-1.63 ± 0.13	
26	CD-28 17446	0.07	4063	0.75	1.93	-1.84 ± 0.17	
27	CD-29 9391	0.17	3780	0.71	1.75	-0.46 ± 0.13	
28	CD-29 15930	0.40	4105	0.72	1.96	-1.79 ± 0.11	
29	CD-31 16658	0.26	3844	0.70	1.81	-0.84 ± 0.16	
30	CD-31 16922	0.31					fast rotator
31	CD-31 17277	0.68	4000	0.74	1.84	-0.97 ± 0.11	LPV
32	CD-32 4154	0.27	3993	0.97	1.69	-0.62 ± 0.10	
33	CD-32 13158	3.06	5129	1.65	1.87	0.10 ± 0.15	
34	CD-32 14894	0.35	3892	0.53	1.92	-1.05 ± 0.10	
35	CD-33 2721	0.16	4343	0.78	2.06	-1.89 ± 0.18	
36	CD-33 15063	0.12	4140	0.90	1.89	-1.80 ± 0.16	
37	CD-34 242	0.04	3843	0.88	1.67	-0.33 ± 0.09	
38	CD-34 3626	0.36	4396	0.81	1.90	-0.01 ± 0.17	
39	CD-34 5597	0.66	4277	1.21	1.71	-0.56 ± 0.15	
40	CD-35 4882	0.30	4101	1.37	1.54	-0.41 ± 0.16	
41	CD-35 13334	0.24	3800	0.78	1.76	-0.74 ± 0.11	
42	CD-35 13661	0.60	4442	0.89	2.08	-2.29 ± 0.15	<i>Gaia SB1</i>
43	CD-35 14807	0.12	4083	1.24	1.62	-0.75 ± 0.16	
44	CD-36 518	0.07	4424	1.24	1.86	-1.74 ± 0.11	
45	CD-36 11584	2.64	5059	0.88	2.20	0.10 ± 0.15	fast rotator
46	CD-38 13823	0.22	4515	0.85	2.15	-2.46 ± 0.14	
47	CD-39 6037	0.23	4082	0.92	1.79	-0.99 ± 0.16	
48	CD-39 9313	0.43	4323	1.03	1.93	-1.68 ± 0.15	
49	CD-40 471	0.05	4323	0.63	2.17	-2.48 ± 0.14	
50	CD-41 4744	0.33	4168	1.41	1.55	-0.31 ± 0.16	
51	CD-41 7816	0.16	4199	1.80	1.35	-0.07 ± 0.17	
52	CD-41 14843	0.03	4000	1.13	1.63	-0.59 ± 0.19	
53	CD-43 7161	0.30	4167	0.82	1.93	-1.50 ± 0.13	
54	CD-43 8736	0.28	3919	0.67	1.87	-1.21 ± 0.09	
55	CD-44 12644	0.28	4564	1.15	2.00	-1.44 ± 0.12	
56	CD-44 13783	0.14	3848	0.86	1.73	-0.76 ± 0.15	

Continue on the next page

TableB.2–continued.

N	Star	A _V	T _{eff} [K]	log g [gcs]	ξ [km s ⁻¹]	[Fe/H]	Comments
57	CD-44 13981	0.12	3970	0.96	1.71	-0.71 ± 0.14	
58	CD-44 15269	0.05	4265	1.00	1.87	-1.39 ± 0.15	
59	CD-46 8357	0.18					RS CVn
60	CD-46 13658	0.09	3936	0.94	1.70	-0.68 ± 0.14	
61	CD-47 14271	0.04	3827	0.76	1.81	-0.93 ± 0.20	
62	CD-48 12928	0.24	3642	0.64	1.80	-0.90 ± 0.20	LPV
63	CD-50 823	0.11	4141	0.70	1.97	-1.64 ± 0.18	<i>Gaia</i> SB1
64	CD-50 877	0.08	3733	0.55	1.86	-0.91 ± 0.12	LPV
65	CD-52 976	0.06	4655	1.29	1.97	-1.90 ± 0.09	
66	CD-52 2441	1.24					SB2
67	CD-52 4849	0.52	4233	0.53	2.05	-2.36 ± 0.17	<i>Gaia</i> SB1
68	CD-57 1959	0.50	4342	1.09	1.93	-2.00 ± 0.12	
69	CD-58 294	0.07	3707	0.62	1.81	-0.81 ± 0.12	LPV
70	CD-59 6913	0.22	4044	0.52	2.04	-2.03 ± 0.17	
71	CD-62 15	0.05	4584	1.26	1.97	-2.11 ± 0.12	
72	CPD-62 1126	0.34	4224	1.26	1.64	-0.49 ± 0.15	
73	HD 6518	0.06	4285	1.15	1.81	-1.44 ± 0.14	
74	HD 19367	0.13	4345	0.74	2.10	-2.12 ± 0.14	
75	HD 41020	0.23	4000	0.76	1.80	-1.10 ± 0.19	LPV
76	HD 114621	0.80	4260	0.98	1.80	-0.33 ± 0.15	
77	HD 298008	0.21	4141	1.48	1.48	-0.07 ± 0.18	
78	HD 298296	0.61	4311	1.00	1.80	-0.35 ± 0.15	
79	TYC 5340-1656-1	0.28					RS CVn (?), SB2
80	TYC 5422-1192-1	0.54					member of OC NGC 2423, fast rotator
81	TYC 5763-1084-1	0.18	3801	0.75	0.77	-0.87 ± 0.12	
82	TYC 6002-1724-1	0.27	4551	1.12	2.05	-2.34 ± 0.12	
83	TYC 6108-150-1	0.20	4617	1.52	1.84	-1.94 ± 0.12	<i>Gaia</i> SB1
84	TYC 6195-815-1	0.60	3947	0.48	1.99	-1.49 ± 0.09	LPV
85	TYC 6199-351-1	0.71	4111	0.99	1.82	-1.66 ± 0.16	
86	TYC 6310-1651-2	0.30	3809	0.67	1.80	-0.67 ± 0.12	
87	TYC 7144-1122-1	0.44	3912	0.93	1.69	-0.45 ± 0.12	
88	TYC 7351-734-1	0.76	3996	1.07	1.59	-0.09 ± 0.16	
89	TYC 7354-1196-1	1.03	4456	1.73	1.55	-0.41 ± 0.15	
90	TYC 7427-35-1	0.26	4000	1.21	1.50	-0.23 ± 0.19	
91	TYC 8025-237-1	0.05	3958	0.74	1.85	-1.09 ± 0.11	
92	TYC 8161-753-1	0.88	4266	1.25	1.80	-1.77 ± 0.13	
93	TYC 8178-334-1	0.68	4160	1.10	1.66	-0.10 ± 0.18	
94	TYC 8263-2160-1	0.31	4278	0.69	1.94	-0.27 ± 0.14	
95	TYC 8325-6844-1	0.52	4060	1.88	1.24	0.03 ± 0.17	
96	TYC 8394-14-1	0.16	4000	0.53	1.97	-1.49 ± 0.19	LPV fast rotator
97	TYC 8400-1610-1	0.13	3748	0.78	1.78	-0.88 ± 0.14	
98	TYC 8584-127-1	1.08	4144	0.95	1.76	-0.58 ± 0.09	300 Myr, 3.2M \odot
99	TYC 8633-2281-1	0.28	4118	0.58	2.06	-2.05 ± 0.19	

Table B.3: Targets' velocity components in galactocentric cylindrical coordinates (V_R, V_T, V_Z), apocentric and pericentric distances (r_{ap}, r_{peri}), orbital eccentricities (ecc.) and maximum height over the galactic plane (Z_{max}).

Star	V_R [kms $^{-1}$]	V_T [kms $^{-1}$]	V_Z [kms $^{-1}$]	r_{ap} [kpc]	r_{peri} [kpc]	ecc.	Z_{max} [kpc]
BD-11 3235	45.62 ± 5.25	10.01 ± 6.00	-15.69 ± 5.37	8.13 ± 0.05	0.19 ± 0.11	0.95 ± 0.02	2.30 ± 0.26
BD-12 5650	-7.89 ± 0.55	206.02 ± 3.01	12.21 ± 0.44	7.36 ± 0.10	6.29 ± 0.25	0.08 ± 0.01	0.36 ± 0.04
BD-13 934	58.93 ± 0.81	69.00 ± 4.03	77.91 ± 3.70	9.87 ± 0.07	2.07 ± 0.06	0.65 ± 0.01	4.70 ± 0.43
BD-13 3195	-135.34 ± 3.32	52.63 ± 2.42	29.82 ± 1.48	10.11 ± 0.11	1.04 ± 0.06	0.81 ± 0.01	1.69 ± 0.01
BD-13 3488	-6.05 ± 0.31	181.66 ± 0.11	65.61 ± 0.14	7.90 ± 0.00	5.96 ± 0.01	0.14 ± 0.00	1.78 ± 0.01
BD-13 6352	24.03 ± 0.59	59.32 ± 9.21	-85.12 ± 4.50	8.12 ± 0.06	1.58 ± 0.21	0.67 ± 0.04	4.32 ± 0.40
BD-14 52	18.29 ± 0.94	110.20 ± 7.04	-86.08 ± 1.82	8.77 ± 0.07	3.53 ± 0.21	0.43 ± 0.03	4.35 ± 0.25
BD-15 4109	-15.38 ± 0.61	11.33 ± 10.40	-123.45 ± 5.18	6.45 ± 0.02	0.22 ± 0.17	0.93 ± 0.05	4.53 ± 0.28
BD-15 5449	-251.76 ± 10.15	52.63 ± 11.01	-0.66 ± 1.92	12.05 ± 0.40	0.69 ± 0.17	0.89 ± 0.03	1.72 ± 0.19
BD-16 2232	382.80 ± 2.41	-66.67 ± 3.28	72.18 ± 0.17	74.56 ± 2.40	1.07 ± 0.06	0.97 ± 0.00	12.82 ± 0.48
BD-17 3143	-171.95 ± 6.88	51.97 ± 10.86	-69.62 ± 6.05	14.00 ± 0.67	1.15 ± 0.25	0.85 ± 0.04	3.81 ± 0.50
BD-17 4251	-334.14 ± 1.73	4.35 ± 8.05	98.02 ± 5.58	26.33 ± 0.31	0.07 ± 0.09	0.99 ± 0.01	19.43 ± 0.37
BD-18 5150	-26.08 ± 0.29	239.84 ± 0.08	4.24 ± 0.10	8.70 ± 0.04	6.80 ± 0.02	0.12 ± 0.00	0.19 ± 0.00
BD-19 6363	-129.71 ± 9.04	23.59 ± 15.71	-70.36 ± 4.32	9.18 ± 0.24	0.51 ± 0.30	0.89 ± 0.06	4.85 ± 0.76
CD-23 1855	-112.81 ± 2.79	2.36 ± 5.40	-2.71 ± 0.69	10.55 ± 0.11	0.04 ± 0.07	0.99 ± 0.01	1.61 ± 0.05
CD-23 11064	25.52 ± 0.33	258.65 ± 0.21	10.42 ± 1.39	11.21 ± 0.02	7.12 ± 0.03	0.22 ± 0.00	1.56 ± 0.08
CD-24 613	34.28 ± 2.30	191.39 ± 2.00	19.72 ± 2.11	8.90 ± 0.06	6.74 ± 0.09	0.14 ± 0.01	2.13 ± 0.12
CD-24 1384	85.81 ± 0.62	53.46 ± 2.72	-94.33 ± 1.16	9.89 ± 0.02	1.37 ± 0.08	0.76 ± 0.01	4.62 ± 0.04
CD-26 7083	116.95 ± 4.27	209.54 ± 5.32	1.45 ± 1.79	14.54 ± 0.89	6.33 ± 0.17	0.39 ± 0.01	1.48 ± 0.18
CD-27 14182	7.99 ± 0.62	244.62 ± 0.48	2.27 ± 0.29	8.66 ± 0.01	6.85 ± 0.04	0.12 ± 0.00	0.56 ± 0.02
CD-27 15535	-43.93 ± 0.20	179.78 ± 1.32	-32.34 ± 0.25	7.68 ± 0.02	4.94 ± 0.06	0.22 ± 0.00	1.25 ± 0.02
CD-27 16505	-377.06 ± 15.13	3.92 ± 8.09	148.23 ± 1.76	73.99 ± 20.61	0.05 ± 0.08	1.00 ± 0.00	26.32 ± 6.05
CD-28 10039	-40.01 ± 0.21	179.67 ± 0.49	69.56 ± 1.19	7.37 ± 0.04	5.35 ± 0.01	0.16 ± 0.00	2.27 ± 0.07
CD-28 10387	90.87 ± 4.12	200.78 ± 3.19	14.26 ± 2.18	9.73 ± 0.08	5.10 ± 0.16	0.31 ± 0.02	0.60 ± 0.04
CD-28 16762	80.54 ± 0.26	27.25 ± 5.90	-36.10 ± 3.00	6.96 ± 0.04	0.44 ± 0.10	0.88 ± 0.03	1.38 ± 0.07
CD-28 17446	-369.09 ± 17.82	-29.91 ± 12.95	69.11 ± 7.29	40.38 ± 11.89	0.38 ± 0.16	0.98 ± 0.00	13.60 ± 5.56
CD-29 9391	-17.33 ± 0.22	189.58 ± 1.71	-44.15 ± 2.03	7.92 ± 0.01	6.00 ± 0.08	0.14 ± 0.01	1.49 ± 0.07
CD-29 15930	7.78 ± 0.64	148.89 ± 3.26	-38.60 ± 1.90	5.75 ± 0.08	3.01 ± 0.12	0.31 ± 0.01	0.97 ± 0.04
CD-31 16658	-6.67 ± 0.62	185.77 ± 1.35	-54.51 ± 1.52	6.26 ± 0.05	4.72 ± 0.07	0.14 ± 0.00	1.15 ± 0.03
CD-31 16922	-34.03 ± 8.31	218.84 ± 1.40	0.71 ± 3.65	8.05 ± 0.29	6.40 ± 0.11	0.11 ± 0.03	0.35 ± 0.02
CD-31 17277	-138.60 ± 1.60	14.28 ± 8.60	-66.96 ± 0.86	7.89 ± 0.04	0.23 ± 0.13	0.94 ± 0.03	2.81 ± 0.09
CD-32 4154	36.70 ± 0.73	213.91 ± 1.22	3.94 ± 0.18	9.74 ± 0.11	7.55 ± 0.06	0.13 ± 0.00	0.17 ± 0.01
CD-32 13158	2.91 ± 0.15	221.09 ± 0.39	2.63 ± 0.18	6.71 ± 0.04	6.51 ± 0.06	0.01 ± 0.00	0.03 ± 0.00
CD-32 14894	-109.30 ± 0.33	281.31 ± 2.63	48.37 ± 4.18	13.56 ± 0.07	4.96 ± 0.10	0.46 ± 0.01	1.87 ± 0.18
CD-33 2721	15.36 ± 1.76	36.47 ± 0.90	-111.53 ± 0.82	9.37 ± 0.03	1.07 ± 0.01	0.79 ± 0.00	6.60 ± 0.16
CD-33 15063	49.34 ± 0.95	-76.52 ± 12.58	-9.60 ± 2.83	6.47 ± 0.06	1.38 ± 0.27	0.65 ± 0.06	1.38 ± 0.06
CD-34 242	62.55 ± 2.67	217.59 ± 0.46	-10.11 ± 1.43	10.43 ± 0.12	6.70 ± 0.05	0.22 ± 0.01	2.09 ± 0.10
CD-34 3626	-53.55 ± 1.13	179.27 ± 0.54	7.90 ± 0.16	9.63 ± 0.05	5.62 ± 0.02	0.26 ± 0.00	0.28 ± 0.01
CD-34 5597	14.31 ± 0.33	195.38 ± 0.26	-21.56 ± 0.68	8.41 ± 0.01	6.55 ± 0.02	0.12 ± 0.00	0.43 ± 0.02
CD-35 4882	36.00 ± 0.39	191.43 ± 0.28	-18.75 ± 0.35	8.68 ± 0.02	6.01 ± 0.01	0.18 ± 0.00	0.31 ± 0.01
CD-35 13334	76.62 ± 0.40	209.65 ± 0.61	19.43 ± 0.59	7.88 ± 0.08	4.77 ± 0.06	0.25 ± 0.00	0.86 ± 0.02
CD-35 13661	-157.80 ± 5.49	-66.73 ± 15.57	121.72 ± 7.38	8.66 ± 0.35	1.10 ± 0.27	0.77 ± 0.04	3.58 ± 0.29
CD-35 14807	-26.36 ± 1.21	227.47 ± 1.23	6.35 ± 1.20	8.26 ± 0.10	6.68 ± 0.09	0.11 ± 0.00	1.29 ± 0.13
CD-36 518	142.02 ± 3.68	95.82 ± 2.41	-121.52 ± 0.55	12.32 ± 0.17	2.49 ± 0.10	0.66 ± 0.01	6.10 ± 0.04
CD-36 11584	-2.20 ± 0.39	227.27 ± 0.33	10.83 ± 0.18	6.74 ± 0.08	6.49 ± 0.06	0.02 ± 0.00	0.12 ± 0.00
CD-38 13823	251.76 ± 4.14	-166.72 ± 24.55	-41.86 ± 9.94	15.83 ± 2.48	2.33 ± 0.27	0.74 ± 0.01	3.55 ± 0.92
CD-39 6037	-223.93 ± 3.58	-28.97 ± 1.77	-74.37 ± 2.22	14.94 ± 0.37	0.50 ± 0.03	0.94 ± 0.00	3.20 ± 0.22
CD-39 9313	-205.60 ± 3.40	146.13 ± 1.38	-79.07 ± 4.69	12.81 ± 0.20	2.46 ± 0.05	0.68 ± 0.01	2.44 ± 0.21
CD-40 471	-98.37 ± 2.34	12.43 ± 6.59	-16.03 ± 1.81	9.45 ± 0.08	0.26 ± 0.14	0.95 ± 0.03	3.67 ± 0.11
CD-41 4744	-8.88 ± 0.07	215.50 ± 0.17	10.60 ± 0.07	8.26 ± 0.01	7.69 ± 0.01	0.04 ± 0.00	0.17 ± 0.00
CD-41 7816	-19.02 ± 0.09	207.91 ± 0.15	17.03 ± 0.06	7.89 ± 0.00	6.63 ± 0.01	0.09 ± 0.00	0.35 ± 0.00
CD-41 14843	-33.23 ± 0.52	265.83 ± 0.67	31.63 ± 0.35	12.61 ± 0.09	7.16 ± 0.01	0.28 ± 0.00	1.92 ± 0.05
CD-43 7161	-294.32 ± 4.87	20.29 ± 2.16	-73.08 ± 3.05	22.30 ± 0.97	0.30 ± 0.03	0.97 ± 0.00	3.91 ± 0.38
CD-43 8736	71.48 ± 3.14	160.19 ± 1.70	64.40 ± 1.99	7.65 ± 0.03	3.68 ± 0.08	0.35 ± 0.01	1.48 ± 0.06
CD-44 12644	-2.71 ± 1.28	54.26 ± 4.34	-59.02 ± 1.48	6.49 ± 0.04	0.94 ± 0.09	0.75 ± 0.02	1.20 ± 0.04

Continue on the next page

TableB.3–continued.

Star	V_R [kms $^{-1}$]	V_T [kms $^{-1}$]	V_Z [kms $^{-1}$]	r_{ap} [kpc]	r_{peri} [kpc]	ecc.	Z_{max} [kpc]
CD-44 13783	-66.82 ± 0.78	192.02 ± 1.15	-77.22 ± 1.21	7.86 ± 0.10	5.17 ± 0.03	0.21 ± 0.00	2.30 ± 0.04
CD-44 13981	3.57 ± 0.19	247.29 ± 0.58	20.62 ± 0.19	9.11 ± 0.01	6.83 ± 0.04	0.14 ± 0.00	1.19 ± 0.05
CD-44 15269	59.66 ± 3.24	157.89 ± 2.58	-41.21 ± 1.00	8.30 ± 0.05	4.16 ± 0.11	0.33 ± 0.01	2.39 ± 0.10
CD-46 8357	73.59 ± 2.62	208.03 ± 4.27	3.96 ± 1.40	9.46 ± 0.25	5.67 ± 0.11	0.25 ± 0.00	0.27 ± 0.00
CD-46 13658	46.25 ± 0.84	166.32 ± 1.87	2.78 ± 0.87	7.07 ± 0.03	3.97 ± 0.08	0.28 ± 0.01	1.10 ± 0.03
CD-47 14271	10.40 ± 0.25	132.78 ± 3.10	47.95 ± 0.37	7.16 ± 0.02	3.38 ± 0.10	0.36 ± 0.01	2.22 ± 0.06
CD-48 12928	-53.31 ± 1.42	216.62 ± 0.67	71.14 ± 2.51	8.41 ± 0.01	5.65 ± 0.07	0.20 ± 0.01	1.64 ± 0.07
CD-50 823	-363.77 ± 7.60	-51.63 ± 7.13	86.36 ± 2.76	53.99 ± 6.54	0.79 ± 0.11	0.97 ± 0.00	10.87 ± 1.52
CD-50 877	67.65 ± 1.63	147.77 ± 0.47	-57.55 ± 0.75	9.31 ± 0.05	4.12 ± 0.02	0.39 ± 0.00	2.26 ± 0.02
CD-52 976	27.53 ± 0.42	-12.27 ± 1.50	2.22 ± 1.85	8.42 ± 0.01	0.23 ± 0.03	0.95 ± 0.01	1.01 ± 0.02
CD-52 2441	14.47 ± 0.48	221.52 ± 0.57	10.87 ± 0.17	8.67 ± 0.04	7.84 ± 0.02	0.05 ± 0.00	0.24 ± 0.01
CD-52 4849	235.24 ± 13.19	17.85 ± 2.02	-67.30 ± 3.91	13.66 ± 1.14	0.28 ± 0.03	0.96 ± 0.00	3.81 ± 0.67
CD-57 1959	248.51 ± 4.41	119.11 ± 1.28	51.91 ± 1.36	19.32 ± 0.70	2.24 ± 0.02	0.79 ± 0.01	3.34 ± 0.24
CD-58 294	125.12 ± 5.28	110.83 ± 1.45	-74.56 ± 0.32	10.47 ± 0.21	2.53 ± 0.06	0.61 ± 0.01	3.26 ± 0.06
CD-59 6913	90.82 ± 6.03	-95.46 ± 9.36	80.60 ± 2.73	6.73 ± 0.07	1.90 ± 0.23	0.56 ± 0.04	2.51 ± 0.12
CD-62 15	-112.33 ± 0.99	-43.32 ± 5.45	79.93 ± 3.44	9.14 ± 0.07	0.87 ± 0.13	0.83 ± 0.02	3.02 ± 0.17
CPD-62 1126	-18.99 ± 0.13	236.21 ± 0.14	-12.19 ± 0.31	9.55 ± 0.01	7.74 ± 0.00	0.10 ± 0.00	0.30 ± 0.01
HD 6518	140.73 ± 4.26	-21.28 ± 7.28	-106.87 ± 0.44	11.15 ± 0.21	0.46 ± 0.16	0.92 ± 0.03	5.49 ± 0.04
HD 19367	36.37 ± 0.75	18.67 ± 7.30	-86.62 ± 0.95	9.93 ± 0.06	0.54 ± 0.22	0.90 ± 0.04	5.91 ± 0.11
HD 41020	-69.63 ± 1.89	1.24 ± 2.04	2.20 ± 1.26	9.07 ± 0.04	0.02 ± 0.02	1.00 ± 0.01	0.65 ± 0.01
HD 114621	-22.34 ± 0.18	217.21 ± 0.23	-2.43 ± 0.17	7.80 ± 0.01	6.68 ± 0.02	0.08 ± 0.00	0.03 ± 0.00
HD 298008	5.77 ± 0.24	214.89 ± 0.51	-36.99 ± 0.58	7.98 ± 0.01	7.59 ± 0.03	0.02 ± 0.00	0.64 ± 0.01
HD 298296	9.21 ± 0.34	208.54 ± 0.20	-11.04 ± 0.28	8.13 ± 0.01	7.14 ± 0.01	0.06 ± 0.00	0.16 ± 0.00
TYC 5340-1656-1	0.46 ± 4.50	187.57 ± 2.79	-13.05 ± 2.28	8.60 ± 0.01	6.31 ± 0.18	0.15 ± 0.01	0.37 ± 0.03
TYC 5422-1192-1	13.07 ± 0.78	223.97 ± 2.48	-10.97 ± 1.45	11.66 ± 0.49	10.09 ± 0.20	0.07 ± 0.01	0.41 ± 0.05
TYC 5763-1084-1	66.76 ± 1.81	173.94 ± 1.64	0.14 ± 1.52	7.27 ± 0.03	3.99 ± 0.09	0.29 ± 0.01	1.20 ± 0.05
TYC 6002-1724-1	-84.07 ± 4.10	-96.86 ± 5.25	-48.44 ± 2.77	10.31 ± 0.19	2.43 ± 0.18	0.62 ± 0.02	1.60 ± 0.15
TYC 6108-150-1	80.17 ± 5.50	36.58 ± 4.33	-4.27 ± 3.64	8.22 ± 0.07	0.68 ± 0.09	0.85 ± 0.02	1.18 ± 0.10
TYC 6195-815-1	24.35 ± 3.03	93.71 ± 7.29	83.42 ± 3.95	5.66 ± 0.09	1.79 ± 0.17	0.52 ± 0.03	2.19 ± 0.12
TYC 6199-351-1	-82.27 ± 0.37	52.66 ± 7.25	-20.07 ± 2.49	6.89 ± 0.08	0.86 ± 0.14	0.78 ± 0.03	0.83 ± 0.04
TYC 6310-1651-2	-15.62 ± 1.13	242.76 ± 0.17	15.11 ± 0.59	7.58 ± 0.09	5.98 ± 0.06	0.12 ± 0.00	0.80 ± 0.03
TYC 7144-1122-1	-6.12 ± 0.10	221.52 ± 0.36	-11.44 ± 0.49	8.92 ± 0.05	8.44 ± 0.02	0.03 ± 0.00	0.23 ± 0.01
TYC 7351-734-1	25.94 ± 0.21	228.15 ± 0.33	-6.50 ± 0.14	7.79 ± 0.05	6.50 ± 0.03	0.09 ± 0.00	0.31 ± 0.01
TYC 7354-1196-1	-28.18 ± 0.65	261.22 ± 1.35	-2.53 ± 0.52	11.11 ± 0.10	7.16 ± 0.03	0.22 ± 0.01	0.16 ± 0.01
TYC 7427-35-1	39.30 ± 0.32	253.85 ± 0.43	-8.41 ± 0.50	10.31 ± 0.02	6.78 ± 0.02	0.21 ± 0.00	0.44 ± 0.01
TYC 8025-237-1	101.42 ± 6.33	48.21 ± 7.00	-48.99 ± 0.22	8.76 ± 0.13	0.95 ± 0.16	0.80 ± 0.03	2.46 ± 0.09
TYC 8161-753-1	-68.35 ± 0.77	8.79 ± 0.34	6.48 ± 0.34	8.53 ± 0.01	0.15 ± 0.01	0.96 ± 0.00	0.16 ± 0.00
TYC 8178-334-1	19.70 ± 0.49	217.94 ± 0.48	10.88 ± 0.11	8.53 ± 0.03	7.46 ± 0.02	0.07 ± 0.00	0.16 ± 0.00
TYC 8263-2160-1	-45.69 ± 1.72	197.72 ± 1.62	7.87 ± 0.45	7.21 ± 0.05	5.01 ± 0.11	0.18 ± 0.01	0.71 ± 0.04
TYC 8325-6844-1	82.12 ± 0.53	168.58 ± 0.78	-11.76 ± 0.16	8.66 ± 0.02	4.07 ± 0.03	0.36 ± 0.00	0.17 ± 0.00
TYC 8394-14-1	-23.62 ± 1.01	234.72 ± 0.25	-2.79 ± 0.64	7.31 ± 0.07	5.78 ± 0.11	0.12 ± 0.00	1.46 ± 0.09
TYC 8400-1610-1	-16.58 ± 0.22	216.65 ± 0.55	-9.91 ± 0.61	6.79 ± 0.07	6.12 ± 0.06	0.05 ± 0.00	1.06 ± 0.04
TYC 8584-127-1	-8.17 ± 0.22	212.39 ± 0.50	2.67 ± 0.20	8.27 ± 0.02	7.56 ± 0.06	0.05 ± 0.00	0.11 ± 0.00
TYC 8633-2281-1	-271.23 ± 3.24	-35.06 ± 0.93	26.48 ± 0.77	17.04 ± 0.35	0.52 ± 0.01	0.94 ± 0.00	1.44 ± 0.02

Table B.4: Total orbital energy (E), angular momentum (L_Z), radial and vertical actions (J_R , J_Z) and classification (class, see bottom of the table) of the program stars.

Star	E [km 2 s $^{-2}$]	L_Z [kpc kms $^{-1}$]	J_R [kpc kms $^{-1}$]	J_Z [kpc kms $^{-1}$]	Class
BD-11 3235	-63257 ± 498	77 ± 46	573 ± 18	73 ± 12	4
BD-12 5650	-49252 ± 1160	1506 ± 41	6 ± 2	5 ± 1	1
BD-13 934	-50818 ± 316	646 ± 35	365 ± 7	192 ± 27	2
BD-13 3195	-53493 ± 350	431 ± 19	593 ± 19	36 ± 0	2
BD-13 3488	-47972 ± 17	1426 ± 1	20 ± 0	63 ± 1	2
BD-13 6352	-59376 ± 117	443 ± 70	304 ± 22	206 ± 26	2
BD-14 52	-51604 ± 263	890 ± 56	158 ± 18	218 ± 15	2
BD-15 4109	-69673 ± 153	67 ± 62	328 ± 15	281 ± 29	4
BD-15 5449	-46630 ± 1287	310 ± 71	821 ± 66	28 ± 3	4
BD-16 2232	17298 ± 859	-600 ± 28	5048 ± 167	55 ± 0	4
BD-17 3143	-39506 ± 1714	469 ± 94	845 ± 94	78 ± 9	2
BD-17 4251	-15189 ± 425	27 ± 50	1807 ± 16	430 ± 9	5
BD-18 5150	-43547 ± 157	1688 ± 5	17 ± 0	1 ± 0	1
BD-19 6363	-56061 ± 1232	177 ± 118	535 ± 49	200 ± 42	4
CD-23 1855	-52653 ± 492	21 ± 49	843 ± 21	30 ± 1	4
CD-23 11064	-36132 ± 63	1855 ± 8	66 ± 1	32 ± 3	1
CD-24 613	-42832 ± 71	1583 ± 14	22 ± 3	74 ± 6	1
CD-24 1384	-52171 ± 96	458 ± 23	465 ± 15	177 ± 4	4
CD-26 7083	-30348 ± 2052	1919 ± 65	233 ± 28	20 ± 2	2
CD-27 14182	-43472 ± 125	1677 ± 6	16 ± 1	8 ± 1	1
CD-27 15535	-52353 ± 284	1299 ± 13	45 ± 2	35 ± 1	1
CD-27 16505	17075 ± 6102	30 ± 62	5246 ± 1254	132 ± 7	4
CD-28 10039	-51640 ± 114	1249 ± 10	23 ± 1	101 ± 6	2
CD-28 10387	-45021 ± 463	1497 ± 29	109 ± 10	7 ± 1	1
CD-28 16762	-71018 ± 279	172 ± 39	449 ± 14	41 ± 3	4
CD-28 17446	-1048 ± 7479	-188 ± 79	2932 ± 743	116 ± 17	5
CD-29 9391	-48010 ± 236	1449 ± 14	19 ± 2	46 ± 4	1
CD-29 15930	-69693 ± 1037	845 ± 32	68 ± 3	32 ± 3	2
CD-31 16658	-58964 ± 495	1153 ± 18	16 ± 1	40 ± 2	2
CD-31 16922	-46652 ± 602	1580 ± 12	14 ± 7	4 ± 0	1
CD-31 17277	-63962 ± 206	91 ± 55	533 ± 20	105 ± 6	4
CD-32 4154	-38848 ± 424	1861 ± 16	20 ± 1	1 ± 0	1
CD-32 13158	-50870 ± 349	1478 ± 10	0 ± 0	0 ± 0	1
CD-32 14894	-34827 ± 72	1603 ± 24	294 ± 12	31 ± 5	2
CD-33 2721	-53295 ± 194	328 ± 7	420 ± 1	349 ± 13	4
CD-33 15063	-71791 ± 660	-469 ± 71	259 ± 40	46 ± 4	6
CD-34 242	-38883 ± 192	1710 ± 5	59 ± 5	57 ± 3	1
CD-34 3626	-43989 ± 93	1587 ± 1	79 ± 3	2 ± 0	1
CD-34 5597	-45056 ± 112	1626 ± 4	17 ± 0	5 ± 0	1
CD-35 4882	-45803 ± 90	1580 ± 3	37 ± 0	3 ± 0	1
CD-35 13334	-52334 ± 491	1312 ± 16	59 ± 0	18 ± 1	1
CD-35 13661	-58418 ± 2162	-376 ± 79	428 ± 21	139 ± 12	4
CD-35 14807	-44988 ± 499	1580 ± 27	12 ± 1	35 ± 7	1
CD-36 518	-41841 ± 314	768 ± 19	471 ± 24	222 ± 4	4
CD-36 11584	-50787 ± 486	1478 ± 14	0 ± 0	1 ± 0	1
CD-38 13823	-33521 ± 5134	-926 ± 108	767 ± 127	62 ± 10	4
CD-39 6037	-37384 ± 1049	-235 ± 14	1077 ± 19	61 ± 4	5
CD-39 9313	-41310 ± 530	937 ± 17	541 ± 19	48 ± 6	2
CD-40 471	-55925 ± 356	102 ± 54	633 ± 30	123 ± 4	4
CD-41 4744	-42378 ± 44	1752 ± 2	2 ± 0	1 ± 0	1
CD-41 7816	-46474 ± 43	1594 ± 2	8 ± 0	4 ± 0	1
CD-41 14843	-32872 ± 169	1936 ± 1	108 ± 4	38 ± 1	1
CD-43 7161	-22027 ± 1620	154 ± 16	1697 ± 79	43 ± 4	5
CD-43 8736	-56701 ± 150	1072 ± 18	106 ± 6	45 ± 3	2
CD-44 12644	-73263 ± 420	350 ± 30	330 ± 10	37 ± 2	2

Continue on the next page

TableB.4–continued.

Star	E [km 2 s $^{-2}$]	L_Z [kpc kms $^{-1}$]	J_R [kpc kms $^{-1}$]	J_Z [kpc kms $^{-1}$]	Class
CD-44 13783	-50456 ± 418	1271 ± 16	40 ± 2	95 ± 4	2
CD-44 13981	-42152 ± 94	1679 ± 8	24 ± 1	27 ± 2	1
CD-44 15269	-52225 ± 120	1132 ± 23	102 ± 9	90 ± 5	2
CD-46 8357	-44387 ± 1065	1584 ± 33	71 ± 4	2 ± 0	1
CD-46 13658	-58493 ± 449	1106 ± 19	67 ± 3	31 ± 1	1
CD-47 14271	-59639 ± 434	921 ± 26	101 ± 6	93 ± 4	2
CD-48 12928	-47328 ± 209	1438 ± 16	40 ± 2	51 ± 4	2
CD-50 823	8043 ± 3487	-420 ± 58	3795 ± 403	53 ± 2	4
CD-50 877	-48696 ± 114	1204 ± 3	150 ± 4	70 ± 1	2
CD-52 976	-63024 ± 92	-102 ± 13	631 ± 6	20 ± 1	4
CD-52 2441	-40843 ± 150	1804 ± 5	3 ± 0	2 ± 0	1
CD-52 4849	-40935 ± 3397	128 ± 14	1008 ± 74	86 ± 13	5
CD-57 1959	-26202 ± 1354	966 ± 11	1029 ± 45	46 ± 3	4
CD-58 294	-48498 ± 593	842 ± 12	367 ± 21	99 ± 0	2
CD-59 6913	-66800 ± 1307	-570 ± 50	198 ± 21	114 ± 9	6
CD-62 15	-57119 ± 632	-322 ± 40	518 ± 20	98 ± 8	4
CPD-62 1126	-38841 ± 34	1866 ± 1	14 ± 0	2 ± 0	1
HD 6518	-48305 ± 808	-172 ± 59	706 ± 11	187 ± 6	4
HD 19367	-52477 ± 126	173 ± 67	566 ± 37	243 ± 3	4
HD 41020	-60065 ± 214	11 ± 18	746 ± 8	9 ± 0	4
HD 114621	-46641 ± 97	1600 ± 3	7 ± 0	0 ± 0	1
HD 298008	-43253 ± 111	1698 ± 4	1 ± 0	11 ± 0	1
HD 298296	-44276 ± 62	1680 ± 2	5 ± 0	1 ± 0	1
TYC 5340-1656-1	-45200 ± 493	1612 ± 24	26 ± 4	4 ± 1	1
TYC 5422-1192-1	-29474 ± 1248	2295 ± 60	8 ± 3	3 ± 1	1
TYC 5763-1084-1	-57502 ± 459	1117 ± 22	74 ± 3	35 ± 3	1
TYC 6002-1724-1	-49743 ± 1213	-898 ± 53	382 ± 14	34 ± 4	6
TYC 6108-150-1	-63492 ± 355	278 ± 33	517 ± 20	26 ± 3	4
TYC 6195-815-1	-74099 ± 1102	498 ± 52	144 ± 8	112 ± 10	2
TYC 6199-351-1	-71505 ± 793	334 ± 50	381 ± 16	19 ± 2	2
TYC 6310-1651-2	-49417 ± 490	1464 ± 17	14 ± 0	17 ± 1	1
TYC 7144-1122-1	-38736 ± 170	1889 ± 6	1 ± 0	2 ± 0	1
TYC 7351-734-1	-47178 ± 234	1572 ± 8	9 ± 0	3 ± 0	1
TYC 7354-1196-1	-36398 ± 164	1906 ± 2	62 ± 4	1 ± 0	1
TYC 7427-35-1	-39188 ± 28	1795 ± 1	54 ± 1	4 ± 0	1
TYC 8025-237-1	-59167 ± 413	353 ± 53	483 ± 35	75 ± 2	4
TYC 8161-753-1	-63294 ± 67	71 ± 3	677 ± 2	1 ± 0	4
TYC 8178-334-1	-42253 ± 112	1751 ± 4	5 ± 0	1 ± 0	1
TYC 8263-2160-1	-54152 ± 600	1307 ± 23	31 ± 2	15 ± 1	1
TYC 8325-6844-1	-51958 ± 143	1264 ± 7	129 ± 2	1 ± 0	3
TYC 8394-14-1	-50821 ± 560	1367 ± 27	13 ± 1	49 ± 6	1
TYC 8400-1610-1	-51590 ± 444	1387 ± 18	2 ± 0	32 ± 3	1
TYC 8584-127-1	-42710 ± 208	1740 ± 8	2 ± 0	0 ± 0	1
TYC 8633-2281-1	-32584 ± 826	-258 ± 6	1265 ± 24	14 ± 0	5

Class: 1: Thin disk; 2: Thick disk; 3: Thin-Thick transition; 4: Halo; 5: GSE candidate; 6: Seq candidate.

Table B.5: Line list adopted for the star BD-11 3235.

Elt	Ion	Wavelength [nm]	$\log gf$ [cm $^{-1}$]	χ_{exc}	Elt	Ion	Wavelength [nm]	$\log gf$ [cm $^{-1}$]	χ_{exc}
Na	I	568.2632	-0.7060	16956.170	Ti	I	487.0125	0.440	18141.266
Na	I	568.8193	-1.0406	16973.365	Ti	I	497.5291	-2.930	28951.973
Na	I	616.0746	-1.246	16973.365	Ti	I	497.5343	0.150	20209.447
Mg	I	571.1088	-1.724	35051.266	Ti	I	497.8188	-0.303	15877.081
Mg	I	706.0414	-1.351	46403.06	Ti	I	500.0990	0.022	16106.076
Mg	I	781.1122	-1.717	47957.027	Ti	I	500.1018	-2.448	25102.875
Mg	I	809.8707	-2.229	47957.027	Ti	I	500.1128	-1.699	25107.410
Mg	I	821.3013	-2.661	46403.065	Ti	I	500.9645	-2.203	170.133
Mg	I	871.2676	-1.690	59318.793	Ti	I	502.5565	-1.728	21588.494
Mg	I	871.7803	-2.866	59318.793	Ti	I	502.5570	0.250	16458.672
Mg	I	873.6006	-1.758	47957.027	Ti	I	503.8349	0.069	31206.008
Mg	I	892.3569	-1.678	43503.33	Ti	I	503.8398	0.020	11531.761
Al	I	669.6012	-1.569	25347.756	Ti	I	504.3584	-1.677	6742.756
Al	I	877.3888	-0.192	43831.105	Ti	I	506.2102	-0.408	17423.855
Si	I	564.5613	-2.140	39760.285	Ti	I	507.1467	-1.007	11776.812
Si	I	566.5555	-2.040	39683.164	Ti	I	508.6834	-3.285	18037.213
Si	I	568.4484	-1.773	39955.05	Ti	I	508.7058	-0.880	11531.761
Si	I	569.0425	-1.870	39760.285	Ti	I	511.3440	-0.727	11639.811
Si	I	570.1104	-1.953	39760.285	Ti	I	514.5460	-0.718	11776.812
Si	I	577.2027	-3.107	45276.188	Ti	I	514.7762	-1.055	28788.381
Si	I	579.3073	-1.963	39760.285	Ti	I	521.9489	-3.481	19322.984
Si	I	594.8541	-1.231	40991.883	Ti	I	521.9503	-2.166	25068.842
Si	I	613.1573	-1.557	45293.629	Ti	I	521.9634	-1.846	19322.984
Si	I	615.5134	-0.855	45321.848	Ti	I	521.9702	-2.236	170.133
Si	I	623.7319	-1.070	45276.188	Ti	I	523.8537	-0.916	16875.123
Si	I	624.4114	-2.288	45293.629	Ti	I	523.8586	-2.074	6842.962
Si	I	655.5463	-1.163	48264.293	Ti	I	528.2376	-1.810	8492.422
Si	I	672.1848	-1.140	47284.062	Ti	I	528.2554	-2.838	29914.736
Si	I	700.3569	-0.939	48102.32	Ti	I	529.5776	-1.577	8602.344
Si	I	793.2348	-0.469	48102.323	Ti	I	529.5839	-2.453	25102.875
Si	I	855.6777	-0.151	59034.988	Ti	I	542.6249	-2.950	170.133
Si	I	855.6805	-0.407	61617.170	Ti	I	542.6549	-2.714	30039.170
Si	I	874.2446	-0.071	58786.860	Ti	I	548.9873	-0.647	27750.135
Si	I	875.2007	0.078	58774.368	Ti	I	549.0130	-1.001	26892.936
Si	I	889.2720	-0.758	48264.292	Ti	I	549.0148	-0.877	11776.812
S	I	921.2863	0.396	63475.051	Ti	I	549.0198	-2.504	29661.250
Ca	I	468.5268	-0.880	23652.305	Ti	I	568.9461	-0.413	18525.059
Ca	I	526.0387	-1.900	20335.359	Ti	I	586.6367	-1.055	26657.416
Ca	I	534.9465	-0.428	21849.635	Ti	I	586.6451	-0.784	8602.344
Ca	I	551.2980	-0.300	23652.305	Ti	I	586.6808	-2.213	26803.420
Ca	I	558.1965	-0.517	20349.260	Ti	I	591.8536	-1.640	8602.344
Ca	I	559.0114	-0.547	20335.359	Ti	I	595.3159	-0.273	15220.393
Ca	I	559.4462	-0.050	20349.260	Ti	I	594.1382	-3.395	25388.330
Ca	I	560.1277	-0.496	20371.000	Ti	I	594.1696	-1.288	25227.223
Ca	I	585.7451	0.230	23652.305	Ti	I	594.1752	-1.510	8492.422
Ca	I	610.2439	-3.373	20349.260	Ti	I	597.8541	-0.440	15108.111
Ca	I	616.1297	-1.266	20349.260	Ti	I	597.8878	-3.302	32514.566
Ca	I	616.6439	-1.142	20335.359	Ti	I	606.4626	-1.888	8436.618
Ca	I	616.9042	-0.540	20349.260	Ti	I	609.1171	-0.367	18287.555
Ca	I	616.9563	-0.270	20371.00	Ti	I	612.6216	-1.369	8602.344
Ca	I	644.9808	-0.550	20335.359	Ti	I	612.6273	-2.845	25438.908
Ca	I	645.5598	-1.350	20349.260	Ti	I	625.8102	-0.299	11639.811
Ca	I	647.1662	-0.590	20371.000	Ti	I	626.1099	-0.423	11531.761
Ca	I	649.9650	-0.590	20349.260	Ti	I	626.1124	-1.571	25227.223
Ca	I	671.7681	-0.610	21849.635	Ti	I	633.6099	-1.687	11639.811
Sc	I	568.6847	0.370	11610.280	Ti	I	655.3671	-2.048	26564.400
Ti	I	474.2789	0.010	18037.213	Ti	I	655.3682	-2.915	33660.652
Ti	I	475.9141	-3.002	22404.738	...				
Ti	I	475.9270	0.570	18192.570					

Table B.6: Abundances and line-to-line dispersion (σ) of elements in their ionisation state from Na I to Sc II in [X/H].

Star	Na I	σ	Mg I	σ	Al I	σ	Si I	σ	Ca I	σ	Sc I	σ	Sc II	σ
BD-11 3235	-2.28	0.03	-1.53	0.04	-2.06	0.19	-1.70	0.12	-1.73	0.05	-2.05	0.00	-1.59	0.13
BD-13 934	-2.00	0.09	-1.39	0.06	-1.82	0.12	-1.51	0.08	-1.53	0.06	-1.89	0.00	-1.56	0.12
BD-13 3195	-1.31	0.01	-0.72	0.10	-0.88	0.07	-0.82	0.12	-0.96	0.07	—	—	-1.03	0.14
BD-15 5449	-1.89	0.02	-1.73	0.09	-1.28	0.05	-1.74	0.13	-1.79	0.06	-2.19	0.00	-1.87	0.06
BD-16 2232	-1.87	0.04	-1.28	0.07	-1.78	0.10	-1.41	0.12	-1.37	0.05	-1.65	0.00	-1.51	0.09
BD-17 3143	-1.76	0.05	-1.21	0.08	-1.69	0.12	-1.43	0.11	-1.27	0.04	-1.47	0.00	-1.68	0.09
BD-19 6363	-2.52	0.04	-1.96	0.03	—	—	-1.99	0.15	-2.03	0.06	-2.58	0.00	-2.27	0.02
CD-23 1855	-2.01	0.11	-1.51	0.07	-1.92	0.11	-1.55	0.11	-1.55	0.05	-1.80	0.00	-1.65	0.11
CD-27 16505	-1.39	0.05	-0.86	0.07	-1.25	0.07	-0.96	0.14	-0.99	0.05	—	—	-0.93	0.14
CD-28 10039	-1.09	0.06	-0.74	0.06	-0.95	0.07	-0.91	0.13	-0.87	0.04	—	—	-0.96	0.13
CD-28 16762	-1.49	0.04	-1.21	0.09	-1.01	0.09	-1.29	0.12	-1.25	0.05	-1.63	0.00	-1.33	0.13
CD-28 17446	-2.02	0.03	-1.41	0.07	-1.84	0.11	-1.48	0.08	-1.51	0.05	-1.87	0.00	-1.41	0.11
CD-29 15930	-1.82	0.03	-1.24	0.05	-1.64	0.13	-1.43	0.12	-1.39	0.06	-1.72	0.00	-1.42	0.12
CD-33 2721	-1.66	0.041	-1.48	0.07	-1.19	0.08	-1.54	0.08	-1.49	0.06	-1.85	0.00	-1.72	0.09
CD-33 15063	-1.65	0.05	-1.19	0.08	-1.31	0.06	-1.34	0.10	-1.39	0.05	-1.76	0.00	-1.37	0.15
CD-36 518	-1.92	0.04	-1.32	0.05	-1.75	0.11	-1.44	0.11	-1.40	0.05	-1.83	0.00	-1.44	0.09
CD-38 13823	-2.84	0.00	-1.97	0.09	—	—	-2.19	0.16	-2.40	0.09	-2.86	0.00	-2.63	0.12
CD-39 6037	-1.21	0.09	-0.64	0.08	-1.01	0.07	-0.75	0.07	-0.85	0.05	—	—	-0.85	0.15
CD-39 9313	-1.85	0.04	-1.29	0.07	-1.57	0.00	-1.35	0.05	-1.41	0.04	—	—	-1.45	0.02
CD-40 471	-2.73	0.05	-1.93	0.00	—	—	-2.02	0.09	-2.11	0.09	-2.71	0.00	-2.23	0.09
CD-43 7161	-1.68	0.06	-1.06	0.08	-1.50	0.09	-1.17	0.12	-1.21	0.06	—	—	-1.15	0.10
CD-44 12644	-1.54	0.04	-0.98	0.06	-1.23	0.13	-1.16	0.07	-1.03	0.03	-1.32	0.00	-1.32	0.10
CD-44 15269	-1.63	0.06	-0.88	0.08	-1.43	0.09	-0.97	0.09	-1.09	0.09	-1.48	0.00	-1.17	0.15
CD-52 976	-2.18	0.02	-1.50	0.05	-2.11	0.00	-1.55	0.05	-1.59	0.07	-2.03	0.00	-1.72	0.12
CD-57 1959	-2.19	0.03	-1.51	0.04	-2.09	0.00	-1.54	0.07	-1.64	0.05	—	—	-1.63	0.11
CD-62 15	-2.23	0.04	-1.58	0.08	-1.99	0.00	-1.73	0.14	-1.74	0.05	-2.27	0.00	-1.89	0.03
HD 6518	-1.52	0.04	-0.97	0.07	-1.36	0.08	-1.05	0.08	-1.05	0.06	-1.34	0.00	-0.97	0.12
HD 19367	-2.32	0.09	-1.66	0.08	-2.24	0.00	-1.79	0.09	-1.77	0.05	-1.95	0.00	-1.91	0.08
TYC 6002-1724-1	-2.54	0.06	-1.84	0.09	—	—	-1.95	0.07	-1.96	0.05	-2.40	0.00	-2.19	0.04
TYC 6199-351-1	-1.77	0.05	-1.09	0.09	-1.51	0.09	-1.15	0.07	-1.30	0.05	-1.71	0.00	-1.25	0.01
TYC 8161-753-1	-1.78	0.04	-1.11	0.07	-1.55	0.07	-1.18	0.12	-1.28	0.05	-1.78	0.00	-1.22	0.14
TYC 8633-2281-1	-2.13	0.13	-1.49	0.06	-1.88	0.11	-1.61	0.07	-1.67	0.06	—	—	-1.69	0.15

Appendix C: Remarks on individual stars

Appendix C.1: BD-14 52

This star was investigated in the 437+760 wavelength range. It is an active star. According to *Gaia* DR3 this star is an SB1 binary with a period of 306 days, a radial velocity semi-amplitude of 1.15 km/s and centre of mass velocity of 60.2 km/s close to our adopted radial velocity. The orbit has a low eccentricity of 0.16.

Appendix C.2: BD-17 4250

This metal-poor star has been analysed in the 437+760 range, it is active as indicated by Ca II-H and -K emission and P-Cygni (and inverse) profiles on H α .

Appendix C.3: BD-15 4109

This star is metal-poor, it was investigated in the 437+760 range. It is active as implied by the Ca II-H and -K emission and P-Cygni (and inverse) profiles on H α .

Appendix C.4: CD-23 11064

This star is cool, the [Mucciarelli et al. \(2021\)](#) calibration provides an effective temperature of 3748 K we ran it at fixed $T_{\text{eff}} = 3750$ K to avoid extrapolation.

Appendix C.5: CD-24 613

This star is cool and was analysed only in the RVS range with the COOL grid. MyGIsFOS required a shift of +5.6 km s $^{-1}$ with respect to the *Gaia* radial velocity.

Table B.7: Abundances and line-to-line dispersion (σ) of elements in their ionisation state from Ti I to Mn II in [X/H].

Star	Ti I	σ	Ti II	σ	V I	σ	V II	σ	Cr I	σ	Cr II	σ	Mn I	σ	Mn II	σ
BD-11 3235	-1.75	0.07	-1.51	0.08	-2.10	0.07	-1.94	0.14	-2.10	0.10	-1.89	0.07	-2.39	0.08	-2.46	0.00
BD-13 934	-1.56	0.06	-1.44	0.08	-1.92	0.06	-1.94	0.05	-1.89	0.09	-1.76	0.03	-2.21	0.09	—	—
BD-13 3195	-0.92	0.08	-0.99	0.08	-1.25	0.09	-1.34	0.20	-1.29	0.11	-1.32	0.00	-1.55	0.09	—	—
BD-15 5449	-1.87	0.05	-1.71	0.04	-2.20	0.07	-2.25	0.04	-2.15	0.14	-2.05	0.08	-2.49	0.11	—	—
BD-16 2232	-1.41	0.06	-1.38	0.09	-1.76	0.05	-1.76	0.02	-1.75	0.09	-1.69	0.03	-2.01	0.07	-2.01	0.00
BD-17 3143	-1.19	0.09	-1.48	0.13	-1.54	0.07	-1.95	0.00	-1.58	0.11	-1.81	0.06	-1.91	0.09	—	—
BD-19 6363	-2.14	0.07	-1.92	0.09	-2.63	0.14	-2.27	0.09	-2.58	0.12	-2.42	0.14	-2.89	0.04	-2.65	0.00
CD-23 1855	-1.57	0.07	-1.57	0.11	-1.93	0.07	-1.86	0.07	-1.98	0.07	-1.96	0.09	-2.23	0.05	-2.13	0.00
CD-27 16505	-0.95	0.08	-0.92	0.10	-1.24	0.07	-0.91	0.00	-1.25	0.13	-1.09	0.00	-1.52	0.13	—	—
CD-28 10039	-0.81	0.08	-0.92	0.09	-1.09	0.08	-0.82	0.00	-1.06	0.14	-0.98	0.00	-1.46	0.12	—	—
CD-28 16762	-1.29	0.07	-1.25	0.08	-1.60	0.07	-1.61	0.13	-1.58	0.13	-1.55	0.10	-1.84	0.05	—	—
CD-28 17446	-1.53	0.06	-1.27	0.08	-1.89	0.04	-1.99	0.00	-1.87	0.11	-1.52	0.00	-2.16	0.09	—	—
CD-29 15930	-1.38	0.06	-1.29	0.06	-1.75	0.06	-1.99	0.05	-1.77	0.09	-1.66	0.04	-2.08	0.12	—	—
CD-33 2721	-1.49	0.07	-1.56	0.07	-1.85	0.04	-1.95	0.04	-1.84	0.08	-1.77	0.25	-2.12	0.06	-2.09	0.00
CD-33 15063	-1.36	0.08	-1.25	0.13	-1.75	0.06	-1.84	0.09	-1.74	0.09	-1.54	0.00	-2.07	0.10	—	—
CD-36 518	-1.44	0.06	-1.34	0.05	-1.80	0.05	-1.70	0.03	-1.74	0.09	-1.59	0.01	-2.03	0.06	-2.01	0.00
CD-38 13823	-2.42	0.06	-2.44	0.11	-2.72	0.15	-2.72	0.06	-2.52	0.08	-2.53	0.06	-2.56	0.09	-2.63	0.00
CD-39 6037	-0.87	0.07	-0.77	0.08	-1.15	0.07	-0.90	0.00	-1.06	0.16	—	—	-1.20	0.11	—	—
CD-39 9313	-1.36	0.06	-1.25	0.06	-1.69	0.05	—	—	-1.66	0.06	-1.62	0.07	-1.97	0.12	—	—
CD-40 471	-2.12	0.09	-2.08	0.09	-2.51	0.09	-2.58	0.11	-2.51	0.06	-2.55	0.14	-2.85	0.07	-2.73	0.00
CD-43 7161	-1.17	0.07	-1.07	0.07	-1.53	0.09	—	—	-1.51	0.11	-1.41	0.05	-1.81	0.13	—	—
CD-44 12644	-0.98	0.06	-1.22	0.10	-1.31	0.04	—	—	-1.39	0.07	-1.10	0.00	-1.61	0.05	—	—
CD-44 15269	-1.10	0.07	-0.94	0.07	-1.47	0.05	—	—	-1.43	0.07	-1.39	0.08	-1.76	0.10	—	—
CD-52 976	-1.64	0.07	-1.53	0.13	-1.97	0.06	-1.78	0.00	-1.97	0.08	-1.88	0.03	-2.23	0.08	-2.14	0.00
CD-57 1959	-1.73	0.07	-1.51	0.05	-2.07	0.07	-1.86	0.08	-2.03	0.11	-1.76	0.03	-2.28	0.05	-2.28	0.00
CD-62 15	-1.73	0.13	-1.72	0.09	-2.09	0.13	-2.06	0.09	-2.17	0.09	-2.11	0.09	-2.41	0.04	-2.33	0.00
HD 6518	-1.08	0.08	-0.99	0.07	-1.41	0.09	-1.51	0.09	-1.41	0.11	-1.38	0.08	-1.65	0.06	—	—
HD 19367	-1.75	0.08	-1.79	0.08	-2.09	0.07	-2.08	0.00	-2.10	0.09	-2.11	0.04	-2.37	0.05	-2.31	0.00
TYC 6002-1724-1	-2.01	0.06	-1.95	0.07	-2.39	0.03	-2.31	0.07	-2.44	0.07	-2.41	0.09	-2.79	0.07	-2.59	0.00
TYC 6199-351-1	-1.36	0.07	-1.08	0.07	-1.72	0.06	-1.74	0.12	-1.76	0.08	-1.48	0.11	-1.97	0.07	—	—
TYC 8161-753-1	-1.43	0.07	-1.11	0.09	-1.81	0.06	-1.67	0.11	-1.80	0.12	-1.49	0.09	-2.11	0.09	—	—
TYC 8633-2281-1	-1.68	0.08	-1.46	0.12	-1.99	0.04	-2.05	0.04	-1.99	0.08	-1.85	0.06	-2.27	0.08	—	—

Appendix C.6: CD-27 14182

Was analysed in the 437+760 range. There is a tiny emission in Ca II-H and -K lines. No evidence of Li I doublet.

Appendix C.7: CD-28 10387

Was analysed in the 437+760 range. Normal H α , tiny emission in Ca II-H and -K lines. No evidence of Li I doublet.

Appendix C.8: CD-29 9391

Was analysed in the RVS range with the COOL grid. Our spectrum required a shift of -1.05 km s^{-1} with respect to the *Gaia* radial velocity.

Appendix C.9: CD-31 17277

Gaia DR3 classifies it as Long Period Variable (LPV) but does not provide a period.

Appendix C.10: CD-32 13158

The star has been analysed in the 437+760 range. Normal H α , tiny emission in Ca II-H and -K lines. No evidence of Li I doublet. The star is of solar metallicity and has a sizeable rotational velocity. Comparison with the evolutionary tracks of [Ekström et al. \(2012\)](#) implies a mass of $6 M_\odot$ and an age of 70 Myr.

Appendix C.11: CD-34 242

This star is cool and was analysed only in the RVS range with the COOL grid. MyGIsFOS required a shift of $+2.6 \text{ km s}^{-1}$ with respect to the *Gaia* radial velocity.

Table B.8: Abundances and line-to-line dispersion (σ) of elements in their ionisation state from Fe I to Zn I in [X/H].

Star	Fe I	σ	Fe II	σ	Co I	σ	Ni I	σ	Cu I	σ	Zn I	σ
BD-11 3235	-2.11	0.14	-1.75	0.13	-1.97	0.13	-2.09	0.15	-2.59	0.12	-1.98	0.00
BD-13 934	-1.93	0.12	-1.73	0.12	-1.81	0.13	-1.91	0.13	-2.33	0.14	-1.84	0.00
BD-13 3195	-1.41	0.15	-1.43	0.12	-1.19	0.15	-1.34	0.13	-1.61	0.11	-1.46	0.03
BD-15 5449	-2.19	0.12	-1.94	0.09	-2.05	0.14	-2.17	0.14	-2.68	0.11	-	-
BD-16 2232	-1.77	0.12	-1.71	0.10	-1.63	0.15	-1.76	0.15	-2.20	0.14	-1.83	0.00
BD-17 3143	-1.68	0.14	-1.91	0.11	-1.54	0.13	-1.71	0.15	-2.06	0.06	-1.94	0.00
BD-19 6363	-2.51	0.12	-2.37	0.13	-2.49	0.08	-2.44	0.13	-	-	-2.25	0.02
CD-23 1855	-1.96	0.11	-1.89	0.09	-1.84	0.11	-1.93	0.11	-2.41	0.09	-1.95	0.02
CD-27 16505	-1.33	0.16	-1.09	0.14	-1.18	0.14	-1.29	0.13	-1.73	0.09	-1.49	0.00
CD-28 10039	-1.12	0.20	-1.02	0.14	-1.10	0.15	-1.16	0.11	-1.46	0.12	-1.45	0.01
CD-28 16762	-1.63	0.13	-1.52	0.12	-1.52	0.13	-1.66	0.13	-2.09	0.13	-1.69	0.00
CD-28 17446	-1.84	0.17	-1.43	0.14	-1.79	0.14	-1.85	0.14	-2.35	0.10	-1.85	0.01
CD-29 15930	-1.79	0.11	-1.66	0.12	-1.67	0.15	-1.79	0.14	-2.16	0.13	-	-
CD-33 2721	-1.88	0.12	-1.91	0.13	-1.81	0.13	-1.91	0.14	-2.34	0.08	-2.02	0.00
CD-33 15063	-1.80	0.16	-1.61	0.15	-1.65	0.15	-1.81	0.15	-2.20	0.12	-1.75	0.01
CD-36 518	-1.74	0.11	-1.59	0.12	-1.73	0.13	-1.81	0.11	-2.28	0.12	-1.81	0.03
CD-38 13823	-2.46	0.14	-2.45	0.14	-2.35	0.12	-2.38	0.11	-3.24	0.00	-2.59	0.02
CD-39 6037	-0.99	0.16	-0.78	0.11	-1.03	0.13	-1.04	0.12	-1.49	0.17	-	-
CD-39 9313	-1.68	0.15	-1.47	0.15	-1.57	0.15	-1.67	0.13	-2.16	0.12	-1.63	0.00
CD-40 471	-2.48	0.14	-2.47	0.13	-2.36	0.11	-2.49	0.13	-2.95	0.11	-2.529	0.03
CD-43 7161	-1.50	0.13	-1.34	0.16	-1.41	0.14	-1.50	0.13	-1.99	0.09	-1.59	0.00
CD-44 12644	-1.44	0.12	-1.66	0.07	-1.26	0.12	-1.46	0.14	-1.84	0.07	-1.65	0.00
CD-44 15269	-1.39	0.15	-1.19	0.17	-1.31	0.12	-1.37	0.14	-1.85	0.09	-	-
CD-52 976	-1.90	0.09	-1.79	0.09	-1.86	0.09	-1.92	0.09	-2.44	0.07	-1.86	0.02
CD-57 1959	-2.00	0.12	-1.71	0.11	-1.94	0.08	-2.02	0.09	-2.55	0.08	-1.91	0.03
CD-62 15	-2.11	0.12	-2.06	0.11	-2.06	0.15	-2.11	0.13	-2.47	0.06	-2.06	0.02
HD 6518	-1.44	0.14	-1.29	0.14	-1.31	0.13	-1.43	0.12	-1.88	0.07	-1.47	0.04
HD 19367	-2.12	0.14	-2.08	0.11	-2.00	0.11	-2.13	0.14	-2.59	0.05	-2.23	0.03
TYC 6002-1724-1	-2.34	0.12	-2.30	0.08	-2.34	0.08	-2.35	0.11	-2.88	0.00	-2.35	0.03
TYC 6199-351-1	-1.66	0.16	-1.29	0.18	-1.53	0.15	-1.62	0.14	-2.09	0.11	-1.54	0.05
TYC 8161-753-1	-1.77	0.13	-1.56	0.12	-1.66	0.12	-1.76	0.10	-2.20	0.15	-1.51	0.02
TYC 8633-2281-1	-2.05	0.19	-1.80	0.12	-1.97	0.09	-2.02	0.12	-2.45	0.14	-2.02	0.00

Appendix C.12: CD-35 13334

This star is cool and was analysed only in the RVS range with the COOL grid. MyGIsFOS required a shift of $+1.8 \text{ km s}^{-1}$ with respect to the *Gaia* radial velocity.

Appendix C.13: CD-35 13661

According to *Gaia* this star is an SB1 binary with a period of 2 days and a semi-amplitude of 1.35 km s^{-1} . The centre of mass radial velocity is $+59.02 \text{ km s}^{-1}$, very close to our adopted radial velocity. The eccentricity is low, 0.12. Analysed in the 437+760 range. H α with P-Cygni and emission on Ca II-H and -K lines. No evident feature at the Li I doublet wavelength.

Appendix C.14: CD-45 8357

This star is classified as an RS CVn binary in the *Gaia* DR3 catalogue. Our spectrum does not show a secondary spectrum (as expected for an RS CVn). The radial velocity from our UVES spectrum is $-20.5 \pm 0.33 \text{ km/s}$, to be compared to the value provided by *Gaia* -32.39 ± 5.24 . Although the two values are compatible at 2.2σ , we consider this as a clear indication that the star's radial velocity is varying, as is the very large error in the *Gaia* radial velocity, incompatible with a star of this brightness. The Ca II H&K line show a very strong emission, further supporting the RS CVn classification of this star. A chemical analysis of such a star is beyond the scope of our paper, however from comparison with synthetic spectra we estimate the metallicity to be roughly solar and the $v \sin i \sim 20 \text{ km s}^{-1}$

Appendix C.15: CD-48 12928

Gaia DR3 classifies this star as LPV with a period of 289.27 days and an amplitude of 0.16 mag. The effective temperature from the [Mucciarelli et al. \(2021\)](#) is 3642 K we run MyGIsFOS in the RVS range with the COOL grid and $T_{\text{eff}} = 3750 \text{ K}$ to avoid extrapolation. Our UVES spectrum requires a shift of -1.1 km s^{-1} with respect to the *Gaia* radial velocity.

Appendix C.16: CD-50 823

Analysed in the 437+760 range. H α shows emissions, Ca II-H and -K lines have emission cores. No Li I doublet.

Table B.9: Abundances and line-to-line dispersion (σ) of elements in their ionisation state from Rb I to La II in [X/H].

Star	Rb I	σ	Sr I	σ	Y II	σ	Zr II	σ	Ba II	σ	La II	σ
BD-11 3235	-1.46	0.00	-2.53	0.00	-2.00	0.06	-1.52	0.07	-1.92	0.08	-2.03	0.05
BD-13 934	—	—	-1.97	0.00	-1.66	0.07	-1.25	0.12	-1.66	0.05	-1.60	0.03
BD-13 3195	-0.82	0.00	—	—	-1.07	0.05	-0.71	0.09	-0.95	0.05	-1.08	0.07
BD-15 5449	—	—	-2.46	0.00	-2.18	0.06	-1.75	0.18	-1.94	0.08	-2.06	0.03
BD-16 2232	—	—	-2.04	0.00	-1.72	0.06	-1.25	0.06	-1.66	0.04	-1.54	0.05
BD-17 3143	—	—	-1.92	0.00	-1.88	0.08	-1.35	0.07	-1.68	0.03	-1.61	0.06
BD-19 6363	—	—	-2.61	0.00	-2.39	0.04	-1.97	0.08	-2.39	0.04	-2.29	0.02
CD-23 1855	—	—	-2.18	0.00	-1.70	0.07	-1.20	0.05	-1.68	0.06	-1.55	0.06
CD-27 16505	-1.35	0.00	—	—	-1.19	0.10	-0.76	0.01	-1.04	0.00	-1.08	0.01
CD-28 10039	-1.10	0.00	—	—	-1.04	0.00	-0.67	0.03	-0.84	0.09	-0.69	0.07
CD-28 16762	-1.23	0.00	-1.96	0.00	-0.64	0.09	-1.12	0.03	-1.35	0.05	-1.35	0.09
CD-28 17446	—	—	-2.35	0.00	-1.66	0.08	-1.15	0.06	-1.39	0.01	-1.42	0.05
CD-29 15930	—	—	-2.15	0.00	-1.59	0.06	-1.09	0.08	-1.54	0.07	-1.61	0.12
CD-33 2721	—	—	-2.12	0.00	-1.96	0.09	-1.49	0.07	-1.72	0.06	-1.74	0.06
CD-33 15063	—	—	-1.95	0.00	-1.45	0.07	-1.01	0.12	-0.89	0.07	-1.18	0.09
CD-36 518	—	—	-1.99	0.00	-1.65	0.06	-1.19	0.05	-1.40	0.05	-1.41	0.06
CD-38 13823	—	—	—	—	-3.15	0.01	-2.84	0.08	-3.17	0.03	-2.94	0.04
CD-39 6037	-1.22	0.00	—	—	-1.060	0.07	—	—	-0.47	0.09	-0.84	0.03
CD-39 9313	—	—	-2.06	0.00	-1.56	0.09	-1.24	0.12	-1.08	0.06	-1.39	0.03
CD-40 471	-1.35	0.00	-2.72	0.00	-2.56	0.08	-2.12	0.09	-2.24	0.09	-2.28	0.06
CD-43 7161	-1.52	0.00	-2.08	0.00	-1.45	0.06	-0.97	0.04	-1.13	0.04	-1.28	0.04
CD-44 12644	—	—	-1.51	0.00	-1.482	0.09	-0.93	0.07	-1.05	0.05	-1.05	0.07
CD-44 15269	-1.08	0.00	-1.79	0.00	-1.29	0.05	-0.87	0.05	-0.79	0.09	-1.34	0.07
CD-52 976	—	—	-2.29	0.00	-2.13	0.06	-1.59	0.03	-1.76	0.11	-1.89	0.06
CD-57 1959	—	—	-2.33	0.00	-1.96	0.08	-1.48	0.07	-1.77	0.04	-1.75	0.06
CD-62 15	—	—	-2.27	0.00	-2.09	0.07	-1.66	0.02	-2.09	0.01	-2.05	0.03
HD 6518	-1.61	0.00	-1.87	0.00	-1.442	0.11	-0.93	0.05	-1.28	0.06	-1.32	0.07
HD 19367	—	—	-2.38	0.00	-2.17	0.09	-1.72	0.12	-1.89	0.04	-1.84	0.07
TYC 6002-1724-1	—	—	-2.53	0.00	-2.55	0.06	-2.03	0.01	-2.61	0.05	-2.49	0.05
TYC 6199-351-1	-1.61	0.00	-2.17	0.00	-1.59	0.11	-1.05	0.04	-1.43	0.07	-1.53	0.05
TYC 8161-753-1	-1.39	0.00	-1.95	0.00	-1.41	0.07	-0.90	0.05	-1.13	0.04	-1.22	0.03
TYC 8633-2281-1	—	—	-2.44	0.00	-2.05	0.10	-1.47	0.05	-1.67	0.06	-1.79	0.05

Appendix C.17: CD-50 877

Gaia DR3 classifies this star as LPV, but does not provide a period. The effective temperature from the Mucciarelli et al. (2021) is 3733 K we run MyGIsFOS in the RVS range with the COOL grid and $T_{\text{eff}} = 3750$ K to avoid extrapolation. Our UVES spectrum requires a shift of -2.0 km s^{-1} with respect to the *Gaia* radial velocity.

Appendix C.18: CD-52 2441

This star is an SB2 binary, the radial velocities of the two components are provided in Table C.1.

Appendix C.19: CD-52 4849

According to the *Gaia* DR3 catalogue this is an SB1 binary with a period of 3.5 days and a semi-amplitude of 1.4 km s^{-1} . The centre of mass radial velocity is 150.65 km s^{-1} , very close to our adopted radial velocity. The eccentricity of the orbit is 0.26. Analysed in the 437+760 range. H α shows emissions, Ca II-H and -K lines have emission cores. No Li I doublet.

Appendix C.20: CD-58 294

Gaia DR3 classifies it as LPV with a period of 176.72 d and an amplitude of 0.03 mag. The effective temperature from the Mucciarelli et al. (2021) is 3707 K we run MyGIsFOS in the RVS range with the COOL grid and $T_{\text{eff}} = 3750$ K to avoid extrapolation. Our UVES spectrum requires a shift of +0.7 km s^{-1} with respect to the *Gaia* radial velocity.

Appendix C.21: CD-59 6913

Gaia DR3 classifies this star as LPV with a period of 344.88 days and an amplitude of 0.05 mag. Analysed in the 437+760 range. H α shows emissions, Ca II-H and -K lines have emission cores. No Li I doublet.

Table B.10: Abundances and line-to-line dispersion (σ) of elements in their ionisation state from Ce II to Eu II in [X/H].

Star	Ce II	σ	Pr II	σ	Nd II	σ	Sm II	σ	Eu II	σ
BD-11 3235	-2.14	0.12	-1.98	0.05	-1.91	0.06	-1.70	0.09	-1.56	0.00
BD-13 934	-1.77	0.09	-1.62	0.01	-1.54	0.02	-1.39	0.05	-1.19	0.00
BD-13 3195	-1.11	0.08	-1.16	0.02	—	—	-0.89	0.02	-1.00	0.00
BD-15 5449	-2.18	0.08	-2.11	0.04	-1.99	0.03	-1.89	0.02	-1.88	0.00
BD-16 2232	-1.66	0.05	-1.52	0.04	-1.45	0.01	-1.23	0.03	-1.02	0.00
BD-17 3143	-1.71	0.08	-1.58	0.01	-1.55	0.03	-1.41	0.04	-1.31	0.00
BD-19 6363	-2.37	0.04	—	—	-2.22	0.04	-1.97	0.05	-2.15	0.00
CD-23 1855	-1.67	0.01	—	—	-1.45	0.02	-1.26	0.02	-1.15	0.00
CD-27 16505	-1.25	0.06	-0.93	0.00	—	—	-0.69	0.03	-0.48	0.00
CD-28 10039	-1.12	0.07	-0.86	0.00	—	—	—	—	-0.49	0.00
CD-28 16762	-1.26	0.26	-1.32	0.00	-1.28	0.04	-1.14	0.07	-0.93	0.00
CD-28 17446	-1.54	0.11	-1.38	0.07	-1.33	0.02	-1.09	0.02	-0.86	0.00
CD-29 15930	-1.74	0.10	-1.58	0.03	—	—	-1.41	0.01	-1.24	0.00
CD-33 2721	-1.88	0.06	-1.73	0.00	-1.69	0.03	-1.54	0.01	-1.44	0.00
CD-33 15063	-1.21	0.08	-1.43	0.00	-1.16	0.06	-1.35	0.03	-1.43	0.00
CD-36 518	-1.49	0.05	-1.42	0.00	-1.34	0.03	-1.22	0.04	-1.06	0.00
CD-38 13823	—	—	—	—	-2.79	0.04	-2.69	0.03	-2.48	0.00
CD-39 6037	-0.87	0.13	-0.79	0.00	—	—	-0.48	0.09	-0.38	0.00
CD-39 9313	-1.46	0.0	-1.49	0.03	-1.34	0.03	-1.31	0.07	-1.14	0.00
CD-40 471	-2.414	0.03	-2.17	0.00	-2.17	0.06	-1.91	0.04	-1.75	0.00
CD-43 7161	-1.35	0.06	-1.19	0.02	-1.14	0.00	-1.05	0.09	-0.71	0.00
CD-44 12644	-1.12	0.07	-1.13	0.00	-1.01	0.02	-0.93	0.05	-0.89	0.00
CD-44 15269	-1.38	0.04	-1.38	0.03	-1.26	0.06	-1.06	0.04	-0.94	0.00
CD-52 976	-1.99	0.04	-1.86	0.00	-1.79	0.03	-1.62	0.01	-1.56	0.00
CD-57 1959	-1.86	0.05	-1.71	0.00	-1.69	0.02	-1.46	0.05	-1.23	0.00
CD-62 15	-2.16	0.02	—	—	-1.988	0.03	-1.85	0.05	-1.76	0.00
HD 6518	-1.41	0.09	-1.22	0.00	—	—	-0.97	0.01	-0.81	0.00
HD 19367	-1.95	0.05	-1.72	0.00	-1.80	0.04	-1.56	0.07	-1.35	0.00
TYC 6002-1724-1	—	—	—	—	-2.41	0.00	-2.20	0.09	-2.26	0.00
TYC 6199-351-1	-1.60	0.11	-1.46	0.02	—	—	-1.19	0.02	-1.07	0.00
TYC 8161-753-1	-1.28	0.08	-1.35	0.00	-1.19	0.04	-1.19	0.09	-1.07	0.00
TYC 8633-2281-1	-1.89	0.09	-1.78	0.00	-1.74	0.04	-1.60	0.06	-1.44	0.00

Appendix C.22: CPD–62 1126

Analysed in the 437+760 range, but only for wavelengths larger than 450 nm. A weak line is visible in the Li I doublet range.

Appendix C.23: HD 41020

Gaia DR3 classifies this star as LPV with a period of 238.79 days and an amplitude of 0.07 mag. No Li I visible, strong emission in Ca II-H and -K, H α also with emissions.

Appendix C.24: TYC 5340–1656–1

This star is classified as an RS CVn binary (stars with a giant primary of type F–K and a dwarf secondary of type G–M), in the *Gaia* DR3 catalogue. Our UVES spectrum shows two almost equally strong line systems, the cross correlation peaks provide the radial velocities provided in Table C.1. This fact clearly rules out the interpretation of this system as a classical RS CVn system since the two companions are of comparable luminosity. They are certainly giants, given the fact that the Balmer lines show no detectable wings. However it is interesting that both stars are chromospherically active (a typical signature of RS CVn systems) and this is obvious in Fig. C.1 where the core emissions of the Ca II H and K lines of both companions are clearly visible. A chemical analysis of such a star is beyond the scope of our paper, and in any case knowledge of the luminosity ratio of the two stars is required. By a quick comparison of the observed spectrum with synthetic spectra we expect the metallicity to be roughly solar and the $v \sin i$ of both stars between 20 and 30 km/s.

Appendix C.25: TYC 5422–1192–1

The star is a G giant member of the Open Cluster NGC 2423. The age of the cluster is estimated to be 310 Myr by (Bossini et al. 2019) and Dias et al. (2021) provide a metallicity of +0.12. Our UVES spectrum shows that the star is a fast rotator, probably above 100 km/s.

Table B.11: LTE and NLTE sulfur abundances obtained line by line for the MINCE stars.

Star	921.2 LTE	922.8 LTE	923.7 LTE	$\langle A(S) \rangle$ LTE	921.2 NLTE	922.8 NLTE	923.7 NLTE	$\langle A(S) \rangle$ NLTE
BD-11 3235	5.95	—	—	5.95	5.88	—	—	5.88
BD-13 3195	6.38	—	—	6.38	6.09	—	—	6.09
BD-15 5449	—	5.79	5.79	5.79 ± 0.00	—	5.72	5.72	5.72 ± 0.00
BD-16 2232	5.97	—	—	5.971	5.72	—	—	5.72
BD-17 3143	5.96	—	—	5.96	5.65	—	—	5.65
BD-19 6363	5.39	—	—	5.39	5.13	—	—	5.13
CD-27 16505	6.55	6.38	6.44	6.46 ± 0.07	6.30	6.28	6.36	6.32 ± 0.03
CD-28 10039	6.61	—	—	6.61	6.28	—	—	6.28
CD-28 16762	6.32	—	—	6.32	6.02	—	—	6.02
CD-29 15930	—	5.97	—	5.97	—	5.95	—	5.95
CD-33 2721	5.94	—	5.69	5.82 ± 0.12	5.69	—	5.55	5.62 ± 0.07
CD-33 15063	6.10	6.25	—	6.18 ± 0.07	5.99	6.18	—	6.09 ± 0.09
CD-36 518	6.17	6.19	—	6.18 ± 0.02	5.86	5.92	—	5.89 ± 0.03
CD-38 13823	4.91	5.02	—	4.96 ± 0.06	4.72	4.83	—	4.77 ± 0.06
CD-39 6037	6.96	6.85	—	6.91 ± 0.06	6.54	6.58	—	6.56 ± 0.02
CD-43 7161	6.34	6.35	—	6.35 ± 0.01	6.09	6.17	—	6.13 ± 0.04
CD-52 976	5.96	5.91	—	5.93 ± 0.03	5.55	5.55	—	5.55 ± 0.00
CD-57 1959	—	5.83	5.90	5.87 ± 0.03	—	5.69	5.77	5.73 ± 0.04
CD-62 15	5.73	—	—	5.73	5.41	—	—	5.41
TYC 6002-1724-1	5.27	5.43	—	5.35 ± 0.08	5.03	5.19	—	5.11 ± 0.08
TYC 6199-351-1	6.48	6.63	—	6.56 ± 0.08	6.32	6.54	—	6.43 ± 0.11
TYC 8161-752-1	6.34	6.41	6.18	6.31 ± 0.09	6.14	6.25	6.05	6.15 ± 0.08
TYC 8633-2281-1	6.69	—	—	6.69	6.64	—	—	6.64

Table C.1: Radial velocities for the components of SB2 stars.

STAR	MJD (d)	primary km s^{-1}	secondary km s^{-1}
CD -52 2441	59177.175649715	$+29.17 \pm 0.03$	$+15.63 \pm 0.03$
TYC 5340-1656-1	59169.157938165	$+7.1 \pm 0.3$	$+56.7 \pm 0.3$

Appendix C.26: TYC 5763-1084-1

Analysed in the RVS range with the COOL grid, our UVES spectrum requires a shift of -1.2 km s^{-1} with respect to the *Gaia* radial velocity.

Appendix C.27: TYC 6108-150-1

According to the *Gaia* DR3 catalogue this star is an SB1 binary, with a period of 390.6 days and a semi-amplitude of 13.9 km s^{-1} . The radial velocity of the centre of mass is 103.81 km s^{-1} , almost 6 km s^{-1} from our adopted radial velocity. The eccentricity is very low 0.06.

Appendix C.28: TYC 6195-815-1

Gaia DR3 classifies this star as LPV with a period of 365.63 days and an amplitude of 0.09 mag. Analysed in the RVS range with the COOL grid, our UVES spectrum requires a shift of $+2.2 \text{ km s}^{-1}$ with respect to the *Gaia* radial velocity.

Appendix C.29: TYC 8400-1610-1

The effective temperature from the [Mucciarelli et al. \(2021\)](#) is 3748 K we run MyGIsFOS in the RVS range with the COOL grid and $T_{\text{eff}} = 3750 \text{ K}$ to avoid extrapolation. Our UVES spectrum requires a shift of -2.3 km s^{-1} with respect to the *Gaia* radial velocity.

Appendix C.30: TYC 8394-14-1

Gaia DR3 classifies this star as an LPV with a period of 603.23 days and an amplitude of 0.05 mag.

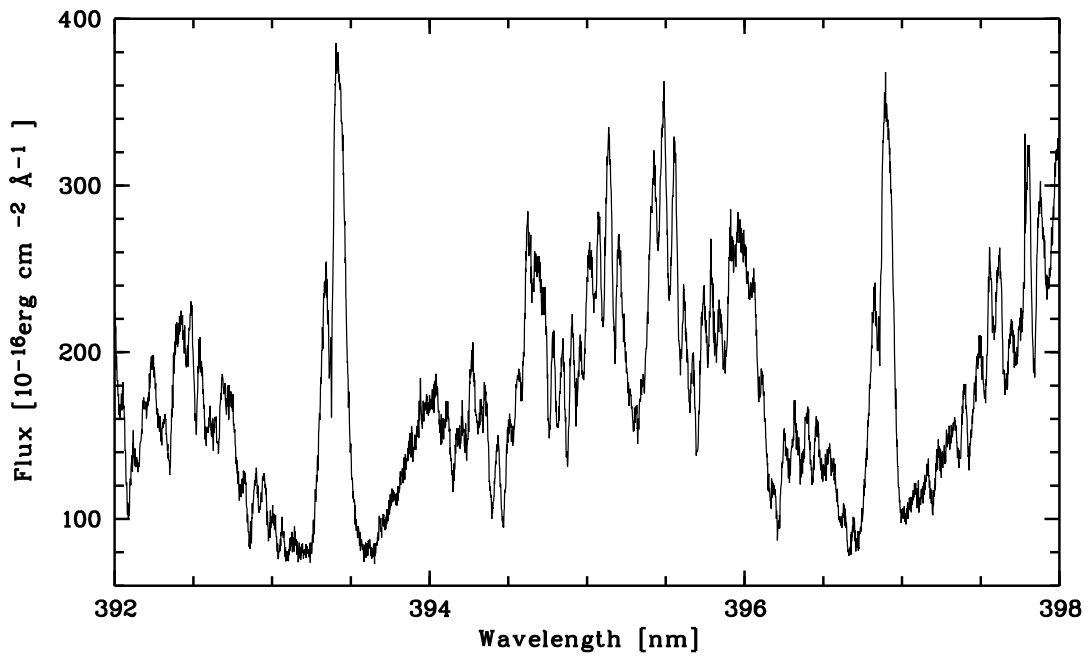
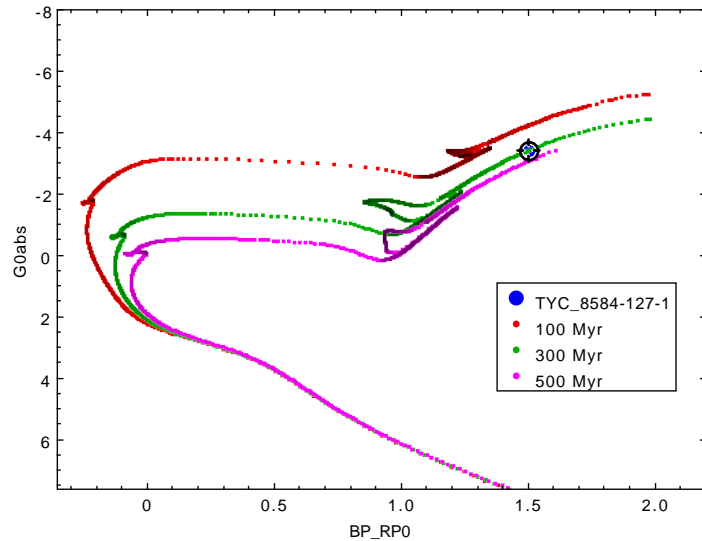


Fig. C.1: Ca II H& K lines of TYC 5340–1656–1.

Fig. C.2: Position in the *Gaia* CMD of TYC 8584–127–1 compared to three BASTI isochrones with metallicity -0.40 .

Appendix C.31: TYC 8584–127–1

This star has a measurable rotational velocity, that suggests that it is a young evolved massive star, similar to those studied by Lombardo et al. (2021). From a fot to an isolated Fe I line we derive a projected rotational velocity of 11.5 km s^{-1} . If we compare the position of the star in the CMD with BASTI isochrones (Pietrinferni et al. 2021) of metallicity -0.40 the implied age is 300 Myr and the mass 3.2 M_\odot . The radial velocity measured from our blue UVES spectrum is 21.67 km s^{-1} , in excellent agreement with the *Gaia* radial velocity (21.97 ± 0.23). Our radial velocity has not been zeroed on telluric lines so that the associated error is dominated by the centering of the star on the slit and this is of the order of 0.5 km s^{-1} .

We ran MyGIsFOS in the RVS range and found $[\text{Fe}/\text{H}] = -0.58 \pm 0.09$ from 16 Fe I lines. It is remarkable that such a young star is moderately metal-poor. Its Galactic orbit is circular on the Galactic plane at roughly the solar radius.